Cross-plane Transport in Nanographene Junctions

Shadiah Mohammed F Albalawi

Ph.D. Thesis in Physics

Department of Physics, Lancaster University, UK

This thesis is submitted in partial fulfilment of the requirements for the degree of Doctor of Philosophy

2023

Declaration

I declare that the work presented in this thesis is, to the best of my knowledge and belief, original and my own work. The material has not been submitted, either in whole or in part, for a degree at this, or any other university. This thesis documents work carried out between January 2020 and April 2023 at Lancaster University, UK, under the supervision of Prof. Colin J. Lambert and Dr Qingqing Wu and funded by the Ministry of Higher Education and Tabuk University, Saudi Arabia.

Shadiah Albalawi

2023

Dedication

My parents,

May Allah bless your souls and grant you a place in heaven.

My husband and my kids,

May God bless you all.

Acknowledgements

I am grateful to ALLAH for his mercy and blessings above all else.

Many people have helped me throughout my PhD journey. Although I am unable to thank them all or express my gratitude fully, I will try to do so briefly below.

First and foremost, I was fortunate to have Prof. Colin J. Lambert as my supervisor during my PhD study. He has provided me with invaluable advice, continuous support, and patience. I would like to express my sincere gratitude to my co-supervisor, Dr Qingqing Wu, for her valuable time, regular meetings, and invaluable advice, which have shaped my research over the years.

Also, the questions and suggestions made by Dr Songjun Hou, Dr Iain Grace, and Dr Ali Ismael throughout our group seminar were greatly appreciated. This work was conducted by experimentalists at Xiamen University. I would like to thank Prof. Wenjing Hong's group for their contributions.

It would be impossible for me to have achieved my dreams without the support and encouragement of my husband, Ahmed, who helped me achieve my goal of studying at Lancaster University. Words are never enough to appreciate all things you do for me, thank you for being an amazing husband, Dad, and my biggest supporter. I am extremely grateful to my parents for their love, prayers, caring and sacrifices for educating and preparing me for my future. I am deeply grateful to my sisters and brothers for their love, understanding, prayers and continuing support through the past years.

It is my sincere hope, Jamel, Saba, and Sama, that the experiences you have had and the challenges you have faced, as well as the difficulties you have encountered, will motivate you for a bright and promising future full of knowledge and ambition.

Last but not least, none of this work have been possible without the unlimited support of the Ministry of Education in the Kingdom of Saudi Arabia and the University of Tabuk.

Abstract

In recent years, heterojunctions and devices consisting of two-dimensional material stacks held together through van der Waals (vdW) forces have gained a lot of attention. In particular, graphene is a promising 2D material for use in single-molecule junctions, due to its high mechanical strength and robust chemical stability at room temperature. In the case of conventional metal electrode junctions, the molecules are attached to the metal electrodes through anchor groups at both ends. Through this configuration, electrons are transported along the molecular backbone, which means they travel from the left electrode to the right electrode via anchors attached to the molecule. Due to this, the size of the device corresponds to the length of the molecule. In contrast, in this thesis, a series of selected molecules was successfully sandwiched between two-dimensional graphene electrodes via vdW interactions to create single-molecule two-dimensional van der Waals heterojunctions (M-2D-vdWHs). In this case, electrons are transported between two graphene electrodes in a cross-plane manner, and the size of the device is determined by the molecule's thickness, rather than it’s length.

This thesis investigates cross-plane charge transport in graphene-based single-molecule van der Waals heterojunctions (M-2D-vdWHs). The results presented in this thesis are computed using SIESTA, which is a density functional theory (DFT) code that solves the Kohn-Sham self-consistent equations. This is then combined with the Gollum code to obtain electron transport properties. The resulting predictions are compared with the experimental results obtained using a newly developed cross-plane break junction (XPBJ) technique. In this thesis, two collaborative research projects have been undertaken, whose results are summarized below.

First, I have investigated charge transport through three well-defined molecular bilayer-graphenes (MBLGs), which consist of two vertically stacked graphene nanoflakes bound together via π-π stacking interactions, and molecular single-layer graphene (MSLG). DFT calculations indicate that the size of molecular graphene could be used to tune charge transport through vdW heterojunctions. Additionally, molecular junctions based on molecular single-layer graphene (MSLG) are more conductive than those based on molecular bilayer-layer graphenes (MBLGs). Moreover, the DFT calculations also indicate that the angles between the core of molecular graphene and peripheral mesityl groups significantly affect charge transport through MSLG junctions, where a decrease in the angle results in an increase in electrical conductance.

Secondly, I studied the influence of substituents and π-conjugation on cross-plane charge transport in graphene-based molecular junctions. The theoretical results demonstrated that the electrical conductance of molecular graphene junctions based on pyrene increases after being substituted by both electron-withdrawing and electron-donating groups. This suggests that both types of substituents can be used to tune charge transport in graphene-based junctions, which differ from conventional metal electrode junctions. Furthermore, I investigated the electrical conductance of the hydrogenated derivatives of pyrene, which have different degrees of conjugation and consequently different degrees of planarity. I found that the conductance of the molecular junctions decreases gradually with a weakening of the molecular conjugation.

Publications

1- Zhao, S., Z. Y. Deng**, S. Albalawi**, Q. Wu, L. Chen, H. Zhang, X. J. Zhao, H. Hou, S. Hou, G. Dong, Y. Yang, J. Shi, C. J. Lambert, Y. Z. Tan and W. Hong (2022). "Charge transport through single-molecule bilayer-graphene junctions with atomic thickness." Chem Sci **13**(20): 5854-5859.

2- Regulation of cross-plane transport by changing substituents and conjugation. To be submitted.

Table of contents

List of abbreviations

ICs	Integrated Circuits
CMOS	Complementary Metal-Oxide Semiconductor
SAMs	Self-Assembled Monolayers
MCBJ	Mechanically Controllable Break Junctions
STM	Scanning Tunnelling Microscopy
EBJ	Electromigration Break Junctions
DFT	Density Functional Theory
M-2D-vdWHs	Molecule Two-Dimensional Van Der Waals Heterojunctions
PAHs	Polycyclic Aromatic Hydrocarbons
QI	Quantum Interference
CQI	Constructive Quantum Interference
DQI	Destructive Quantum Interference
LDA	Local Density Approximation
GGA	Generalized Gradient Approximation
vdW-DF	Van Der Waals Density Functional
SCF	Self-Consistent Field
MBLG	Molecular Bilayer Graphene
MSLG	Molecular Single-Layer Graphene
SIESTA	Spanish Initiative for Electronic Simulations with Thousands of Atoms
HOMO	Highest Occupied Molecular Orbitals
LUMO	Lowest Unoccupied Molecular Orbitals
SMJs	Single-Molecule Junctions
DAPyr	1,6-diaminopyrene

DBPyr	1,6-dibromopyrene
XPBJ	Cross-Plane Break Junction
OPEs	Oligophenylene ethynylenes
BDFs	Benzodifurans

Chapter 1.

1 Introduction and Background

1.1 Molecular electronics

In 1965, Gordon Moore predicted that the number of transistors in integrated circuits (ICs) would double about every two years [1]. Consequently, electronic devices will become smaller, faster, and cheaper as transistors in integrated circuits become smaller and more efficient. Currently, complementary metal-oxide-semiconductor (CMOS) technology is widely utilized for integrating circuits (ICs), such as microprocessors, microcontrollers, memory chips, and other types of digital logic circuits. However, there are several challenges associated with continuous CMOS transistor downscaling due to physical limitations [2]. For instance, as the gate thickness is scaled down, leakage currents increase exponentially. Additionally, as the number of transistors per unit area in ICs increases, power consumption and thermal issues arise.

To overcome these challenges, one promising idea is to use single molecules, a few molecules, and self-assembled monolayers (SAMs) as basic components of electronic devices such as switches [3-8], rectifiers [9, 10], sensors [11, 12], and transistors [13-15], etc, which is well-known today as molecular electronics. The idea that a single molecule can function as a device was first suggested by Ratner and Aviram in 1974 [16]. They proposed a molecule consisting of three parts: a donor pi system, an acceptor pi system, and separated by a sigma-bonded molecular bridge (methylene). Such a device is called a molecular rectifier. This idea, however, did not have any significant impact due to the absence of real experiments to test it at that time.

Molecules possess attractive properties that make them suitable candidates for use as components in electronic devices [17]. For example, the size of a molecule is of the order of a nanometre (between 1 to 10 nm), which leads to increasing the capacity and improvement in the performance. Additionally, the presence of quantum interference in molecular junctions which can be used to adjust their electronic properties to provide switching and sensing capabilities. It is also possible to prepare many molecules at a low cost. However, molecules also have some obvious limitations such as the small size of the molecules makes it difficult to control the connection between the electrodes and the molecules. Also, molecules become unstable at high temperatures.

The field of molecular electronics became an active research area in the 1990s as fabrication techniques improved. The first experimental study that measured the conductance of a junction containing a single molecule was performed by Mark Reed's group and James Tour's group in 1997 [18]. They studied the electrical properties of benzene-dithiol connected to gold electrodes, using mechanically controllable break junctions (MCBJ). Then in 2003, the first STM-based single molecule conductance was repeatedly measured by forming thousands of gold-molecule-gold junctions [19]. To date, several experimental techniques have been developed for preparing molecular junctions and studying their electrical properties. The three common experimental techniques used to study electron transport through single molecules are mechanically controlled break junctions (MCBJ) [20], electromigration break junctions (EBJ) [21], and scanning tunnelling microscopy (STM) [22].

Combined with experimental techniques, many theoretical tools have been developed and used to predict the transport properties in molecular devices. Currently, density functional theory (DFT) is an enormously successful method for electronic structure

simulations of the ground-state of metals, semiconductors and insulators [23]. For bulk materials, molecules, and surfaces, DFT is one of the most widely used computational tools and it is essential to verify experiment results and provide guidance for experiments.

1.2 Molecular junctions

In nanoscale electronic systems, a molecular junction refers to a molecule that is connected robustly with at least two electrodes via anchor groups. To explore the influence of the structure of a molecular junction on transport properties, the molecule, the electrode, and their contact have been extensively investigated.

Firstly, several studies have examined the effect of intrinsic properties of molecules, such as their length [24, 25] and conformation [26-28]. Secondly, a variety of anchoring groups have been investigated such as thiol [29, 30], amines (NH_2) [31, 32], and fullerene (C60) [33] etc. It is found that the choice of anchoring groups affects the strength of the connection between the molecule and the electrodes, and therefore determines the stability of the molecular junction [34].

Thirdly, electrode materials play a vital role in the charge transport at single-molecule junctions and can be classified into metal and non-metal. To date, gold electrodes are the most widely used for studying charge transport in single-molecule junctions due to their good malleability and strong bonding to sulfur [19]. In addition, other materials such as Pt, Cu, Pd, and Ag have also been reported to be adopted as electrodes [35-39]. However, it has been reported that electronic devices utilizing metal electrodes have experienced some problems. For instance, the high atomic mobility of metal atoms makes it difficult to form stable nanogaps between metal electrodes [40, 41]. Also,

except for gold, all metal electrodes are easily oxidized under ambient conditions [37]. Non-metal electrodes such as carbon-based materials like graphene are ideal materials to replace metal electrodes. Graphene has attracted considerable scientific and technological interest since its discovery by Andre Geim and Konstantin Novoselov in 2004 [42]. This is due to its unique properties such as exceptional electrical conductivity, mechanical strength, and chemical stability. Graphene is composed of carbon atoms arranged in a perfect hexagonal lattice, with each carbon atom bonded to three nearby carbon atoms. It forms a single layer that is only one atom thick. It is a fundamental component of other carbon allotropes, such as graphite, carbon nanotubes, and fullerene.

As this thesis discusses the transport of charge through molecular graphene junctions, I will discuss the advantages of using graphene as an electrode material and present some examples from the literature.

1.3 Molecular junctions with graphene electrodes

Recently, some researchers have succeeded in fabricating molecular junctions by replacing metal electrodes with graphene electrodes. This is due to the graphene's highly dispersive density of states near the Fermi energy E_F [43] and robust mechanical stability. Furthermore, graphene electrodes can form stable contact with single molecules through covalent bonds (amide bond) [44, 45] as well as non-covalent bonds such as van der Waals interactions [46-48] and π-π interactions [49-52]. As a result of the advantages listed above, by using two-dimensional planar graphene electrodes, we can study the intrinsic properties of molecules through non-covalent interactions with graphene electrodes. Figure 1.1 shows some examples of graphene-molecule-graphene

junctions in which the molecule attaches to graphene electrodes via covalent bonds and non-covalent interactions as described below [53].

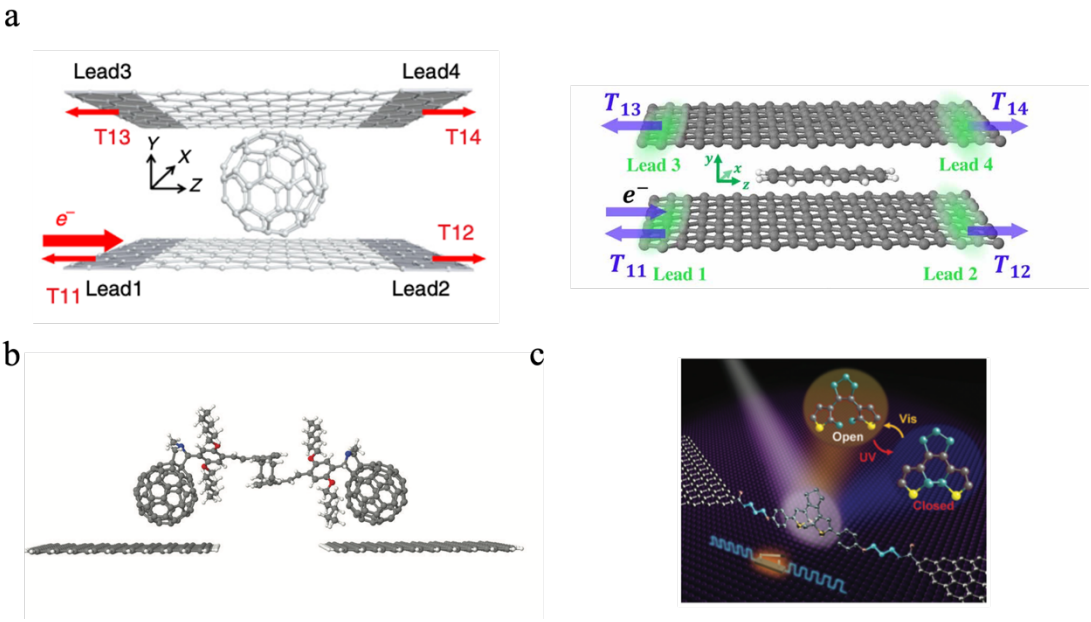

Figure 1.1. Examples of molecular junctions with graphene electrodes. (a) (left) cross-plane graphene-C60-graphene junction and graphene-anthracene (PAH3)-graphene junction (right) based on van der Waals interactions. (b) In-plane graphene junctions with two C60 as anchors connecting the molecule to graphene electrodes via π-π stacking interactions. (c) In-plane graphene-diarylethene-graphene junction via an amide bond between the molecule and two graphene electrodes.

Figure 1.1(a) presents (left) various pristine fullerenes including (C_{60}, C_{70}, C_{76} and C_{90}) and (right) nine polycyclic aromatic hydrocarbons (PAHs) were successfully sandwiched between two graphene electrodes via the overlap between π orbitals in these molecules and graphene electrodes to form single-molecule two-dimensional van der

Waals heterojunctions M-2D-vdWHs [46, 47]. Also, as shown in Figure 1.1(b), a single molecule with anchors like anthracene [54], can be weakly coupled to graphene electrodes via π-π stacking interactions. Other anchor groups were used to connect the molecule to the graphene electrodes such as fullerene (C_{60}) [55, 56] and polycyclic aromatic hydrocarbons (PAHs). Figure 1.1(c) presents the case of graphene in-plane junctions with robust amide bonds where graphene point contacts functionalized by -COOH can react with molecules ended with ($-NH_2$), to form stable single-molecule junctions [44, 45].

1.4 Quantum interference

A great deal of interest has been drawn to quantum interference (QI), which plays a crucial role in charge transport in single-molecule junctions. QI can be explained by electron propagation via molecular orbitals whose paths differ in energy. In recent years, both theoretical and experimental investigations of constructive and destructive quantum interference effects in a single molecule at room temperature have been conducted [54, 57-64]. It is found that as molecular orbitals can be manipulated by chemical design, quantum interference may be used to control the conductance of molecular devices [65]. In other words, conductance may be enhanced through constructive quantum interference (CQI) or suppressed through destructive quantum interference (DQI) due to the quantum interference effects. Quantum interference is found to be strongly correlated to the connectivity between the electrodes and the molecular core. As a simple example, quantum interference significantly reduces the electron transfer through a meta-connected benzene ring in comparison to a para-connected benzene ring [66, 67]. Furthermore, QI effects were found to be dependent on conjugation [68, 69] and heteroatom substitution [70]. The ability to adjust the

properties of the molecules offers the possibility of developing new molecular devices at room temperature. A particular application is the use of quantum interference to control molecular switches with extremely large on-off ratios [71, 72].

1.5 Conclusion

A brief overview of the field of molecular electronics is provided in this chapter, including a brief historical background and a discussion of the development of the field along with improvements to experimental and theoretical techniques. I also discussed the key factors that influence charge transport at molecular junctions. Next, I discussed single-molecule junctions formed using graphene electrodes, their advantages, and examples. Lastly, I reviewed quantum interference effects in molecular devices.

1.6 Outline of thesis

The purpose of this thesis is to investigate cross-plane electron transport in graphene-single molecule-graphene junctions. It consists of six chapters, as follows:

Chapter 1 discuss molecular electronics and single-molecule junctions with graphene electrodes. Then, density functional theory is discussed in **chapter 2** including the many-body Schrodinger equation, the Hohenberg and Kohn theorems, and the Kohn and Sham method. Next, several fundamental concepts related to quantum transport are presented in **chapter 3**, including the Landauer or scattering approach, the scattering matrix, and the transmission function. Following that, to provide unique insights into cross-plane charge transport through multi-layered structures, three well-defined molecular bilayer-graphene structures, comprised of two graphene nanoflakes stacked vertically via π-π stacking interactions, with varying sizes, were investigated in **chapter**

4. **Chapter 5** presents a variety of substituents including electron-withdrawing and electron-donating substituents, π-conjugation, and planarity, are studied experimentally and theoretically to determine their influence on charge transport in graphene-single molecule-graphene junction.

1.7 Bibliography

[1] Moore GE. Cramming more components onto integrated circuits. Electronics 1965.

[2] Haron NZ, Hamdioui S. Why is CMOS scaling coming to an END? In: 2008 3rd International Design and Test Workshop. 2008. pp. 98-103.

[3] Charles P. Collier GM, Eric W. Wong, Yi Luo, Kristen Beverly, Jos´e Sampaio, Fran¸cisco M. Raymo,, J. Fraser Stoddart JRH. A [2]Catenane Based Solid State Electronically Reconfigurable Switch. SCIENCE 2000.

[4] Z. J. Donhauser BAM, K. F. Kelly, L. A. Bumm, J. D. Monnell, J. J. Stapleton, D. W. Price Jr., A. M. Rawlett, D. L. Allara, J. M. Tour, P. S. Weiss. Conductance Switching in Single Molecules Through Conformational Changes. SCIENCE 2001.

[5] Yong Chen G-YJ, Douglas A A Ohlberg, Xuema Li, Duncan R Stewart, Jan O Jeppesen,, Kent A Nielsen JFSaRSW. Nanoscale molecular-switch crossbar circuits. NANOTECHNOLOGY 2003.

[6] Wang X, Li, X., Ning, S., & Ismael, A. . Orientation preference control: a novel approach for tailoring molecular electronic functionalities. . Journal of Materials Chemistry C 2023.

[7] Ismael. AK. 20-State Molecular Switch in a Li@C60 Complex. ACS Omega 2023.

[8] Alshammari M, Al-Jobory, A. A., Alotaibi, T., Lambert, C. J., & Ismael, A. Orientational control of molecular scale thermoelectricity. Nanoscale Advances 2022.

[9] Martin AS, Sambles JR, Ashwell GJ. Molecular rectifier. Phys Rev Lett 1993; 70:218-221.

[10] Aleksandar Staykov DN, and Kazunari Yoshizawa. Theoretical Study of Donor-π-Bridge-Acceptor Unimolecular Electric Rectifier. J. Phys. Chem. 2007.

[11] Kolmakov A, Moskovits M. Chemical Sensing and Catalysis by One-Dimensional Metal-Oxide Nanostructures. Annual Review of Materials Research 2004; 34:151-180.

[12] G. Raschke SB, A. S. Susha, A. L. Rogach, T. A. Klar, and J. Feldmann. Gold Nanoshells Improve Single Nanoparticle Molecular Sensors. Nano Letters 2004.

[13] Martel R, Schmidt T, Shea HR, Hertel T, Avouris P. Single- and multi-wall carbon nanotube field-effect transistors. Applied Physics Letters 1998; 73:2447-2449.

[14] Bao HEKaZ. The Physical Chemistry of Organic Field-Effect Transistors. J. Phys. Chem. 2000.

[15] DeHon A. Array-based architecture for FET-based, nanoscale electronics. IEEE Transactions On Nanotechnology 2003; 2:23-32.

[16] Aviram A, Ratner MA. Molecular rectifiers. Chemical Physics Letters 1974; 29:277-283.

[17] Cuevas JC, and Scheer, Elke. Molecular Electronics an Introduction to Theory and Experiment. 2nd ed. 2017.

[18] M. A. Reed CZ, C. J. Muller, T. P. Burgin, J. M. Tour. Conductance of a Molecular Junction. SCIENCE 1997.

[19] Tao BXaNJ. Measurement of Single-Molecule Resistance by Repeated Formation of Molecular Junctions. SCIENCE 2003.

[20] Xiang D, Jeong H, Lee T, Mayer D. Mechanically controllable break junctions for molecular electronics. Adv Mater 2013; 25:4845-4867.

[21] Park H, Lim AKL, Alivisatos AP, Park J, McEuen PL. Fabrication of metallic electrodes with nanometer separation by electromigration. Applied Physics Letters 1999; 75:301-303.

[22] Chen F, Hihath J, Huang Z, Li X, Tao NJ. Measurement of single-molecule conductance. Annu Rev Phys Chem 2007; 58:535-564.

[23] K. I. Ramachandran DG, Krishnan Namboori. Computational Chemistry and Molecular Modeling Principles and Applications. Springer 2008.

[24] Su Ying Quek HJC, Steven G. Louie, and J. B. Neaton. Length Dependence of Conductance in Aromatic Single-Molecule Junctions. American Chemical Society 2009.

[25] Moreno-Garcia P, Gulcur M, Manrique DZ, Pope T, Hong W, Kaliginedi V, Huang C, Batsanov AS, Bryce MR, Lambert C, Wandlowski T. Single-molecule conductance of functionalized oligoynes: length dependence and junction evolution. J Am Chem Soc 2013; 135:12228-12240.

[26] Venkataraman L, Klare JE, Nuckolls C, Hybertsen MS, Steigerwald ML. Dependence of single-molecule junction conductance on molecular conformation. Nature 2006; 442:904-907.

[27] Mishchenko A, Vonlanthen D, Meded V, Burkle M, Li C, Pobelov IV, Bagrets A, Viljas JK, Pauly F, Evers F, Mayor M, Wandlowski T. Influence of conformation on conductance of biphenyl-dithiol single-molecule contacts. Nano Lett 2010; 10:156-163.

[28] Luke A. Wilkinson TLRB, Iain M. Grace, Joseph Hamill, Xintai Wang, Sophie Au-Yong, Ali Ismael, Samuel P. Jarvis, Songjun Hou, Tim Albrecht, Lesley F. Cohen, Colin Lambert, Benjamin J. Robinson, Nicholas J. Long . Assembly, structure and thermoelectric properties of 1, 1′-dialkynylferrocene 'hinges'. Chemical Science 2022.

[29] Strange M, Lopez-Acevedo O, Häkkinen H. Oligomeric Gold−Thiolate Units Define the Properties of the Molecular Junction between Gold and Benzene Dithiols. The Journal of Physical Chemistry Letters 2010; 1:1528-1532.

[30] Alshehab A, and Ali K. Ismael. Impact of the terminal end-group on the electrical conductance in alkane linear chains. RSC advances 2023.

[31] Jordan R. Quinn FWF, Jr., Latha Venkataraman,Mark S. Hybertsen,,and Ronald Breslow. Single-Molecule Junction Conductance through Diaminoacenes. American Chemical Society 2007.

[32] Latha Venkataraman YSP, Adam C. Whalley, Colin Nuckolls, Mark S. Hybertsen, and Michael L. Steigerwald. Electronics and Chemistry: Varying Single-Molecule Junction Conductance Using Chemical Substituents. American Chemical Society 2007.

[33] Christian A. Martin DD, Jakob Kryger Sørensen, Thomas Bjørnholm, Jan M. van Ruitenbeek, and Herre S. J. van der Zant. Fullerene-Based Anchoring Groups for Molecular Electronics. American Chemical Society 2008.

[34] Lin L, Jiang J, Luo Y. Elastic and inelastic electron transport in metal–molecule(s)–metal junctions. Physica E: Low-dimensional Systems and Nanostructures 2013; 47:167-187.

[35] Chih-Hung Ko M-JH, Ming-Dung Fu, and Chun-hsien Chen. Superior Contact for Single-Molecule Conductance- Electronic Coupling of Thiolate and Isothiocyanate on Pt, Pd, and Au. American Chemical Society 2009.

[36] Christlieb N, Bessell MS, Beers TC, Gustafsson B, Korn A, Barklem PS, Karlsson T, Mizuno-Wiedner M, Rossi S. A stellar relic from the early Milky Way. Nature 2002; 419:904-906.

[37] Kim T, Vazquez H, Hybertsen MS, Venkataraman L. Conductance of molecular junctions formed with silver electrodes. Nano Lett 2013; 13:3358-3364.

[38] Nakazumi T, Kaneko S, Kiguchi M. Electron Transport Properties of Au, Ag, and Cu Atomic Contacts in a Hydrogen Environment. The Journal of Physical Chemistry C 2014; 118:7489-7493.

[39] Manabu Kiguchi SM, Takuya Takahashi, Kenji Hara, Masaya Sawamura, and Kei Murakoshi. Conductance of Single 1,4-Benzenediamine Molecule Bridging between Au and Pt Electrodes. American Chemical Society 2008.

[40] Prins F, Hayashi T, de Vos van Steenwijk BJA, Gao B, Osorio EA, Muraki K, van der Zant HSJ. Room-temperature stability of Pt nanogaps formed by self-breaking. Applied Physics Letters 2009; 94.

[41] O'Neill K, Osorio EA, van der Zant HSJ. Self-breaking in planar few-atom Au constrictions for nanometer-spaced electrodes. Applied Physics Letters 2007; 90.

[42] Novoselov KS, Fal'ko VI, Colombo L, Gellert PR, Schwab MG, Kim K. A roadmap for graphene. Nature 2012; 490:192-200.

[43] Kim T, Liu ZF, Lee C, Neaton JB, Venkataraman L. Charge transport and rectification in molecular junctions formed with carbon-based electrodes. Proc Natl Acad Sci U S A 2014; 111:10928-10932.

[44] Chuancheng Jia AM, Na Xin, Shaoyun Huang, Jinying Wang, Qi Yang, Shuopei Wang, Hongliang Chen, Duoming Wang, Boyong Feng, Zhirong Liu, Guangyu Zhang, Da-Hui Qu, He Tian, Mark A. Ratner, H. Q. Xu, Abraham Nitzan, Xuefeng Guo. Covalently bonded single-molecule junctions with stable and reversible photoswitched conductivity. SCIENCE 2016.

[45] Jia C, Wang J, Yao C, Cao Y, Zhong Y, Liu Z, Liu Z, Guo X. Conductance switching and mechanisms in single-molecule junctions. Angew Chem Int Ed Engl 2013; 52:8666-8670.

[46] Tan Z, Zhang D, Tian HR, Wu Q, Hou S, Pi J, Sadeghi H, Tang Z, Yang Y, Liu J, Tan YZ, Chen ZB, Shi J, Xiao Z, Lambert C, Xie SY, Hong W. Atomically defined angstrom-scale all-carbon junctions. Nat Commun 2019; 10:1748.

[47] S. Zhao QW, J. Pi, J. Liu, J. Zheng, S. Hou, J. Wei, R. Li, H. Sadeghi, Y. Yang, J. Shi, Z. Chen, Z. Xiao, C. Lambert, W. Hong,. Cross-plane transport in a single-molecule two-dimensional van der Waals heterojunction. SCIENCE ADVANCES 2020.

[48] Zhao S, Deng ZY, Albalawi S, Wu Q, Chen L, Zhang H, Zhao XJ, Hou H, Hou S, Dong G, Yang Y, Shi J, Lambert CJ, Tan YZ, Hong W. Charge transport through single-molecule bilayer-graphene junctions with atomic thickness. Chemical Science 2022; 13:5854-5859.

[49] Lortscher E. Wiring molecules into circuits. Nat Nanotechnol 2013; 8:381-384.

[50] El Abbassi M, Sangtarash S, Liu X, Perrin ML, Braun O, Lambert C, van der Zant HSJ, Yitzchaik S, Decurtins S, Liu SX, Sadeghi H, Calame M. Robust graphene-based molecular devices. Nat Nanotechnol 2019; 14:957-961.

[51] Thomas JO, Limburg B, Sowa JK, Willick K, Baugh J, Briggs GAD, Gauger EM, Anderson HL, Mol JA. Understanding resonant charge transport through weakly coupled single-molecule junctions. Nat Commun 2019; 10:4628.

[52] Limburg B, Thomas JO, Holloway G, Sadeghi H, Sangtarash S, Hou IC-Y, Cremers J, Narita A, Müllen K, Lambert CJ, Briggs GAD, Mol JA, Anderson HL. Anchor Groups for Graphene-Porphyrin Single-Molecule Transistors. Advanced Functional Materials 2018; 28.

[53] Zhao S, Chen H, Qian Q, Zhang H, Yang Y, Hong W. Non-covalent interaction-based molecular electronics with graphene electrodes. Nano Research 2021.

[54] Prins F, Barreiro A, Ruitenberg JW, Seldenthuis JS, Aliaga-Alcalde N, Vandersypen LM, van der Zant HS. Room-temperature gating of molecular junctions using few-layer graphene nanogap electrodes. Nano Lett 2011; 11:4607-4611.

[55] Ullmann K, Coto PB, Leitherer S, Molina-Ontoria A, Martin N, Thoss M, Weber HB. Single-molecule junctions with epitaxial graphene nanoelectrodes. Nano Lett 2015; 15:3512-3518.

[56] Leitherer S, Coto PB, Ullmann K, Weber HB, Thoss M. Charge transport in C(60)-based single-molecule junctions with graphene electrodes. Nanoscale 2017; 9:7217-7226.

[57] Lambert CJ. Basic concepts of quantum interference and electron transport in single-molecule electronics. Chem Soc Rev 2015; 44:875-888.

[58] Vazquez H, Skouta R, Schneebeli S, Kamenetska M, Breslow R, Venkataraman L, Hybertsen MS. Probing the conductance superposition law in single-molecule circuits with parallel paths. Nature Nanotechnology 2012; 7:663-667.

[59] Ballmann S, Hartle R, Coto PB, Elbing M, Mayor M, Bryce MR, Thoss M, Weber HB. Experimental evidence for quantum interference and vibrationally induced decoherence in single-molecule junctions. Phys Rev Lett 2012; 109:056801.

[60] Aradhya SV, Meisner JS, Krikorian M, Ahn S, Parameswaran R, Steigerwald ML, Nuckolls C, Venkataraman L. Dissecting contact mechanics from quantum interference in single-molecule junctions of stilbene derivatives. Nano Lett 2012; 12:1643-1647.

[61] Kaliginedi V, Moreno-Garcia P, Valkenier H, Hong W, Garcia-Suarez VM, Buiter P, Otten JL, Hummelen JC, Lambert CJ, Wandlowski T. Correlations between molecular structure and single-junction conductance: a case study with oligo(phenylene-ethynylene)-type wires. J Am Chem Soc 2012; 134:5262-5275.

[62] Aradhya S, Venkataraman, L. Single-molecule junctions beyond electronic transport. Nature Nanotechnology 2013; 8.

[63] Arroyo CR, Tarkuc, S., Frisenda, R., Seldenthuis, J.S., Woerde, C.H., Eelkema, R., Grozema, F.C. and Van Der Zant, H.S., . Signatures of quantum interference effects on charge transport through a single benzene ring. Angewandte Chemie 2013.

[64] González MT, Ali K. Ismael, Miguel Garcia-Iglesias, Edmund Leary, Gabino Rubio-Bollinger, Iain Grace, David Gonzalez-Rodriguez, Tomas Torres, Colin J. Lambert, and Nicolas Agrait. Interference Controls Conductance in Phthalocyanine Molecular Junctions. The Journal of Physical Chemistry C 2021.

[65] Constant M. Gu´edon HV, Troels Markussen, Kristian S. Thygesen, Jan C. Hummelen, and Sense Jan van der Molen. Observation of Quantum Interference in Molecular Charge Transport. Nature Nanotechnology 2012; 7.

[66] P. Sautet CJ. Electronic interference produced by a benzene embedded in a polyacetylene chain. Chemical Physics Letters 1988; 153: 511-516,.

[67] Cendrine Patoux CC, Jean-Pierre Launay,* Christian Joachim,* and Andre´ Gourdon. Topological Effects on Intramolecular Electron Transfer via Quantum Interference. Inorganic Chemistry 1997:5037-5049.

[68] Gemma C. Solomon DQA, Randall H. Goldsmith, Thorsten Hansen, Michael R. Wasielewski, Richard P. Van Duyne, and Mark A. Ratner. Quantum Interference in Acyclic Systems: Conductance of Cross-Conjugated Molecules. American Chemical Society 2008.

[69] Juan Hurtado-Gallego RD, Iain M Grace, Laura Rincón-García, Andrei S Batsanov, Martin R Bryce, Colin J Lambert, Nicolás Agraït. Quantum interference dependence on molecular configurations for cross-conjugated systems in single-molecule junctions. Molecular Systems Design & Engineering 2022; 7.

[70] Zi-Zhen Chen S-DW, Jin-Liang Lin, Li-Chuan Chen, Jing-Jing Cao, Xiangfeng Shao, Colin J. Lambert, Hao-Li Zhang. Modulating Quantum Interference Between

Destructive and Constructive States in Double N-Substituted Single Molecule Junctions. Advanced Electronic Materials 2023; 9.

[71] Liljeroth SJvdMaP. Charge transport through molecular switches. Journal of Physics: Condensed Matter 2010; 22.

[72] Max Roemer AG, David Jago, David Costa-Milan, Jehan Alqahtani, Juan Hurtado-Gallego, Hatef Sadeghi, Colin J Lambert, Peter R Spackman, Alexandre N Sobolev, Brian W Skelton, Arnaud Grosjean, Mark Walkey, Sven Kampmann, Andrea Vezzoli, Peter V Simpson, Massimiliano Massi, Inco Planje, Gabino Rubio-Bollinger, Nicolás Agraït, Simon J Higgins, Sara Sangtarash, Matthew J Piggott, Richard J Nichols, George A Koutsantonis. 2, 7-and 4, 9-Dialkynyldihydropyrene molecular switches: syntheses, properties, and charge transport in single-molecule junctions. Journal of the American Chemical Society 2022; 144.

Chapter 2.

2 Density Functional Theory

In this chapter, I will provide a brief overview of density functional theory (DFT), focusing on the main problem which is solving the Schrodinger equation of the many-body system in section (2.2). Next, I will present two key theorems which form the foundation of the DFT proposed by Hohenberg and Kohn in section. After that, section (2.4) discusses the Kohn-Sham equations, a set of simple and powerful equations that make DFT the most widely used method. Finally, I compare two of the widely used approximations, local density approximation (LDA) and generalized gradient approximation (GGA) and then describe the van der Waals density functional (vdW-DF) method that was applied in our calculations in chapters 4 and 5.

2.1 Introduction

A collection of atoms forms molecules, solids, etc. Atoms are composed of electrons and nuclei. For large molecules and solids, solving the Schrodinger equation is impossible due to electron-electron and electron-nuclei interactions.

The density functional theory (DFT) is an alternative method to solve the Schrodinger equation using electron density instead of many-body wave functions. Electron density is preferred over the wave function because it is a function of three spatial variables, in contrast to the wave function, which is a function of 3N variables (where N is the number of electrons, and it is 4N in the case of spin) [1]. The entire field is based on two fundamental mathematical theorems proved by Hohenberg-Kohn [2] as well as a set of equations derived by Kohn-Sham [3]. Nowadays, density functional theory

(DFT), is a valuable research tool for electronic structure calculations in material science, where efficient approximations are used to simulate large-scale systems.

2.2 Many-body system

In quantum mechanics, the system of electrons and nuclei can be described by the time-independent Schrodinger equation,

$$H\,\psi = E\,\psi \tag{2.1}$$

where E is the energy eigenvalue, and the many-body Hamiltonian operator [4] is,

$$\widehat{H} = \frac{-\hbar^2}{2m_i}\sum_{i=1}^{N_e}\nabla_i^2 - \frac{\hbar^2}{2M_I}\sum_{I=1}^{N_{nuc}}\nabla_I^2 + \frac{1}{2}\sum_{i\neq j}\frac{e^2}{|r_i - r_j|} - \sum_{i,I}\frac{Z_I e^2}{|r_i - R_I|} + \frac{1}{2}\sum_{I\neq J}\frac{Z_I Z_J e^2}{|R_I - R_J|} \tag{2.2}$$

Where $\hbar$ is Planck's constant, m_i and M_I represent the mass of the electron and nucleus respectively. Z_I is the atomic number of the I^{th} atom, e is the charge of the electron, r_i and R_I represent the positions of i^{th} electron and I^{th} nucleus.

In equation 2.2, the first two terms represent the kinetic energies of the electron and nucleus, followed by electron-electron interactions, electron-nucleus interactions, and nucleus-nucleus interactions respectively. Therefore, equation (2.2) can also be written as follows:

$$\widehat{H} = \hat{T}_e(r) + \hat{T}_N(R) + V_{ee}(r) + V_{eN}(r,R) + V_{NN}(R) \tag{2.3}$$

Finding a solution to equation (2.1), for large molecules or solids is a challenge as the Hamiltonian will have a dreadful appearance. To reduce the complexity of the many-

body Schrodinger equation, the Born-Oppenheimer or adiabatic approximation is used [5].

Born-Oppenheimer approximation assumes that compared to electrons nuclei are much more massive and consequently electrons move faster than nuclei. As a result, the nuclei can be assumed to be frozen at some positions (R) and therefore, the kinetic energy of nuclei can be ignored, and their potential energy added as a constant. Consequently, the full wave function can be separated into electronic and nuclear wave functions, and the Schrodinger equation of the electronic part can be written as follows:

$$\hat{H}_e(r,R)\psi_e(r,R) = E_e\psi_e(r,R) \qquad 2.4$$

in which the electronic Hamiltonian can be written as

$$\hat{H} = \frac{-\hbar^2}{2m_i}\sum_{i=1}^{N_e}\Delta_i^2 + \frac{1}{2}\sum_{i\neq j}\frac{e^2}{|r_i - r_j|} - \sum_{i,I}\hat{V}_{ext}(r_i) \qquad 2.5$$

where $\hat{V}_{ext}$ is the potential acting on the electrons due to the nuclei. As a result of the Born-Oppenheimer approximation, the electronic Hamiltonian of the system is less complicated, however, it is still a challenge to deal with electron-electron interactions. The following section shows that using DFT is more practical than the many-body wave functions.

2.3 Hohenberg-Kohn theorems

The field of density functional theory (DFT) depends on two fundamental theorems which were proved by P. Hohenberg and W. Kohn in their famous paper [2], in which the ground-state density $n(r)$, plays a central role. Following are the two HK theorems [4, 6]:

Theorem 1: For any system of an interacting electron moving in an external potential, the external potential $V_{ext}(r)$ is uniquely determined, by the ground-state density $n(r)$. This means, There is a one-to-one correspondence between the electron density and the external potential. Therefore, it is not possible to assume the existence of two different external potentials $V_{ext}^{(1)}(r)$ and $V_{ext}^{(2)}(r)$, differing by more than a constant, and leading to the same ground state density $n(r)$.

Theorem 2: The variational principle: In external potential $V_{ext}(r)$, the true ground state is the one that minimizes the total energy through the universal functional $E_{HK}[n]$.

A Hamiltonian for a system of electrons and fixed nuclei moving under the influence of an external potential $V_{ext}(r)$ can be expressed as:

$$\widehat{H} = \frac{-\hbar^2}{2m_i}\sum_{i=1}^{N_e}\nabla_i^2 + \frac{1}{2}\sum\nolimits_{i\neq j}\frac{e^2}{|r_i - r_j|} - \sum\nolimits_{i,I}\hat{V}_{ext}\,(r_i) \qquad 2.6$$

The total energy functional in terms of density has the form [4],

$$E_{HK}[n] = F_{HK}[n] + \int V_{ext}(r)n(r)dr \qquad 2.7$$

In which $F_{HK}[n] = T[n] + E_{int}[n]$, represents a universal functional or HK functional. As the kinetic energy *T* and the electron-electron interaction energy only depend on the charge density, they are universal. however, $F_{HK}[n]$ is unknown.

2.4 Kohn-Sham equations

Due to the Kohn-Sham approach that was first proposed in 1965, density functional theory is today a popular method for simulating electronic structures [3, 4]. Inspired by the Hartree approach, which is an independent particle system, Kohn and Sham

assumed that a real system with interacting electrons can be replaced by an auxiliary system with non-interacting electrons that leads to the same density. Here, I will derive the self-consistent Kohn and Sham equations which represent single-particle equations.

In the beginning, we add and subtract the kinetic energy functional of an independent particle system of density, *n* and the equivalent of the electron-electron energy term within the Hartree approximation.

$$E_v[n] = F_{HK}[n] + \int V_{ext}(r)n(r)dr \; + T_s[n(r)] - T_s[n(r)] + \frac{1}{2}\int \frac{n(r)n(r')}{|r-r'|}\, drdr' - \frac{1}{2}\int \frac{n(r)n(r')}{|r-r'|}\, drdr' \tag{2.8}$$

Thus, the total energy functional could be written in the form,

$$E_v[n] = \underbrace{T_s[n(r)] + \int V_{ext}(r)n(r)dr + \frac{1}{2}\int \frac{n(r)n(r')}{|r-r'|}\, drdr'}_{E_H} + E_{XC}[n(r)] \tag{2.9}$$

the final term $E_{XC}[n(r)]$ is the so-called exchange-correlation energy functional. Using the HK variational theorem, one can write equation (2.9) for the interacting system as follows:

$$E_{v(r)}[n] = T_s[n(r)] + \int V_{ext}(r)n(r)dr + \frac{1}{2}\int \frac{n(r)n(r')}{|r-r'|}\, drdr' + E_{xc}[n(r)] \geq E \tag{2.10}$$

The Euler-Lagrange equations are used to minimize the previous equation in terms of density, the result is the single-particle Kohn-Sham equations for noninteracting electrons, which give the exact electron density of the real system.

$$\left[-\frac{\nabla^2}{2}+\underbrace{V_{ext}(r)+\int dr'\frac{n(r')}{|r-r'|}+\frac{\delta E_{xc}[n]}{\delta n(r)}}_{V_{eff(r)}}\right]\varphi_j(r)=\varepsilon_j\varphi_j(r) \tag{2.11}$$

equivalent to

$$\left[-\frac{\nabla^2}{2}+V_{eff}(r)\right]\varphi_j(r)=\varepsilon_j\varphi_j(r) \tag{2.12}$$

In which *j* represents spatial coordinates and spin quantum number and the $V_{eff}(r)$ is the sum of three terms, the external potential acting on the real system, the Hartree potential, and the exchange-correlation potential which is called Kohn-Sham potential or effective potential and has the form,

$$V_{eff}(r)=V_{ext}(r)+V_H(r)+V_{xc}(r) \tag{2.13}$$

where $V_{xc}(r)$ is local exchange-correlation potential, and the electron density is given by,

$$n(r)=\sum_{j=1}^{N}\left|\varphi_j(r)\right|^2 \tag{2.14}$$

Finally, the ground-state energy could be written as,

$$E = \sum_j \varepsilon_j + E_{xc}[n(r)] - \int V_{XC}(r)n(r)dr \qquad 2.15$$

$$-\frac{1}{2}\int \frac{n(r)n(r')}{|r-r'|}\, drdr'$$

To solve equation (2.11), one must have the Hartree potential and the exchange-correlation potential, which means that the density is not just an output, but also an input. To solve this, the iterative method called the Self-Consistent Field approach (SCF) was first introduced by Douglas Hartree who used it to solve Hartree equations. By using iterative methods, the Kohn-Sham equations can be solved self-consistently as follows (Figure 2.1):

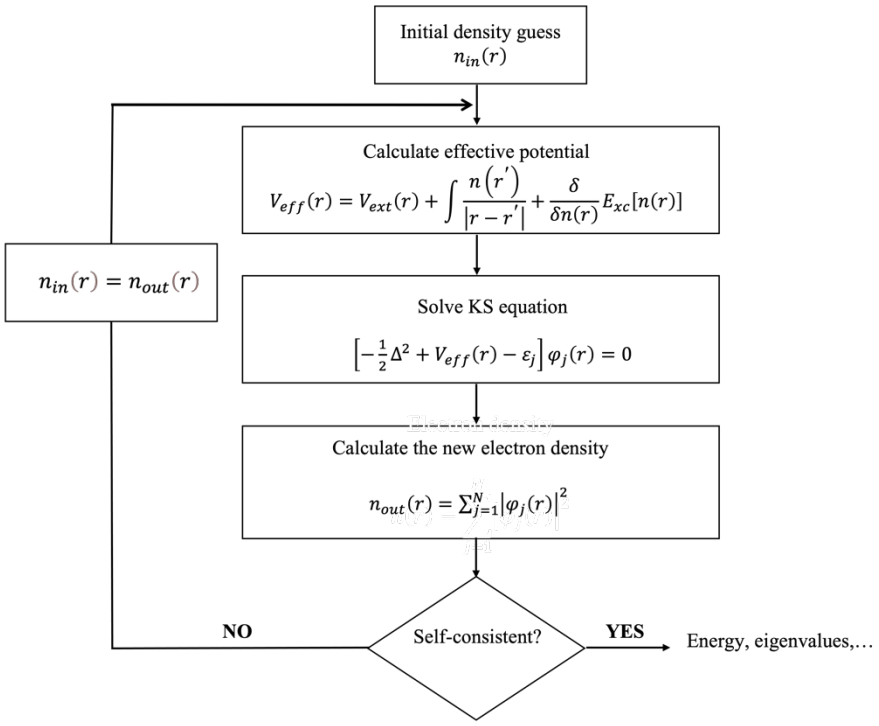

Figure 2.1. Schematic diagram of the self-consistent loop for solving Kohn-Sham equations.

First, an initial electron density, $n_{in}(r)$, is assumed (iteration 0). Then, the effective potential $V_{eff}(r)$ is constructed using equation (2.13). After that, equation (2.12) will be solved to find $\varphi_j(r)$. Finally, the new output density $n_{out}(r)$ is obtained, which should be the same as the initial one or smaller than a certain small value called tolerance. If it is not the new electron density will be used and iterated until it is. By the end of the process, the converged eigenvalues, energies, and eigenfunctions will be determined, as well as the final density.

2.5 Exchange and correlation functionals

It is not possible to determine the exchange-correlation energy $E_{xc}[n(r)]$ or exchange-correlation potential $V_{XC}(r)$. To make density functional theory DFT useful in practice, an approximation must be used. In quantum chemistry, functional development is an active research area. Consequently, several approximate functionals have been developed and are used in DFT calculations. Here I will compare two of the most used approximations, local density approximation (LDA) and generalized gradient approximation (GGA). Following that, I describe the van der Waals density functional (vdW-DF) method, which was applied to our calculations in chapters 4 and 5.

The local density approximation (LDA) [3, 7] is the simplest and oldest approximation in DFT, dating back to Kohn & Sham in 1965. Based on the LDA, the value of $E_{xc}[n(r)]$ is approximated by the exchange-correlation energy of an electron in a homogeneous electron gas with the same density. The LDA exchange-correlation functional has the form [6]:

$$E_{xc}^{LDA}[n] = \int e_{XC}\big(n(r)\big)n(r)\, dr \qquad 2.16$$

Where $e_{XC}(n)$ is the exchange-correlation energy density of the homogeneous electron gas evaluated at the local $n(r)$. Although LDA is considered a good approximation for systems where the density varies slowly, it is simply not accurate enough in a large variety of physical problems. For more accurate results, it is necessary to consider more than just the local density.

This is known as a generalized gradient approximation (GGA). In the GGAs, not only information about local electron density is included, but also information about its local gradient. Many of the GGA functionals have been developed and used. Two well-known examples are the Perdew-Wang functional (PW91) [8] and the Perdew-Burke-Ernzerhof functional (PBE) [9]. In general, the fact that GGA provides more physical information does not necessarily mean it is more accurate than LDA.

Typically, the local-density approximation (LDA) is appropriate for largely homogeneous systems, such as simple metals and semiconductors. While, in inhomogeneous systems, such as transition metals, compound metals, surfaces, and some chemical systems, semi-local-density approximations, such as generalized gradient approximations (GGA), are useful. However, previous approximations are unable to describe systems with nonlocal, long-ranged interactions, such as van der Waals (vdW) forces.

Recently, van der Waals density functional (VDW-DF) [10], has been developed and applied for several layered materials. In this functional, the exchange-correlation energy functional is written as follows:

$$E_{xc}^{vdW-DF}[n] = E_{xc}^{0}[n] + E_{c}^{nl}[n] \qquad 2.17$$

in which, $E_{xc}^{0}[n]$ is a semi-local functional and $E_{c}^{nl}[n]$ is a nonlocal functional. The part $E_{xc}^{0}[n]$ is given by the summation of local correlation [11] and gradient-correction exchange GGA using (revPBE) [12] and equation (2.17) becomes,

$$E_{xc}^{vdW-DF}[n] = E_{x}^{GGA}[n] + E_{c}^{LDA}[n] + E_{c}^{nl}[n] \qquad 2.18$$

2.6 The Pseudopotential Approximation

Pseudopotential approximation is a successful and widely used theory in relativistic electronic structure calculations and was first proposed by Hans G. A. Hellmann in 1934 [13]. Pseudopotential approximation is used to solve the many-body Schrodinger equation by reducing the number of electrons involved in the calculation while maintaining the accuracy of the results. Using pseudopotentials, it is common to focus on the behaviour of valence electrons (those in the outermost electron shells) because these electrons are responsible for most of the chemical and physical characteristics of a material. While the core electrons (those in the inner electron shells) are closely bound to the atomic nucleus and have a limited spatial extent. Therefore, they play little role in many electronic properties.

Pseudopotentials replace the core electrons and their associated potentials with an approximation [14-16]. The use of pseudopotentials allows researchers to calculate the electronic structure of much larger and more complex systems than is possible with all-electron calculations. Thus, pseudopotentials are a vital tool in helping to understand the electronic properties of materials, predict their behaviour, and design new materials for a wide range of applications, such as in the fields of materials science, chemistry, and condensed matter physics.

2.7 Conclusion

As a summary, this chapter presents a brief introduction to density functional theory (DFT), which includes the main problem of solving Schrodinger's equation for the many-body problem as well as the Hohenberg and Kohn theorems. Following this, the self-consistent Kohn and Sham equations, which represent single-particle equations are derived. Also, several approximate functionals that have been developed and used in DFT calculations is discussed.

2.8 Bibliography

[1] SHOLL DS, STECKEL JA. Density functional theory-a practical introduction. John Wiley & Sons, Inc., Hoboken, New Jersey 2009.

[2] Hohenberg P, Kohn W. Inhomogeneous Electron Gas. Physical Review 1964; 136:B864-B871.

[3] Kohn W, Sham LJ. Self-Consistent Equations Including Exchange and Correlation Effects. Physical Review 1965; 140:A1133-A1138.

[4] .Martin RM. Electronic Structure Basic Theory and Practical Methods. 2004.

[5] Combes J-M, Duclos P, Seiler R. The born-oppenheimer approximation. In: Rigorous atomic and molecular physics. Springer; 1981. pp. 185-213.

[6] Kohn W. Nobel Lecture: Electronic structure of matter—wave functions and density functionals*. Reviews of Modern Physics October 1999.

[7] Entwistle MT, Casula M, Godby RW. Comparison of local density functionals based on electron gas and finite systems. Physical Review B 2018; 97.

[8] Perdew JP, Wang Y. Accurate and simple analytic representation of the electron-gas correlation energy. Phys Rev B Condens Matter 1992; 45:13244-13249.

[9] John P. Perdew KB, Matthias Ernzerhof. Generalized Gradient Approximation Made Simple. PHYSICAL REVIEW LETTERS 1996.

[10] Dion M, Rydberg H, Schroder E, Langreth DC, Lundqvist BI. van der Waals density functional for general geometries. Phys Rev Lett 2004; 92:246401.

[11] John P. Perdew YW. Pair-distribution function and its coupling-constant average for the spin-polarized electron gas. The American Physical Society 1992.

[12] Yang YZaW. Comment on “Generalized Gradient Approximation Made Simple”. The American Physical Society 1998.

[13] N Troullier JM. Efficient pseudopotentials for plane-wave calculations. American Physical Society 1991.

[14] Zunger A, Cohen ML. Self-consistent pseudopotential calculation of the bulk properties of Mo and W. Physical Review B 1979; 19:568-582.

[15] Chelikowsky JR. The Pseudopotential-Density Functional Method (PDFM) Applied to Nanostructures.pdf. journal of Physics D: Applied Physics 2000.

[16] Louie SG, Froyen S, Cohen ML. Nonlinear ionic pseudopotentials in spin-density-functional calculations. Physical Review B 1982; 26:1738-1742.

Chapter 3.

3 Transport Theory

The purpose of this chapter is to introduce some of the fundamental concepts in quantum transport. First, the Landauer approach will be used to demonstrate that the electrical conductance of a given system is related to its transmission properties at Fermi energy in section (3.2). Then, the current flows between sites via bounds will be discussed in section (3.3). Next, the concept of a scattering matrix in one dimension will be discussed in section (3.4). Following that, the general transmission formula for the scattering region connected to two electrodes in terms of the green function will be derived in section (3.5) and the Breit-Wigner formula in section (3.6). Finally, Green's function for different systems will be presented in section (3.7).

3.1 Introduction

In a molecular device, the molecule is brought into contact with at least two external electrodes. Electrodes are connected to reservoirs that supply electrons to the system. As a voltage is applied, current flows from left to right through the molecule.

Since the 1990s, many theoretical theories have been developed to explain the current passing through nanodevices [1]. One of the most powerful approaches to describe coherent transport was the Landauer (or scattering) approach [2, 3]. Rolf Landauer proposed in 1957 that if inelastic interactions (such as electron-electron or electron-phonon interactions) can be ignored, then the transport problem can always be regarded as a scattering problem. While this assumption is reasonable for short molecules, the probability of inelastic scattering increases significantly with increasing molecule

length. The nonequilibrium Green's function is commonly used to describe the electron transport behaviour through molecules in the case of inelastic scattering [4].

3.2 The Landauer formula

Herein, we consider a system consisting of a scattering region in the centre connected to the left (L) and right (R) semi-infinite leads (or electrodes). The leads are connected to electron reservoirs, which feed the system with electrons of energy E and have electrochemical potentials $\mu_{L,R}$ of the left and right reservoirs respectively. Due to the slight difference in chemical potential between the reservoirs (μ_L-$\mu_R > 0$), electrons can move from the left to the right side through the scattering region.

Figure 3.1. Schematic diagram of Landauer's approach. This model illustrates electron transport through a molecule (scattering region), which is attached to left (L) and right (R) semi-infinite leads, which are connected to the left and right reservoirs at temperature $T_{L,R}$ and electrochemical potential $\mu_{L,R}$. In this figure I represents the incident wave, r is the amplitude of the reflected wave due to an incoming wave from the left and t is the amplitude of the transmitted wave.

According to the Landauer formula, the current flowing from left to right lead via a scattering region can be described as follows [5]:

$$I = \left(\frac{2e}{h}\right)\int_{-\infty}^{\infty} dE\ T(E)\ [f_L(E) - f_R(E)] \qquad 3.1$$

where $e = -|e|$ is the electron charge, h is Plank's constant, $T(E)$ is the transmission coefficient for electrons of energy E passing from left lead to right lead via the molecule. Assuming electrons are injected from the left (right) reservoir with Fermi distributions $f_{L,R}(E)$ corresponding to the electrochemical potentials $\mu_{L,R}$,

$$f_{L(R)}(E) = \left[e^{\left(\frac{E-\mu_{L,R}}{k_B T}\right)} + 1\right]^{-1} \qquad 3.2$$

where k_B is Boltzmann constant and T is the temperature. Equation 3.1 shows that only the difference between $f_L(E)$ and $f_R(E)$ can cause current flow between two leads, whereas in the case of $f_L(E) = f_R(E)$ leads to $I = 0$.

If a voltage difference V, or bias, between the left and right reservoirs, has been created, then

$$\mu_L = E_F + \frac{eV}{2} \qquad and \qquad \mu_R = E_F - \frac{eV}{2} \qquad 3.3$$

As a result, at zero temperature (T = 0 K) and a finite voltage, the current could be written as

$$I = \left(\frac{2e}{h}\right)\int_{E_F - eV/2}^{E_F + eV/2} dE\ T(E) \qquad 3.4$$

To obtain the electrical conductance $G = I/V$, the $T(E)$ can be averaged over an energy window of width eV centred on the Fermi energy. In the limit of zero voltage, finite temperature limit, equation (3.1) can be further approximated. Using Taylor expansion at $\mu_L = E_F$, the left Fermi distribution $f_L(E)$ is written as,

$$f(\mu_L) = f(E_F) + \frac{df}{d\mu}\bigg|_{\mu = E_F} (\mu_L - E_F) \tag{3.5}$$

similarly, to expand the right Fermi distribution $f_R(E)$ at $\mu_R = E_F$,

$$f(\mu_R) = f(E_F) + \frac{df}{d\mu}\bigg|_{\mu = E_F} (\mu_R - E_F) \tag{3.6}$$

Leading to,

$$f(\mu_L) - f(\mu_R) = \frac{df}{d\mu}\bigg|_{\mu = E_F} (\mu_L - \mu_R) \tag{3.7}$$

$$= \frac{df}{d\mu}\bigg|_{\mu = E_F} eV = -\frac{df}{dE}\bigg|_{\mu = E_F} eV$$

substituting equation (3.7) into equation (3.1), one can obtain

$$I = \left(\frac{2e^2\,V}{h}\right)\int_{-\infty}^{\infty} dE\;\; T(E)\left[-\frac{df}{dE}\bigg|_{\mu = E_F}\right] \tag{3.8}$$

therefore, the electrical conductance at the zero voltage, finite temperature limit:

$$G = \frac{I}{V} = G_0 \int_{-\infty}^{+\infty} dE\; T(E)\left(-\frac{df(E)}{dE}\right) \tag{3.9}$$

where $G_0$is the quantum of conductance and has the value,

$$G_0 = \frac{2e^2}{h} \approx 77.48\;\mu S \tag{3.10}$$

Finally, at zero voltage and zero temperature, the electrical conductance can be written as,

$$G = G_0 T(E_F) \tag{3.11}$$

Obviously, the transmission coefficient *T(E)* plays a central role in the Landauer approach. Moreover, *T(E)* is a property of the whole system, which includes the leads, the molecules, and the contacts between them.

3.3 Bond currents

This section aims to provide a formula for current flowing between two sites via a bond. Figure illustrates a one-dimensional infinite chain, where ε_j represents on-site energy and $-\gamma_j$ represents the nearest coupling.

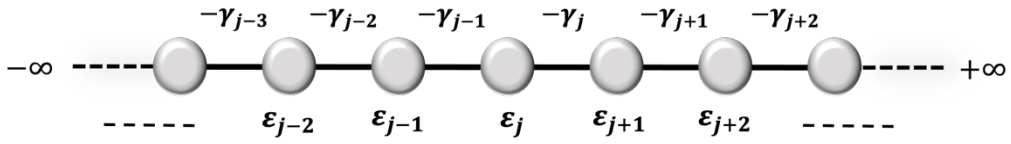

Figure 3.2. A one-dimensional infinite chain where ε_j represents on-site energy and $-\gamma_j$ represents the nearest coupling.

The time-independent Schrodinger equation for the system shown above can be expressed by the following formula:

$$\varepsilon_{j-1}\phi_{j-1} - \gamma_{j-2}\phi_{j-2} - \gamma_{j-1}\phi_j = E\phi_{j-1} \qquad 3.12$$

$$\varepsilon_j\phi_j - \gamma_{j-1}\phi_{j-1} - \gamma_j\phi_{j+1} = E\phi_j$$

$$\varepsilon_{j+1}\phi_{j+1} - \gamma_j\phi_j - \gamma_{j+1}\phi_{j+2} = E\phi_{j+1}$$

Moreover, the time-dependent Schrodinger equation is,

$$i\hbar\frac{d}{dt}\phi_j(t) = \varepsilon_j\phi_j(t) + H_{j,j-1}\phi_{j-1}(t) + H_{j,j+1}\phi_{j+1}(t) \qquad 3.13$$

The probability that an electron may be found on site *j* at a particular time *t* is determined by the following equation:

$$P_j(t) = \left|\phi_j(t)\right|^2 = \phi_j(t)\phi_j^*(t) \tag{3.14}$$

to describe the change in the probability $P_j(t)$ that an electron will be found at the site *j* at time *t*,

$$i\hbar \frac{d}{dt}P_j(t) = i\hbar \left[\phi_j(t)\frac{d}{dt}\phi_j^*(t) + \phi_j^*(t)\frac{d}{dt}\phi_j(t)\right] \tag{3.15}$$

Note that, the complex conjugate of equation (3.13), can be written as follows:

$$i\hbar\frac{d}{dt}\phi_j^*(t) = -\left[\varepsilon_j\phi_j^*(t) + H_{j,j-1}^*\phi_{j-1}^*(t) + H_{j,j+1}^*\phi_{j+1}^*(t)\right] \tag{3.16}$$

As a result of equations (3.13) and (3.16) in equation (3.15), the following result is obtained

$$\frac{d}{dt}P_j(t) = J_{(j-1\to j)} - J_{(j\to j+1)} \tag{3.17}$$

where $J_{(j-1\to j)}$ is the bond current from the site $(j-1)$to the site (j), and $J_{(j\to j+1)}$is the bond current from the site (j) to the site $(j+1)$, which are written as follows:

$$J_{(j-1\to j)} = \frac{i}{\hbar}\left[H_{j,j-1}^*\phi_j(t)\phi_{j-1}^*(t) - H_{j,j-1}\phi_j^*(t)\phi_{j-1}(t)\right] \tag{3.18}$$

and

$$J_{(j\to j+1)} = \frac{i}{\hbar}\left[H_{j,j+1}\phi_j^*(t)\phi_{j+1}(t) - H_{j,j+1}^*\phi_j(t)\phi_{j+1}^*(t)\right] \tag{3.19}$$

As a result of $H_{j,j+1} = -\gamma_j$ equation (3.19) becomes,

$$J_{(j\to j+1)} = \frac{i}{\hbar}\left[-\gamma_j\phi_j^*(t)\phi_{j+1}(t) + \gamma_j^*\phi_j(t)\phi_{j+1}^*(t)\right] \tag{3.20}$$

considering that $-i(z-z^*) = 2y = 2\,Im(z)$,

$$J_{(j\to j+1)} = \frac{2}{\hbar} Im\left[\gamma_j \phi_j^*(t)\phi_{j+1}(t)\right] \tag{3.21}$$

If $\phi_j(t)$ is an eigenstate of Hamiltonian *H,* and has the form,

$$\phi_j(t) = \psi_j e^{-iEt/\hbar} \tag{3.22}$$

As a result, $P_j(t) = \left|\phi_j(t)\right|^2 = \left|\psi_j\right|^2$, which is independent of time so, $\frac{d}{dt} P_j(t) = 0$, Therefore, the bond current has the feature,

$$J_{(j-1\to j)} = J_{(j\to j+1)} \tag{3.23}$$

This means, all bond currents are equal and currents entering and leaving any given site are equal.

As an example, consider a wave function $\psi_j = Ae^{ikj}$, using equation (3.21)

$$J_{(j\to j+1)} = \frac{2}{\hbar} Im\left[\gamma_j |A|^2 e^{ik}\right] = \frac{2\gamma_j |A|^2 \sin k}{\hbar} = v_k |A|^2 \tag{3.24}$$

where $v_k = \frac{2\gamma}{\hbar} \sin k$, is the group velocity.

3.4 Scattering matrix

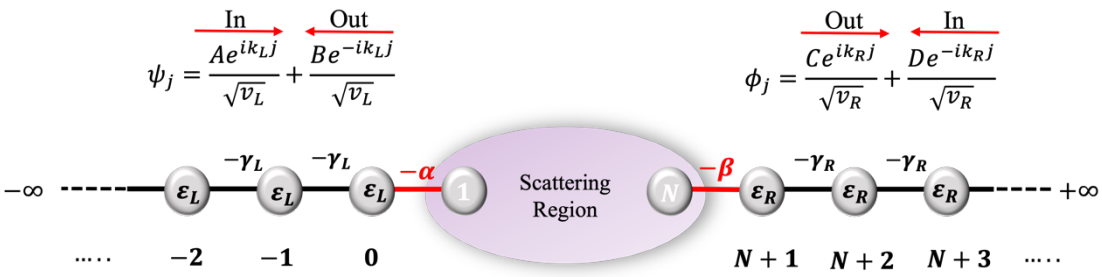

Figure 3.3. System of two different semi-infinite leads connected to a scattering region. The system consists of a scattering arbitrary region containing N sites ($j = 1, 2, \ldots, N$) connected to one-dimensional leads from left and right sides by matrix element ($-\alpha, -\beta$). The left lead has the sites ($j = -1, -2, \ldots, -\infty$) while the right

lead includes the sites ($j = N+1, N+2, \ldots, \infty$). In which, $\varepsilon_{L,R}$ stands for on-site energy and $-\gamma_{L,R}$represents the nearest coupling.

As a consequence of equation (3.11), the problem of finding the conductance becomes the problem of calculating the transmission coefficient. Now, it is useful to introduce the Scattering matrix or S-matrix that relates the transmission and reflection coefficients of the wave at the right of the scattering region with the wave at the left.

Assume a system shown in Figure 3.3 which consists of two semi-infinite leads connected to a scattering region. In which the $\varepsilon_{L,R}$ stands for on-site energy and $-\gamma_{L,R}$ stands for the nearest coupling for the left (L) and right (R) leads. For a given *E*, the wave vector $k_{L,R}$ and the group velocity $v_{L,R}$ of the plane waves on left and right leads are,

$$k_{L,R} = \cos^{-1}\left[\frac{\epsilon_{L,R} - E}{2\gamma_{L,R}}\right] \qquad \text{and} \qquad v_{L,R} = 2\gamma_{L,R}\sin k_{L,R} \tag{3.25}$$

As shown in Figure 3.3, plane waves of amplitudes A (from the left lead) and D (from the right lead) enter the scattering region. While the plane waves of amplitudes B (to the left lead) and C (to the right lead) leave the scattering region.

In the case of the left lead, the most general solution of the time-independent Schrodinger equation and the corresponding current is as follows:

$$\psi_j = \frac{Ae^{ik_L j}}{\sqrt{v_L}} + \frac{Be^{-ik_L j}}{\sqrt{v_L}} \tag{3.26}$$

$$I_L = |A|^2 - |B|^2$$

Similarly, for the right lead, one can write,

$$\phi_j = \frac{Ce^{ik_R j}}{\sqrt{v_R}} + \frac{De^{-ik_R j}}{\sqrt{v_R}} \tag{3.27}$$

$$I_R = |C|^2 - |D|^2$$

The scattering matrix is defined as a 2×2 matrix that relates the incoming and outgoing amplitudes as follows,

$$\begin{pmatrix} B \\ C \end{pmatrix} = \begin{pmatrix} S_{11} & S_{12} \\ S_{21} & S_{22} \end{pmatrix} \begin{pmatrix} A \\ D \end{pmatrix} \tag{3.28}$$

Alternatively, it can be written as follows:

$$|out\rangle = S|in\rangle \tag{3.29}$$

where,

$$|out\rangle = \begin{pmatrix} B \\ C \end{pmatrix}, \qquad S = \begin{pmatrix} S_{11} & S_{12} \\ S_{21} & S_{22} \end{pmatrix} \text{and} \qquad |in\rangle = \begin{pmatrix} A \\ D \end{pmatrix} \tag{3.30}$$

The conversation of current implies that the current in the left lead I_L is equal to the current in the right lead I_R,

$$|A|^2 - |B|^2 = |C|^2 - |D|^2 \tag{3.31}$$

Besides, the incoming current from both leads $I_{in}$is equal to the outgoing current from both leads I_{out},

$$|B|^2 + |C|^2 = |A|^2 + |D|^2 \tag{3.32}$$

Using this equation, we can prove a very significant property of the scattering matrix, namely Unitarity [6],

$$|B|^2 + |C|^2 = \begin{pmatrix} B^* & C^* \end{pmatrix} \begin{pmatrix} B \\ C \end{pmatrix} = \begin{pmatrix} A^* & D^* \end{pmatrix} S^\dagger S \begin{pmatrix} A \\ D \end{pmatrix} \tag{3.33}$$

$$= \begin{pmatrix} A^* & D^* \end{pmatrix} \begin{pmatrix} A \\ D \end{pmatrix} = |A|^2 + |D|^2$$

which simply implies that S is a unitary matrix,

$$S^{\dagger} = S^{-1} \qquad \text{or} \qquad S^{\dagger}S = I \tag{3.34}$$

To illustrate the physical meaning of matrix S elements, we shall consider two cases:

Case (1): A = 1 and D = 0.

Thus, the plane wave of the unit current enters only from the left lead. Therefore, equations (3.26) and (3.27) can be rewritten as follows:

$$\psi_j = \frac{e^{ik_L j}}{\sqrt{v_L}} + \frac{re^{-ik_L j}}{\sqrt{v_L}} \tag{3.35}$$

$$\phi_j = \frac{te^{ik_R j}}{\sqrt{v_R}}$$

As a result, the scattering matrix becomes,

$$\begin{pmatrix} r \\ t \end{pmatrix} = \begin{pmatrix} S_{11} & S_{12} \\ S_{21} & S_{22} \end{pmatrix} \begin{pmatrix} 1 \\ 0 \end{pmatrix} \tag{3.36}$$

where $r = S_{11}$ represents the reflection amplitude associated with an incoming plane wave from the left lead and $t = S_{21}$ is the corresponding transmission amplitude from the left lead to the right lead.

Case (2): A = 0 and D = 1.

In this case, the plane wave of the unit current enters only from the right lead, and the wave functions for the left and right leads are,

$$\psi_j = \frac{t'e^{-ik_L j}}{\sqrt{v_L}} \tag{3.37}$$

$$\phi_j = \frac{r'e^{ik_R j}}{\sqrt{v_R}} + \frac{e^{-ik_R j}}{\sqrt{v_R}}$$

In which $t' = S_{12}$ is the transmission amplitude associated with an incoming plane wave from the right lead and $r' = S_{22}$ is the corresponding reflection amplitude.

Consequently, the scattering matrix becomes,

$$\begin{pmatrix} t' \\ r' \end{pmatrix} = \begin{pmatrix} S_{11} & S_{12} \\ S_{21} & S_{22} \end{pmatrix} \begin{pmatrix} 0 \\ 1 \end{pmatrix} \tag{3.38}$$

Based on equations (3.36) and 3.38), the scattering matrix in terms of transmission and reflection amplitudes is

$$S = \begin{pmatrix} S_{11} & S_{12} \\ S_{21} & S_{22} \end{pmatrix} = \begin{pmatrix} r & t' \\ t & r' \end{pmatrix} \tag{3.39}$$

Because of the unitarity of the scattering matrix equation (3.34), which allows one to obtain,

$$\begin{pmatrix} 1 & 0 \\ 0 & 1 \end{pmatrix} = \begin{pmatrix} r^* & t^* \\ t'^* & r'^* \end{pmatrix} \begin{pmatrix} r & t' \\ t & r' \end{pmatrix} \tag{3.40}$$

In addition,

$$\begin{pmatrix} 1 & 0 \\ 0 & 1 \end{pmatrix} = SS^\dagger = \begin{pmatrix} r & t' \\ t & r' \end{pmatrix} \begin{pmatrix} r^* & t^* \\ t'^* & r'^* \end{pmatrix} \tag{3.41}$$

which leads to,

$$rr^* = r'^* r' \qquad \text{and} \qquad t^* t = t'^* t' \tag{3.42}$$
$$rr^* + t^* t = 1$$

Assuming that, $R(E) = rr^* \; and \; T(E) = t^* t$, are the reflection and transmission amplitudes due to a plane wave coming from the right lead. In addition, the reflection and transmission due to a plane wave coming from the left lead is $R'(E) = r'^* r' \; and \; T'(E) = t'^* t'$. Thus, we can conclude two crucial equations about reflection and transmission coefficients,

$$R(E) = R'(E) \qquad \text{and} \qquad T(E) = T'(E) \tag{3.43}$$

and

$$R(E) + T(E) = 1$$

3.5 Transmission Function

This section aims to drive the most general equation to calculate the transmission probability for a scattering region connected with 1 D electrodes from both sides [7, 8].

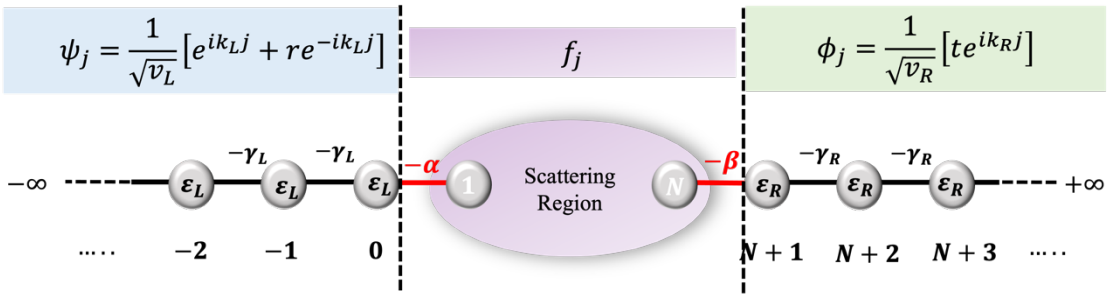

Figure 3.4. An arbitrary scattering region connected to one-dimensional leads. a system, which consists of a scattering arbitrary region containing N sites ($j = 1, 2, \dots, N$) connected to one-dimensional leads from left and right sides by matrix element ($-\alpha, -\beta$). The left lead has the sites ($j = -1, -2, \dots, -\infty$) while the right lead includes the sites ($j = N+1, N+2, \dots, \infty$). In which, $\varepsilon_{L,R}$ stands for on-site energy and $-\gamma_{L,R}$represents the nearest coupling.

Figure shows a system, which consists of a scattering arbitrary region containing N sites ($j = 1,2, \dots, N$) connected to one-dimensional leads from left and right sides by matrix element ($-\alpha, -\beta$). The left lead has the sites ($j = -1, -2, \dots, -\infty$) while the right lead includes the sites ($j = N+1, N+2, \dots, \infty$). In which, $\varepsilon_{L,R}$ stands for on-site

energy and $-\gamma_{L,R}$represents the nearest coupling. Regarding the three distinguished regions shown above, for each part the wave function can be defined in the following form:

■ for the left lead

$$\psi_j = \frac{1}{\sqrt{v_L}}\left[e^{ik_L j} + re^{-ik_L j}\right] \tag{3.44}$$

■ for the right lead

$$\phi_j = \frac{1}{\sqrt{v_R}}\left[te^{ik_R j}\right] \tag{3.45}$$

■ for the scattering region

$$f_j \tag{3.46}$$

Therefore, the Schrodinger equation for these different regions has the form,

■ for the left lead, when $(j = -1, -2, \dots, -\infty)$.

$$\epsilon_L \psi_j - \gamma_L \psi_{j-1} - \gamma_L \psi_{j+1} = E\psi_j \tag{3.47}$$

when $(j = 0)$,

$$\epsilon_L \psi_0 - \gamma_L \psi_{-1} - \alpha f_1 = E\psi_0 \tag{3.48}$$

■ for scattering region, when $(j = 1)$,

$$\sum_{l=1}^{N} H_{1l} f_l - \alpha\psi_0 = Ef_1 \tag{3.49}$$

when $(j = 2, \dots, N-1)$,

$$\sum_{l=1}^{N} H_{jl} f_l = Ef_j \tag{3.50}$$

when $(j = N)$,

$$\sum_{l=1}^{N} H_{Nl} f_l - \beta \phi_{N+1} = E f_N \tag{3.51}$$

■ for the right lead, when $(j = N+2, N+3, \dots, +\infty)$,

$$\epsilon_R \phi_j - \gamma_R \phi_{j-1} - \gamma_R \phi_{j+1} = E \phi_j \tag{3.52}$$

when $(j = N+1)$,

$$\epsilon_R \phi_{N+1} - \beta f_N - \gamma_R \phi_{N+2} = E \phi_{N+1} \tag{3.53}$$

Substituting equation (3.44) into (3.47) leads

$$E = \epsilon_L - 2\gamma_L \cos k_L \tag{3.54}$$

Similarly, substituting equation (3.45) into (3.52) leads

$$E = \epsilon_R - 2\gamma_R \cos k_R \tag{3.55}$$

Our task here is to obtain a relation between the wave function inside a scattering region f_j with the wave function outside the scattering region (ψ_j, ϕ_j). Replacing $(j = 0)$ in equation (3.47) and then comparing with equation 3.48, one can find

$$\gamma_L \psi_1 = \alpha f_1 \tag{3.56}$$

similarly, substituting $(j = N+1)$ in equation (3.52) and then comparing with equation (3.53), one can find,

$$\gamma_R \phi_N = \beta f_N \tag{3.57}$$

combining both equations (3.49) and (3.51) leads

$$(E - h)|f\rangle = |s\rangle \tag{3.58}$$

where,

$$|f\rangle = \begin{pmatrix} f_1 \\ \vdots \\ f_j \\ \vdots \\ f_N \end{pmatrix}, |s\rangle = \begin{pmatrix} -\alpha\psi_0 \\ 0 \\ \vdots \\ 0 \\ -\beta\phi_{N+1} \end{pmatrix} \quad 3.59$$

and h is the Hamiltonian of the scattering region can be written as:

$$h = \begin{pmatrix} H_{11} & H_{12} & \cdots & \cdots & H_{1N} \\ H_{21} & H_{22} & \cdots & \cdots & H_{2N} \\ \vdots & \vdots & & & \vdots \\ \vdots & \vdots & & & \vdots \\ H_{N1} & H_{N2} & \cdots & \cdots & H_{NN} \end{pmatrix} \quad 3.60$$

multiplying equation (3.58) by $(E-h)^{-1}$,leads

$$|f\rangle = g|s\rangle \quad 3.61$$

where $g = (E-h)^{-1}$, is $N \times N$ matrix called the Green's function of the scattering region and the previous equation has the form,

$$\begin{pmatrix} f_1 \\ \vdots \\ f_j \\ \vdots \\ f_N \end{pmatrix} = \begin{pmatrix} g_{11} & g_{12} & \cdots & \cdots & g_{1N} \\ g_{21} & g_{22} & \cdots & \cdots & g_{2N} \\ \vdots & \vdots & & & \vdots \\ \vdots & \vdots & & & \vdots \\ g_{N1} & g_{N2} & \cdots & \cdots & g_{NN} \end{pmatrix} \begin{pmatrix} -\alpha\psi_0 \\ 0 \\ \vdots \\ 0 \\ -\beta\phi_{N+1} \end{pmatrix} \quad 3.62$$

which can be reduced to,

$$\begin{pmatrix} f_1 \\ f_N \end{pmatrix} = \begin{pmatrix} g_{11} & g_{1N} \\ g_{N1} & g_{NN} \end{pmatrix} \begin{pmatrix} -\alpha\psi_0 \\ -\beta\phi_{N+1} \end{pmatrix} \quad 3.63$$

equivalently,

$$\begin{pmatrix} f_1 \\ f_N \end{pmatrix} = \tilde{g} \begin{pmatrix} -\alpha\psi_0 \\ -\beta\phi_{N+1} \end{pmatrix} \quad 3.64$$

in which $\tilde{g}$ is a submatrix of g, and this equation can be written as,

$$[\tilde{g}]^{-1} \begin{pmatrix} f_1 \\ f_N \end{pmatrix} = \begin{pmatrix} -\alpha\psi_0 \\ -\beta\phi_{N+1} \end{pmatrix} \quad 3.65$$

in which

$$[\tilde{g}]^{-1} = \begin{pmatrix} g_{11} & g_{1N} \\ g_{N1} & g_{NN} \end{pmatrix}^{-1} = \frac{1}{d}\begin{pmatrix} g_{NN} & -g_{1N} \\ -g_{N1} & g_{11} \end{pmatrix} \quad 3.66$$

$$\text{And} \qquad d = g_{11}g_{NN} - g_{1N}g_{N1}$$

from equation (3.44) and (3.56), one can write

$$\psi_1 = \frac{1}{\sqrt{v_L}}[2i \sin k_L] + \psi_0 e^{-ik_L} \quad 3.67$$

similarly, from equation (3.45) and (3.57),

$$\phi_N = \phi_{N+1} e^{-ik_R} \quad 3.68$$

Therefore, using equations (3.56) and (3.57), one can write

$$\begin{pmatrix} -\alpha\psi_0 \\ -\beta\phi_{N+1} \end{pmatrix} = \begin{pmatrix} \Sigma_L & 0 \\ 0 & \Sigma_R \end{pmatrix}\begin{pmatrix} f_1 \\ f_N \end{pmatrix} + \begin{pmatrix} \frac{\alpha e^{ik_L}}{\sqrt{v_L}}[2i\, sin\, k_L] \\ 0 \end{pmatrix} \quad 3.69$$

where $\Sigma_L$and Σ_R are the self-energies of the left and right lead, given by

$$\Sigma_L = \frac{-\alpha^2 e^{ik_L}}{\gamma_L} \qquad \text{and} \qquad \Sigma_R = \frac{-\beta^2 e^{ik_R}}{\gamma_R} \quad 3.70$$

Substituting equation (3.69) into (3.65),

$$([\tilde{g}]^{-1} - \Sigma)\begin{pmatrix} f_1 \\ f_N \end{pmatrix} = \begin{pmatrix} \frac{\alpha e^{ik_L}}{\sqrt{v_L}}[2i\, sin\, k_L] \\ 0 \end{pmatrix} \quad 3.71$$

Hence,

$$\begin{pmatrix} f_1 \\ f_N \end{pmatrix} = G\begin{pmatrix} \frac{\alpha e^{ik_L}}{\sqrt{v_L}}[2i\, sin\, k_L] \\ 0 \end{pmatrix} \quad 3.72$$

where,

$$G = ([\tilde{g}]^{-1} - \Sigma)^{-1} \quad 3.73$$

Since $G = \begin{pmatrix} G_{11} & G_{1N} \\ G_{N1} & G_{NN} \end{pmatrix}$, one can write this equation in full,

$$G = \left[\frac{1}{d}\begin{pmatrix} g_{NN} & -g_{1N} \\ -g_{N1} & g_{11} \end{pmatrix} - \begin{pmatrix} \Sigma_L & 0 \\ 0 & \Sigma_R \end{pmatrix}\right]^{-1} \quad 3.74$$

equivalently,

$$G = \frac{d}{D}\begin{pmatrix} g_{11} - d\Sigma_R & g_{1N} \\ g_{N1} & g_{NN} - d\Sigma_L \end{pmatrix} \quad 3.75$$

where,

$$D = (g_{11} - d\Sigma_R)(g_{NN} - d\Sigma_L) - (g_{1N}g_{N1}) \quad 3.76$$

or

$$G = \frac{1}{\Delta}\begin{pmatrix} g_{11} - d\Sigma_R & g_{1N} \\ g_{N1} & g_{NN} - d\Sigma_L \end{pmatrix} \quad 3.77$$

where,

$$\Delta = 1 - g_{11}\Sigma_L - g_{NN}\Sigma_R + \Sigma_L\Sigma_R(g_{11}g_{NN} - g_{1N}g_{N1}) \quad 3.78$$

Finally, from equation (3.45) the expression for the transmission amplitude can be written as,

$$t = \frac{ig_{N1}}{\Delta}\ \alpha\beta e^{ik_L}\sqrt{\frac{2\sin k_L}{\gamma_L}}\sqrt{\frac{2\sin k_R}{\gamma_R}}\, e^{-ik_R N} \quad 3.79$$

since the transmission probability is $T = |t|^2$, the final transmission formula in terms of the green function of the isolated scattered region has the form

$$T(E) = |t|^2 = 4\overbrace{\left[\frac{\alpha^2 \sin k_L}{\gamma_L}\right]}^{\Gamma_L}\overbrace{\left|\frac{g_{N1}}{\Delta}\right|^2}^{M}\overbrace{\left[\frac{\beta^2 \sin k_R}{\gamma_R}\right]}^{\Gamma_R} \quad 3.80$$

in which $\Gamma_L = \left[\frac{\alpha^2 \sin k_L}{\gamma_L}\right]$ are the properties of the left lead, $\Gamma_R = \left[\frac{\beta^2 \sin k_R}{\gamma_R}\right]$ are the properties of the right lead and $M = \left|\frac{g_{N1}}{\Delta}\right|^2$ is determined by both the molecule and the electrodes.

3.6 Breit-Wigner formula

This section will drive the Breit-Wigner formula and some aspects of the transmission coefficient curve. Considering isolated system contains *N* sites as shown in Figure 3.5, the time-independent Schrodinger equation can be written as

$$H|\psi_n\rangle = E_n|\psi_n\rangle \tag{3.81}$$

Figure 3.5. The isolated scattering region consists of N sites.

where the eigenstate $|\psi_n\rangle$ satisfies important properties such as

$$\langle\psi_n \mid \psi_m\rangle = \delta_{n,m} \tag{3.82}$$

$$\sum_{n=1}^{N} |\psi_n\rangle\langle\psi_n| = 1$$

In this case, the Green's function could be defined as

$$g = (E - H)^{-1} I = \sum_{n=1}^{N} (E - H)^{-1} |\psi_n\rangle\langle\psi_n| = \sum_{n=1}^{N} \frac{|\psi_n\rangle\langle\psi_n|}{(E - E_n)} \tag{3.83}$$

Now, consider the case where $E = \lambda$, in which λ is the nondegenerate eigenvalue of the Hamiltonian, equation (3.83) becomes,

$$g(E) = \frac{|\psi_\lambda\rangle\langle\psi_\lambda|}{E-\lambda} = \begin{pmatrix} g_{11} & g_{12} & \cdots & \cdots & g_{1N} \\ g_{21} & g_{22} & \cdots & \cdots & g_{2N} \\ \vdots & \vdots & & & \vdots \\ \vdots & \vdots & & & \vdots \\ g_{N1} & g_{N2} & \cdots & \cdots & g_{NN} \end{pmatrix} \quad 3.84$$

In which $|\psi_\lambda\rangle$ is the corresponding eigenstate, has the form

$$|\psi_\lambda\rangle = \begin{pmatrix} \psi_1^\lambda \\ \psi_2^\lambda \\ \vdots \\ \psi_N^\lambda \end{pmatrix} \quad 3.85$$

Using the above equations, one can determine the elements of Green's function

$$g_{11} = \frac{\left|\psi_1^\lambda\right|^2}{(E-\lambda)}, g_{NN} = \frac{\left|\psi_N^\lambda\right|^2}{(E-\lambda)}, g_{1N} = \frac{\psi_1\psi_N^*}{(E-\lambda)}, \quad 3.86$$

$$g_{N1} = \frac{\psi_N\psi_1^*}{(E-\lambda)}$$

From equation (3.78) where,

$$\Delta = 1 - g_{11}\Sigma_L - g_{NN}\Sigma_R + \Sigma_L\Sigma_R(g_{11}g_{NN} - g_{1N}g_{N1})$$

One can find by using equations (3.86) that the term $\Sigma_L\Sigma_R(g_{11}g_{NN} - g_{1N}g_{N1}) = 0$ and $g_{11}\Sigma_L - g_{NN}\Sigma_R = \frac{\psi_1^2\Sigma_L - \psi_N^2\Sigma_R}{E-\lambda}$.

This leads to,

$$\Delta = 1 - \frac{\psi_1^2\Sigma_L - \psi_N^2\Sigma_R}{E-\lambda} \quad 3.87$$

Substituting equations (3.87) and (3.88) in equation (3.80), yields

$$T(E) = 4\Gamma_L\Gamma_R\left[\frac{\psi_N^2\,\psi_1^2}{(E-\lambda)^2}\right]\frac{1}{\left(1 - \frac{\psi_1^2\Sigma_L - \psi_N^2\Sigma_R}{E-\lambda}\right)^2} \quad 3.88$$

$$T(E) = \frac{4\,\Gamma_L\Gamma_R}{(E-\lambda-\sigma_L-\sigma_R)^2 + (\,\Gamma_L+\Gamma_R)^2} \qquad 3.89$$

Finally, the transmission coefficient can be written as

$$T(E) = \frac{4\,\Gamma_L\Gamma_R}{(E-\varepsilon_n)^2 + (\,\Gamma_L+\Gamma_R)^2} \qquad 3.90$$

which is called the Breit-Wigner formula or the Lorentzian function [9]. In which $T(E)$ is the transmission coefficient of electrons, Γ_L and Γ_R are the coupling of the molecular orbital of the scattering region to the electrode and electrons pass through molecules with a certain amount of energy known as *E*. Γ_L is the properties of the left lead and it is given by

$$\Gamma_L = \left[\frac{\alpha^2 \sin k_L \psi_1^2}{\gamma_L}\right] \text{ and } \sigma_L = \left[\frac{-\alpha^2 \cos k_L \psi_1^2}{\gamma_L}\right],$$

Γ_R are the properties of the right lead and have the form

$$\Gamma_R = \left[\frac{\beta^2 \sin k_R \psi_N^2}{\gamma_R}\right] \text{ and } \sigma_R = \left[\frac{-\beta^2 \cos k_R \psi_N^2}{\gamma_R}\right],$$

In this case, the term $\varepsilon_n = (\lambda - \sigma_L - \sigma_R)$ is represented by the eigenvalue of the molecular orbitals λ which shift slightly by $(\sigma_L - \sigma_R)$, as a result of the coupling between the orbitals of the scattering region and the electrodes. Based on equation (3.90), some features will be explained below [7].

1. In case $E = \varepsilon_n$, equation (3.90) becomes:

$$T_{max}(E) = \frac{4\,\Gamma_L\Gamma_R}{(\,\Gamma_L+\Gamma_R)^2}$$

If $\Gamma_L = \Gamma_R$, then , $T_{max}(E) = 1$. This means when a symmetric molecule is coupled symmetrically to identical electrodes ($\Gamma_L = \Gamma_R$), then as shown in

Figure 3.6, the transmission coefficient will have its maximum value $T_{max}(E) = 1$.

2. In the case of the asymmetric junctions which means, $\Gamma_L \neq \Gamma_R$, for example, if $\Gamma_L \gg \Gamma_R$, then equation (3.90) becomes $T_{max}(E) \approx \frac{4\Gamma_R}{\Gamma_L} \ll 1$.

3. Finally, the Breit-Wigner formula applies when the energy of the electron is close to an eigenvalue of the isolated molecule, and when the spacing between energy levels (δ), is larger than the width of the resonance $\Gamma = \Gamma_L + \Gamma_R$ as shown in Figure 3.6.

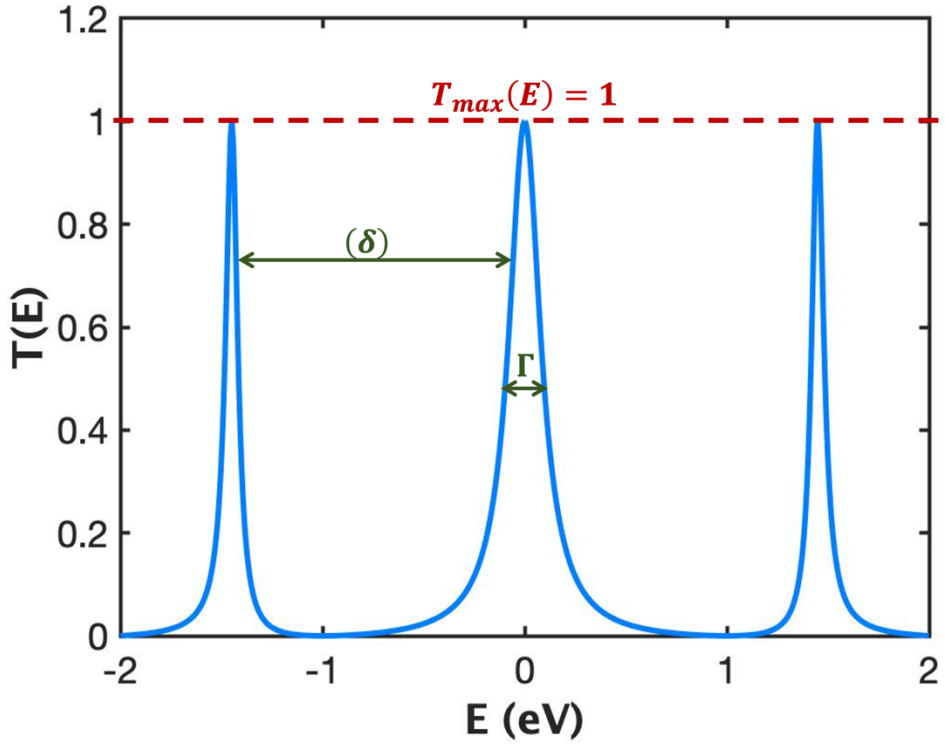

Figure 3.6. A transmission coefficient of a symmetric junction ($\Gamma_L = \Gamma_R$). In which a symmetric molecule (3 chains of atoms) is attached to identical electrodes; then the transmission peaks reach $T_{max}(E) = 1$. Also, the width of the resonances $\Gamma = \Gamma_L + \Gamma_R$, and the level spacing of the isolated molecule (δ).

3.7 Green's function

The following section starts by giving a general definition of Green's function and then highlights the relation between Green's functions and wave functions [7]. Consider a one-dimensional system, described by a time-independent Schrodinger equation,

$$H\,|\psi\rangle = E\,|\psi\rangle \tag{3.91}$$

The Green's function for this system can be defined as

$$(\,EI\;-\;H\,)\,G\;=\;I \tag{3.92}$$

in which,

$$G(E) = (EI - H)^{-1} \tag{3.93}$$

To understand the relationship between Green's functions and wave functions, it is helpful to introduce the following notation, where p^{th} is a column of *G*.

$$G_{jp} = \psi_j^{\,p} \tag{3.94}$$

$$\begin{pmatrix} \vdots \\ G_{j-2,p} \\ G_{j-1,p} \\ G_{j,p} \\ G_{j+1,p} \\ G_{j+2,p} \\ \vdots \end{pmatrix} = \begin{pmatrix} \vdots \\ \psi_{j-2}^{\,p} \\ \psi_{j-1}^{\,p} \\ \psi_j^{\,p} \\ \psi_{j+1}^{\,p} \\ \psi_{j+2}^{\,p} \\ \vdots \end{pmatrix}$$

in terms of the *j, p* elements equation (3.92) can be written as,

$$\sum_{l=1}^{N} H_{jl}\,G_{lp}(E) = E\,G_{jp}(E) - \delta_{jp} \tag{3.95}$$

or equivalently by using the notation in (3.94),

$$\sum_{l=1}^{N} H_{jl}\,\psi_j^p = E\,\psi_j^p - \delta_{jp} \qquad 3.96$$

where $\delta_{jp}$is a Kronecker delta, which is given by,

$$\delta_{jp} = \begin{cases} 1 & for \quad j = p \\ 0 & for \quad j \neq p \end{cases} \qquad 3.97$$

3.7.1 Green's function of a doubly infinite chain

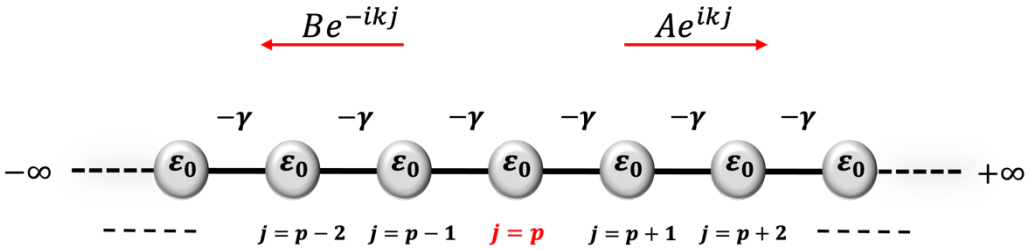

Figure 3.7. A doubly infinite chain of atoms labelled j, where ε_j represents on-site energy and $-\gamma$ represents the nearest coupling.

First, consider a doubly infinite chain shown in Figure 3.7 in which ε_j represents on-site energy and $-\gamma$ represents the nearest coupling. From equation (3.95), the Green's function for the infinite chain system is

$$\epsilon_0 G_{jp} - \gamma G_{j-1,p} - \gamma G_{j+1,p} = E G_{jp} - \delta_{jp} \qquad 3.89$$

suggesting the solution for this equation is

$$G_{jp} = \begin{cases} Ae^{ikj} & j \geq p \\ Be^{-ikj} & j \leq p \end{cases} \qquad 3.90$$

now, consider the case where $j = p$, which implies that

$$A = Ce^{-ikp} \qquad \text{and} \qquad B = Ce^{ikp} \qquad 3.100$$

Equation (3.99), becomes

$$G_{jp} = \psi_j^p = Ce^{ik|j-p|} \tag{3.101}$$

As a result, equation (3.89) can be written as follows:

$$\epsilon_0 G_{pp} - \gamma G_{p-1,p} - \gamma G_{p+1,p} = E G_{pp} - \delta_{pp} \tag{3.102}$$

Equivalent to

$$(\epsilon_0 - E)C - \gamma\, Ce^{ik} - \gamma Ce^{ik} = -1 \tag{3.103}$$

which leads

$$C = \frac{1}{2\, i\, \gamma\, sin\, k} = \frac{1}{i\, \hbar\, v(E)} \tag{3.104}$$

Finally, Green's function for a doubly infinite chain is

$$G_{jp} = \psi_j^p = \frac{e^{ik(E)|j-p|}}{i\, \hbar\, v(E)} \tag{3.105}$$

This equation corresponds to the so-called retarded Green's function.

More generally,

$$G_{jp} = \psi_j^p = \frac{e^{ik(E)|j-p|}}{i\, \hbar\, v(E)} + Ae^{ikj} + Be^{-ikj} \tag{3.106}$$

3.8 Conclusion

In summary, this chapter describes the theoretical framework of charge transport through molecules. Several theoretical concepts related to transport theory were presented. For example, the Landauer (or scattering) approach has been discussed to explain coherent transport via molecules. I have also derived the most general equation to calculate the transmission probability for a scattering region connected to a 1D electrode. Several important features of the transmission coefficient curve were explained using the Berit-Wigner formula. Finally, a general definition of Green's function is provided, as well as a discussion of the relationship between Green's functions and wave functions.

3.9 Bibliography

[1] Xiang D, Wang X, Jia C, Lee T, Guo X. Molecular-Scale Electronics: From Concept to Function. Chem Rev 2016; 116:4318-4440.

[2] Landauer R. Spatial Variation of Currents and Fields Due to Localized Scatterers in Metallic Conduction. 1957.

[3] Datta S. Electronic Transport in Mesoscopic Systems. Cambridge University Press 1995.

[4] Lin L, Jiang J, Luo Y. Elastic and inelastic electron transport in metal–molecule(s)–metal junctions. Physica E: Low-dimensional Systems and Nanostructures 2013; 47:167-187.

[5] Lambert CJ. Basic concepts of quantum interference and electron transport in single-molecule electronics. Chem Soc Rev 2015; 44:875-888.

[6] Scheer E, Cuevas JC. Molecular electronics: an introduction to theory and experiment. World Scientific; 2017.

[7] Lambert CJ. Quantum Transport in Nanostructures and Molecules, An introduction to molecular electronics. IOP Publishing 2021.

[8] al CCe. Direct calculation of the tunneling current. J. Phys. C: Solid State Phys. 4 916 1971.

[9] G. BREIT and E. WIGNER. Capture of Slow Neutrons. Phys. Rev 1936.

Chapter 4.

4 Charge transport through single-molecule bilayer-graphene junctions with atomic thickness

This work is a collaborative study involving my theoretical work at Lancaster University and experiments carried out in Prof. Wenjing Hong's group at Xiamen University. The results presented in this chapter were published in Zhao, S., Z. Y. Deng, **S. Albalawi**, Q. Wu, L. Chen, H. Zhang, X. J. Zhao, H. Hou, S. Hou, G. Dong, Y. Yang, J. Shi, C. J. Lambert, Y. Z. Tan and W. Hong (2022). "Charge transport through single-molecule bilayer-graphene junctions with atomic thickness." Chem Sci **13**(20): 5854-5859.

The van der Waals interactions (vdW) between π-conjugated molecules offer new opportunities for constructing heterojunction-based devices and investigating charge transport in heterojunctions with atomic thickness. In this chapter, I have investigated the cross-plane charge transport through three molecular bilayer graphenes (MBLGs) and molecular single-layer graphene (MSLG), sandwiched between two graphene electrodes via van der Waals interactions (vdW). The Density functional theory (DFT) results show that the cross-plane charge transport through single-molecule junctions is determined by the size and layer number of molecular graphene in these junctions. Also, the DFT calculations reveal that the charge transport through molecular graphene in these molecular junctions is sensitive to the angles between the graphene flake and peripheral mesityl groups, and those rotated groups can be used to tune the electrical conductance. This study provides new insight into cross-plane charge transport in atomically thin junctions and highlights the role of through-space interactions in vdW heterojunctions at the molecular scale.

4.1 Introduction

Two-dimensional (2D) materials such as graphene and related heterojunctions have aroused great interest due to their unique electrical properties and potential applications as quantum devices [1-3]. Multilayer heterojunctions formed from 2D van der Waals (vdW) materials are promising platforms for investigating strongly correlated phenomena, such as superconductivity [4, 5], insulativity [6, 7], and Moiré excitons [8-10], which are absent in monolayer materials. Interlayer tunnelling [11] and Coulomb interactions [12] offer an additional degree of freedom for modulating the electrical properties of multilayers [13].

Single-molecule electrical characterization techniques can be used to investigate charge transport through molecular junctions by trapping molecules with different lengths inside a nanogap [14-21]. However, when the nanogap is located between metallic electrodes, it is essential to modify the molecule by attaching anchor groups at each end, which bind to the electrodes. Such anchor groups can significantly affect transport through the parent molecular core. In contrast, by utilizing non-covalent interactions to bridge between two graphene electrodes and molecules without adding anchor groups [22, 23]. This technique takes advantage of the π-π orbital overlap between graphene electrodes and planar molecules, which can form a cross-plane transport channel for electrons passing between the graphene electrodes.

Herein, I investigate the cross-plane charge transport through molecular bilayer graphene (MBLG) using the density functional theory (DFT). Based on DFT calculations, I found that the resultant electrical conductance increased with increasing MBLG atomic number. Additionally, the molecular junctions based on single-layer molecular graphene are more conductive than double-layer molecular graphene

junctions. It is also found that the variation of conductance is due to the size dependence of the molecule's bandgap combined with the rotation angles of the peripheral mesityl groups.

4.2 Studied molecules

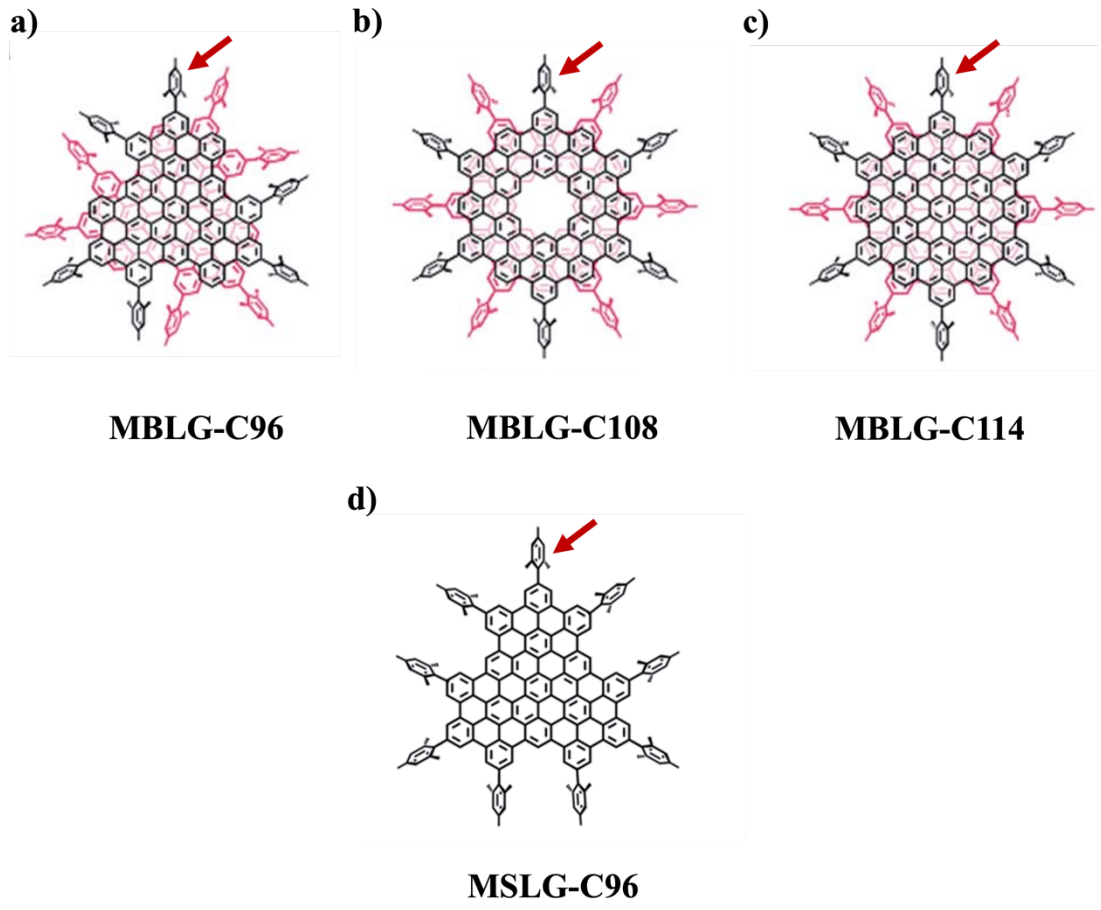

Figure 4.1. The molecular structures of molecular bilayer graphene (MBLGs) and molecular single-layer graphene (MSLG). Top row: Molecular bilayer graphene (MBLGs). a) MBLG-C96, b) MBLG-C108, c) MBLG-C114. The black and the red colours indicate the top single-layer and bottom single-layer of MBLG. The red arrows point to the peripheral mesityl groups (six mesityl groups in each layer). The Bottom row: Molecular single-layer graphene (MSLG). d) MSLG-C96. The

red arrow points to the peripheral mesityl groups (nine mesityl groups in the single layer).

Figure 4.1 (a-c) shows molecular structures of three well-defined molecular bilayer-graphene (MBLGs) denoted as MBLG-C96, MBLG-C108, and MBLG-C114 [$(C_{96}H_{24}R_6)_2$, $(C_{108}H_{24}R_6)_2$, and $(C_{114}H_{24}R_6)_2$, R= $(CH3)_3C_6H_3$ mesityl group], were synthesized [24, 25]. Compared with MBLG-C114, MBLG-C108 contains a cavity defect at its centre, and the stable bilayer structure is obtained by two vertically stacked graphene nanoflakes via π-π stacking interaction. Their peripheral mesityl groups were introduced to tune the aggregation behaviour [24, 25].

Furthermore, to investigate the influence of the layer number of molecular graphene on charge transport through molecular graphene junctions, MSLG-C96 ($C_{96}H_{24}R_9$, R=mesityl group) shown in Figure 4.1 (d) was synthesized [26], in which mesityl groups are grafted to the periphery of the graphene nanoflake to hinder the interlayer stacking. Compared with MBLG-C96, which has six peripheral mesityl groups in a single layer, MSLG-C96 has nine peripheral mesityl groups.

4.3 The geometry optimization

In this study, I used the methods described in Chapter 2 to obtain the optimised geometry of the studied molecules (see Figure 4.1 a-d) using the standard Kohn-Sham self-consistent density functional code SIESTA [27]. SIESTA uses norm-conserving pseudo-potentials to describe the core electrons and linear combinations of atomic orbitals to represent valence states. The van der Waals density functional (vdW-DF)

[28] with exchange modified by Berland and Hyldgaard [29], and a double ζ-polarized atomic-orbital basis set for carbon and hydrogen has been used. A plane wave cut-off of 200 Rydberg was used to define the real-space grid. In the case of MBLG molecules, the optimal geometries can be obtained by relaxing the molecules until all forces on the atoms are less than 0.04 eV/A°. While for MSLG-C96, the force tolerance was 0.03 eV/A°. Figure 4.2 shows the studied molecules after the relaxation process.

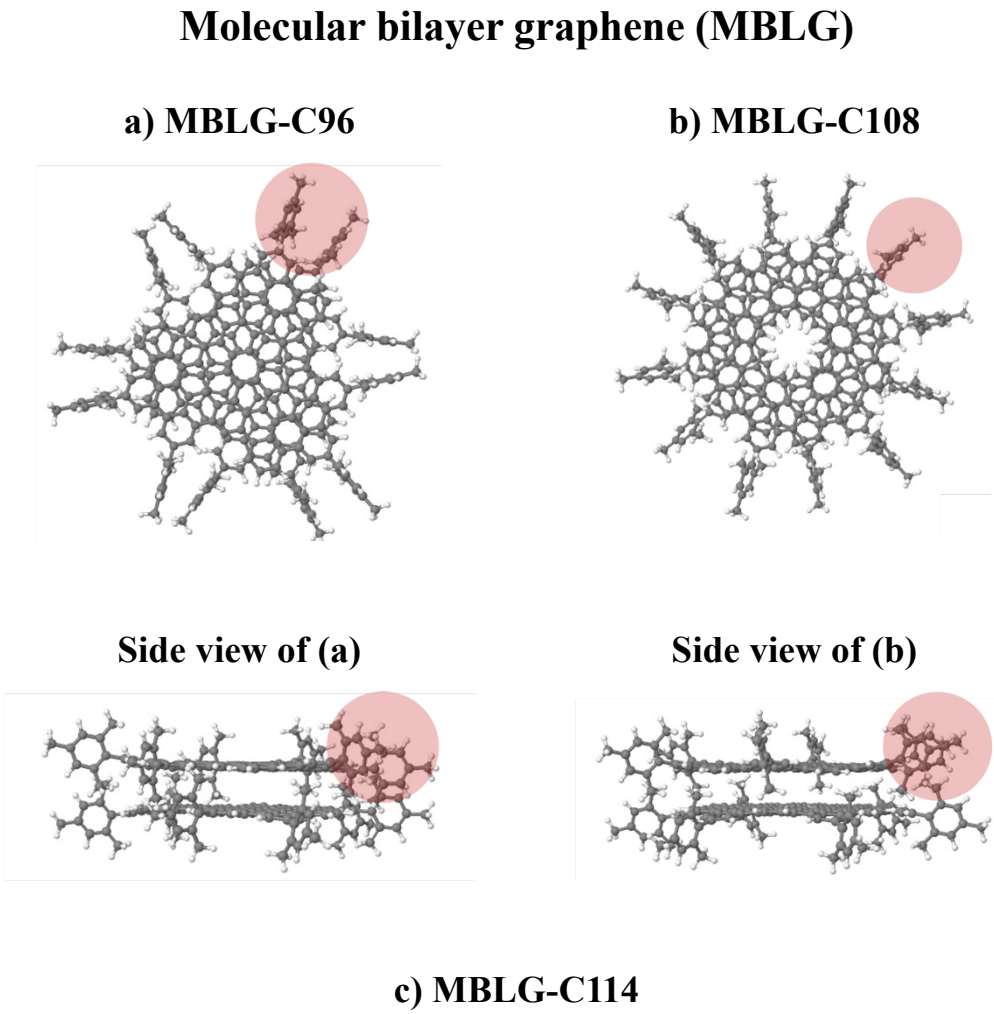

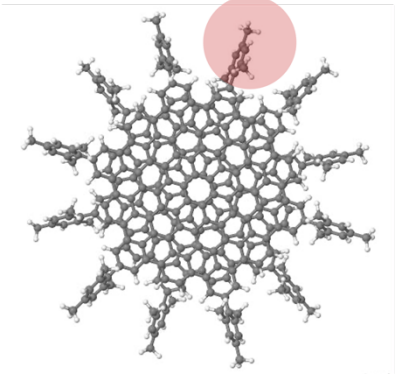

Side view of (c)

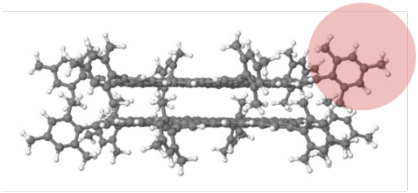

Molecular single-layer graphene (MSLG)

d) MSLG-C96

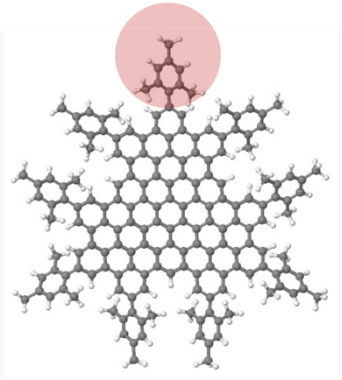

Side view of (d)

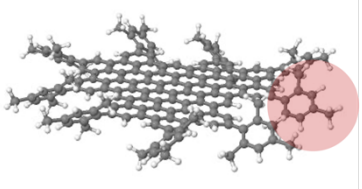

Figure 4.2. Top and side views of fully relaxed isolated molecular bilayer graphene (MBLGs) and molecular single-layer graphene (MSLG). (a) Top row: top view of MBLG-C96, bottom row: side view of MBLG-C96. (b) Top row: top view of

MBLG-C108, bottom row: side view of MBLG-C96. (c) Top row: top view of MBLG-C114, bottom row: side view of MBLG-C114, (d) Top row: top view of MSLG-C96, bottom row: side view of MSLG-C96. The red circles indicate the peripheral mesityl groups (top and side views). (Key: C = grey and H = white).

4.4 Frontier orbitals

In this section, I will plot the wave functions of the studied molecules and calculate the HOMO-LUMO gap by using the methods introduced in Chapter 2 to gain a deeper understanding of the electronic properties of these structures (see Figure 4.1).

Figures 4.3 to 4.6 show a plot of the frontier orbitals for MSLG-C96, MBLG-C96, MBLG-C108 and MBLG-C114. The highest occupied molecular orbitals HOMO, lowest unoccupied molecular orbitals LUMO, HOMO-1, and LUMO+1 along with their respective energies are shown. Moreover, the HOMO-LUMO gaps for MSLG-C96, MBLG-C96, MBLG-C108, and MBLG-C114 are found to be 1.68, 1.62, 1.88, and 1.45 respectively (see Table 4.1).

According to Table 4.1, MBLG-C96 shows a smaller HOMO-LUMO gap compared with MSLG-C96. Additionally, among the MBLG molecules, MBLG-C114 has the smallest HOMO-LUMO gap associated with the largest molecular area. However, MBLG-C108 has a larger HOMO–LUMO gap than MBLG-C96 even though the former is larger than the latter.

MSLG-C96

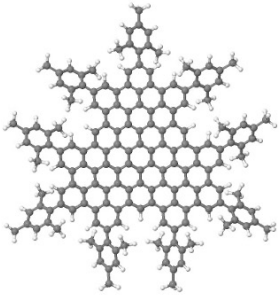

E_F = -3.75 eV

LUMO+1 **LUMO**

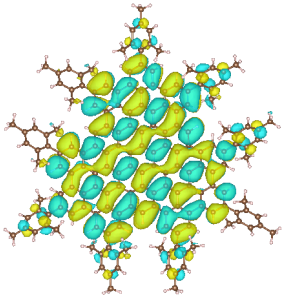

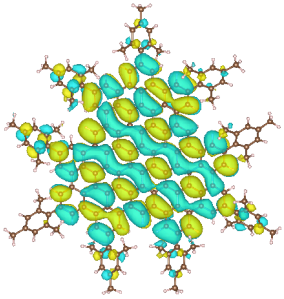

-2.78 eV **-2.79 eV**

HOMO **HOMO-1**

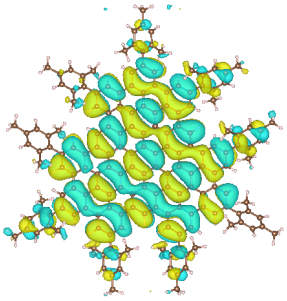

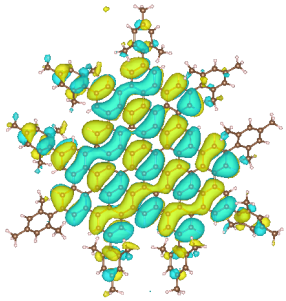

-4.47 eV **-4.47 eV**

Figure 4.3. The wave functions of MSLG-C96. LUMO+1, LUMO, HOMO, and HOMO-1 along with their respective energies.

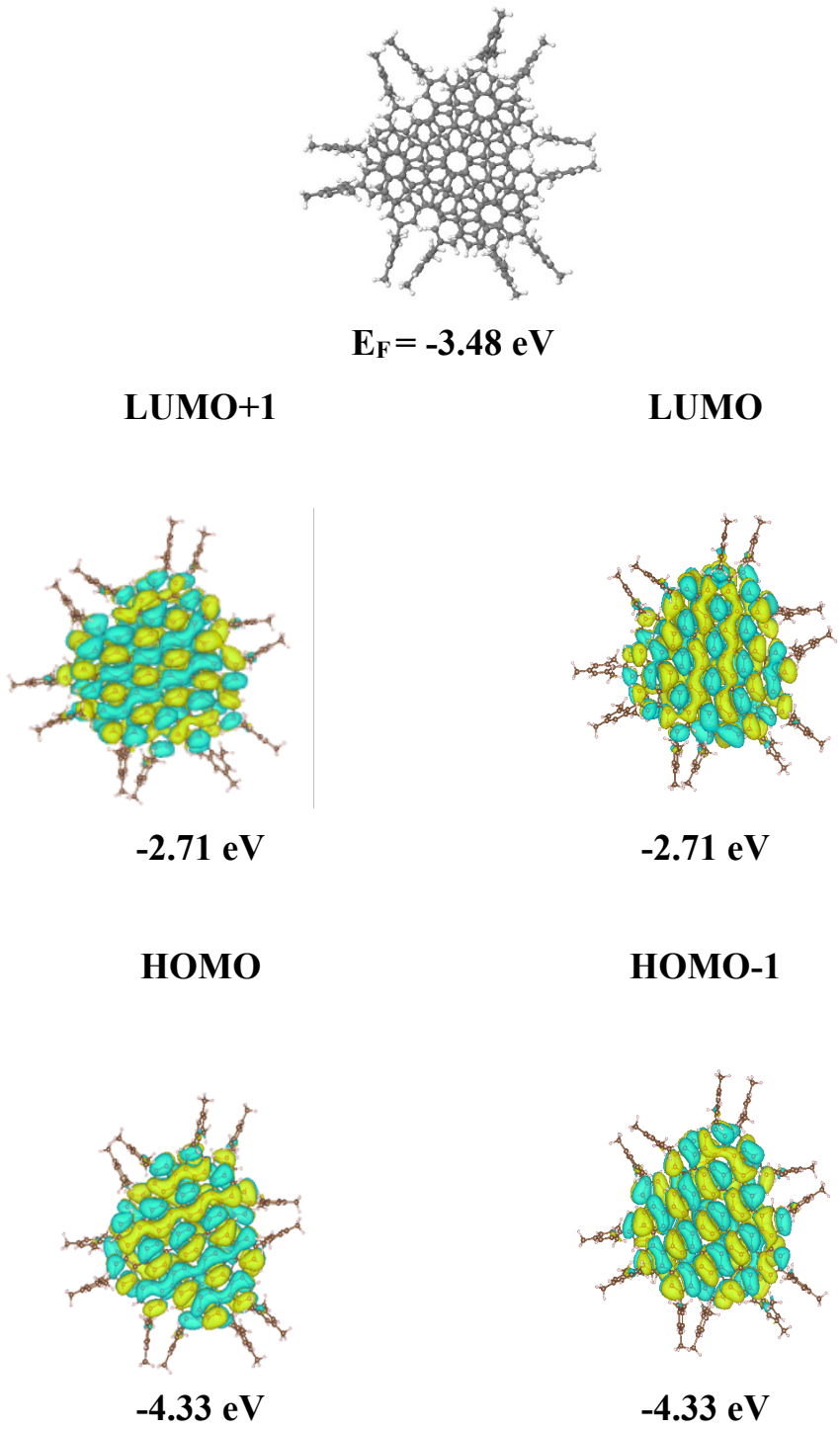

Figure 4.4. The wave functions of MBLG-C96. LUMO+1, LUMO, HOMO, and HOMO-1 along with their respective energies.

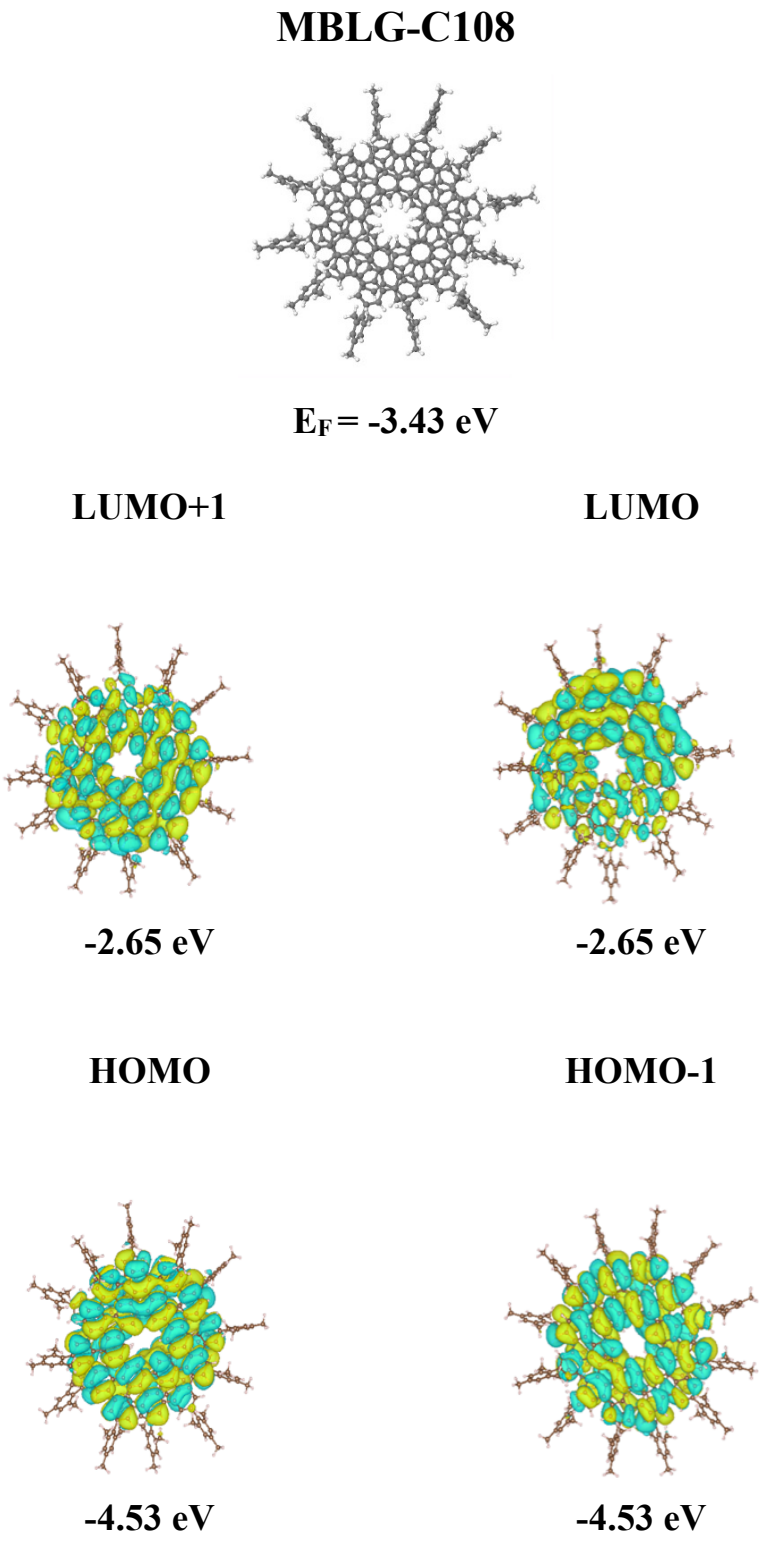

Figure 4.5. The wave functions of MBLG-C108. LUMO+1, LUMO, HOMO, and HOMO-1 along with their respective energies.

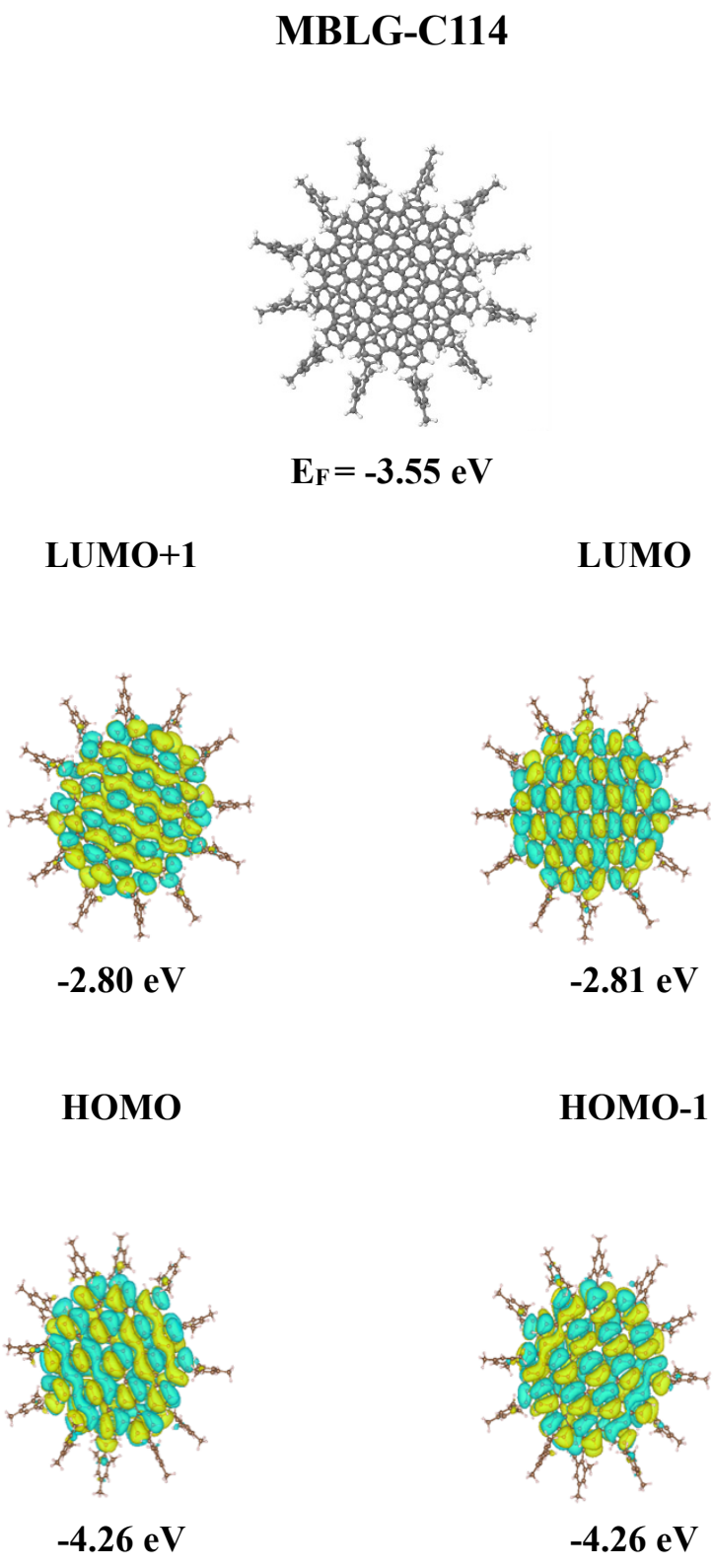

Figure 4.6. The wave function of MBLG-C114. LUMO+1, LUMO, HOMO, and HOMO-1 along with their respective energies.

The studied molecules	HOMO-LUMO gap
MSLG-C96	1.68
MBLG-C96	1.62
MBLG-C108	1.88
MBLG-C114	1.45

Table 4.1. HOMO-LUMO gap for MSLG-C96, MBLG-C96, MBLG-C108 and MBLG-C114.

4.5 The angle of the mesityl groups

In this chapter, I investigate the effect of the angle of the mesityl groups on charge transport in molecular graphene junctions. To achieve that, I studied the transport properties in which the angles between the graphene flake and mesityl groups are rotated to several angles as described below.

4.5.1 The angle of the mesityl groups of molecular bilayer graphene (MBLGs)

As mentioned in section (4.2), the molecular structure of MBLGs has 6 side mesityl groups in each single layer. To understand how these side groups affect the transport properties of MBLG molecules, I studied three cases as described below.

Case (a): the angle between the graphene flake and the mesityl groups is around 90°.

I first consider the crystal configuration case, where the angle between graphene flake and mesityl groups is approximately 90° for those MBLGs as shown in Figure 4.7.

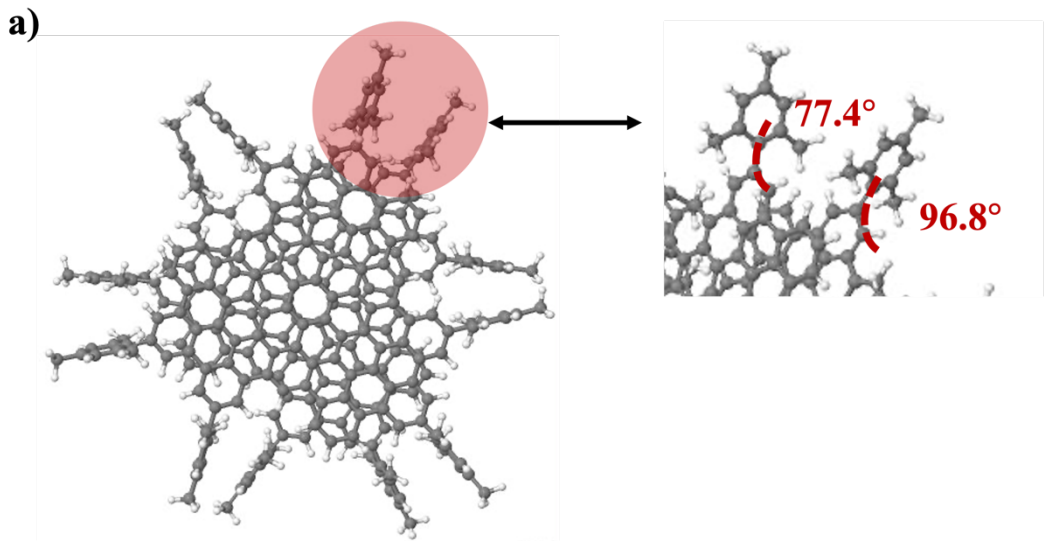

Figure 4.7. (a) The molecular structure of MBLG-C96 (left), and a close-up view of the angle between the graphene flake and the peripheral mesityl groups are close to 90° for those MBLGs (right).

Case (b): the angle between the graphene flake and the mesityl groups is 30°.

Then, I manually rotated the angle between the mesityl groups and the graphene flake of MBLG-C96, MBLG-C108, and MBLG-C114 to 30° as can be seen in Figure 4.8 (a-c). Red circles indicate the angles of the mesityl group that rotate to 30°.

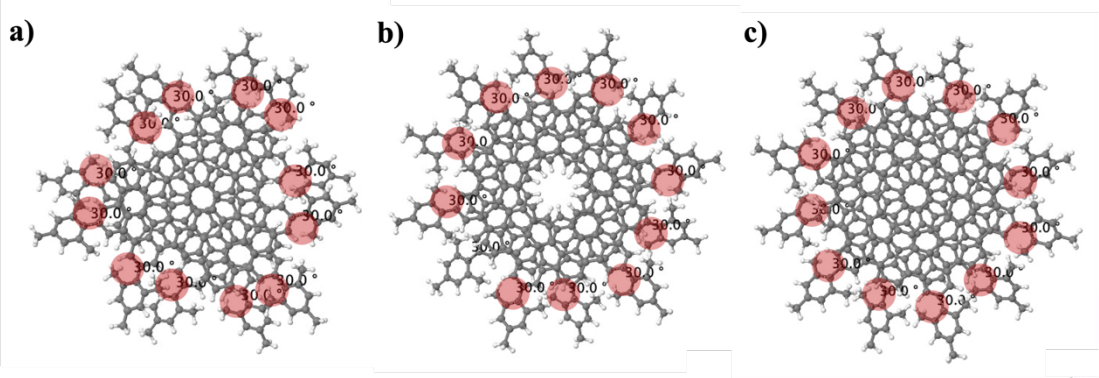

Figure 4.8. The structures of molecular bilayer graphene in which the side mesityl groups were rotated to 30°. (a) MBLG-C96 with side mesityl groups rotated to 30°. (b) MBLG-C108 with side mesityl groups rotated to 30°. (c) MBLG-C114 with side mesityl groups rotated to 30°. (The red circles are used to distinguish the side mesityl groups).

Case (c): the angle between the graphene flake and the mesityl groups is 10°.

Following that, the angle between mesityl groups and graphene flakes of MBLGs was manually rotated to 10° as shown in Figure 4.9 (a-c). Red circles indicate the angles of the mesityl group that rotate to 10°.

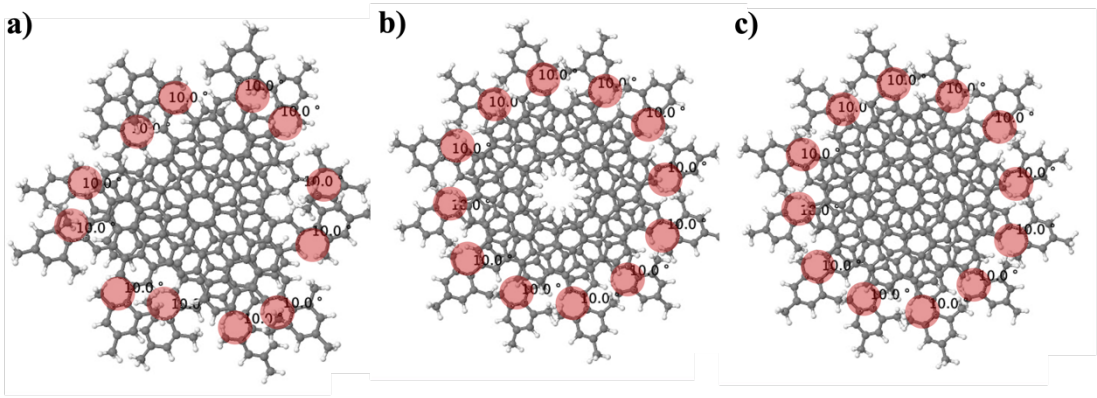

Figure 4.9. The structure of molecular bilayer graphene in which the side mesityl groups were rotated to 10° (red circles are used to distinguish the side mesityl groups). (a) MBLG-C96 with side mesityl groups rotated to 10°. (b) MBLG-C108 with side mesityl groups rotated to 10°. (c) MBLG-C114 with side mesityl groups rotated to 10°.

4.5.2 The angle of the mesityl groups of molecular single-layer graphene (MSLG)

As mentioned in section (4.2), the molecular structure of MSLG has 9 side mesityl groups. The following cases are examined to determine how these side mesityl groups affect the transport properties of MSLG-C96.

Case (d): the angle between the graphene flake and the mesityl groups is rotated to 40°, 35°, 30° and 20°.

To demonstrate the effect of side mesityl groups on charge transport in molecular graphene junctions, the side groups were rotated to 40°, 35°, 30° and 20° as shown in Figure 4.10 (a-d).

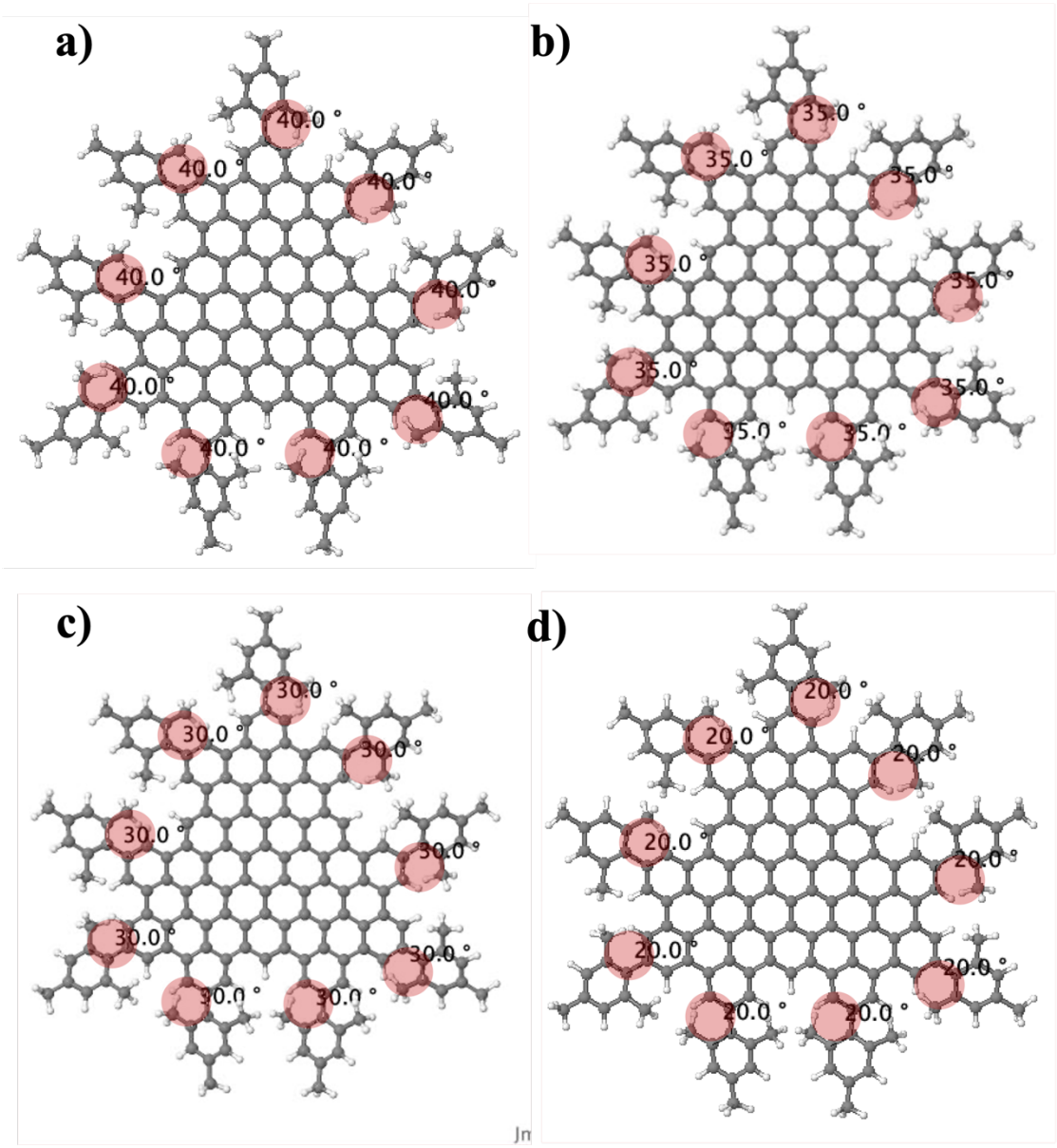

Figure 4.10. The molecular structure of MSLG-C96, in which the angle between the graphene flake and peripheral mesityl groups of MSLG-C96 is rotated to (a) 40° (b) 35° (c) 30° (d) 20° (red circles are used to distinguish the side mesityl groups).

4.6 Determine the distance by using the total energy

To better understand how the MBLG and MSLG molecules are sandwiched and interact with graphene sheets in the experiment, I used SIESTA to calculate the total energy as a function of the distance between the graphene sheet and the molecules being studied for each of the cases mentioned above in section (4.5).

4.6.1 Determine the distance of MBLGs for case (a)

In this section, I calculate the total energy as a function of the distance of MBLG-C114, MBLG-C108 and MBLG-C96, in which the angles between the graphene flake and the mesityl groups are around 90° for those MBLGs (see Figure 4.11).

Figure 4.11 illustrates the total energy (after subtracting a large negative number for simplicity) versus the distance between the lower flake of MBLG molecules and the bottom graphene sheet (see the purple arrow in (a)). According to Figure 4.11 (b), the minimum total energies for MBLG-C96, MBLG-C108 and MBLG-C114 are found at 6.3 Å with total energy -154795.8 eV (blue curve), 6.4 Å with total energy -158688 eV (orange curve), and 6.2 Å with total energy -160355.3 eV (purple curve), respectively.

4.6.2 Determine the distance of MBLGs for case (b)

The total energy E (after subtracting a large negative number for simplicity) versus the distances between the bottom graphene sheet and lower graphene flake of MBLGs with the side groups rotated to 30° relative to the graphene flake is calculated as shown in Figure 4.12 (see the purple arrow in a). As can be seen in Figure 4.12 (b), the optimum distance, (which corresponds to the minimum of the total energy curve), for MBLG-C96 is 4.7 Å with total energy -154740.3 eV (blue curve), and for both MBLG-C108 and MBLG-C114 is 4.9 Å with total energy -160337.4 eV (purple curve).

4.6.3 Determine the distance of MBLGs for case (c)

In this section, I calculate the optimum distance, (which corresponds to the minimum of the total energy curve), between the lower flake of MBLG molecules, with their side groups rotated to 10°, and the bottom graphene sheet (see the purple arrow in Figure 4.13 a). Figure 4.13 (b) illustrates the total energy (after subtracting a large negative number for simplicity) versus the distance between the lower flake of MBLG molecules, with their side groups rotated to 10°, and the bottom graphene sheet. It is found that the minimum total energies for MBLG-C96 are found at 4.4 Å with total energy -154775 eV (blue curve), and for both MBLG-C108 and MBLG-C114 are found at 4.3 Å with total energy -160336.3 eV (purple curve).

4.6.4 Determine the distance of MSLG for case (d)

In this section, I determined the optimum distance, (which corresponds to the minimum of the total energy curve), between the bottom graphene electrode and the MSLG.

As can be seen in Figure 4.14 (a), MSLG-96 with side groups rotated to different angles lies above the graphene sheet. Then, the total energy against the distance between the graphene flake of MSLG-C96 and the bottom graphene sheet has been plotted (see the purple arrow in a). Figure 4.14 (b) shows that the minimum total energies for MBLG-C96 at 20° (blue curve), 30°(orange curve), 35°(purple curve), and 40° (green curve) were found at distances of 3.9 Å, 4.3 Å, 4.5 Å, and 4.7 Å with total energies -134838.5 eV, -134844.1 eV, -134846.2 eV and -134846.6 eV respectively.

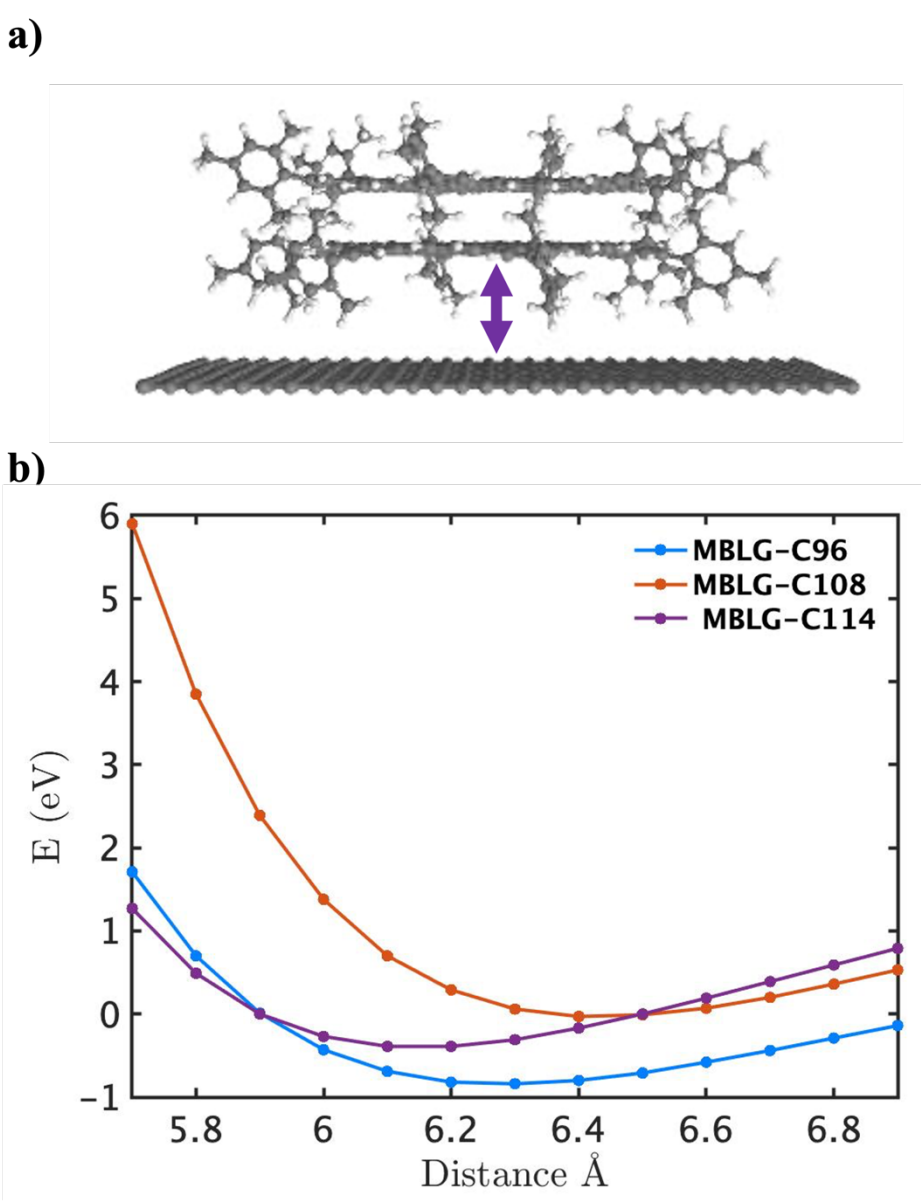

Figure 4.11. Total energy versus distance of MBLG molecules in which the peripheral mesityl groups are close to 90°. (a) The MBLG-C114 molecule is positioned above the graphene electrode. (b) Evolutions of total energy (after subtracting a large negative number for simplicity) versus distance between the graphene flake of MBLG and the bottom graphene sheet for MBLG-C96, MBLG-C108, and MBLG-C114.

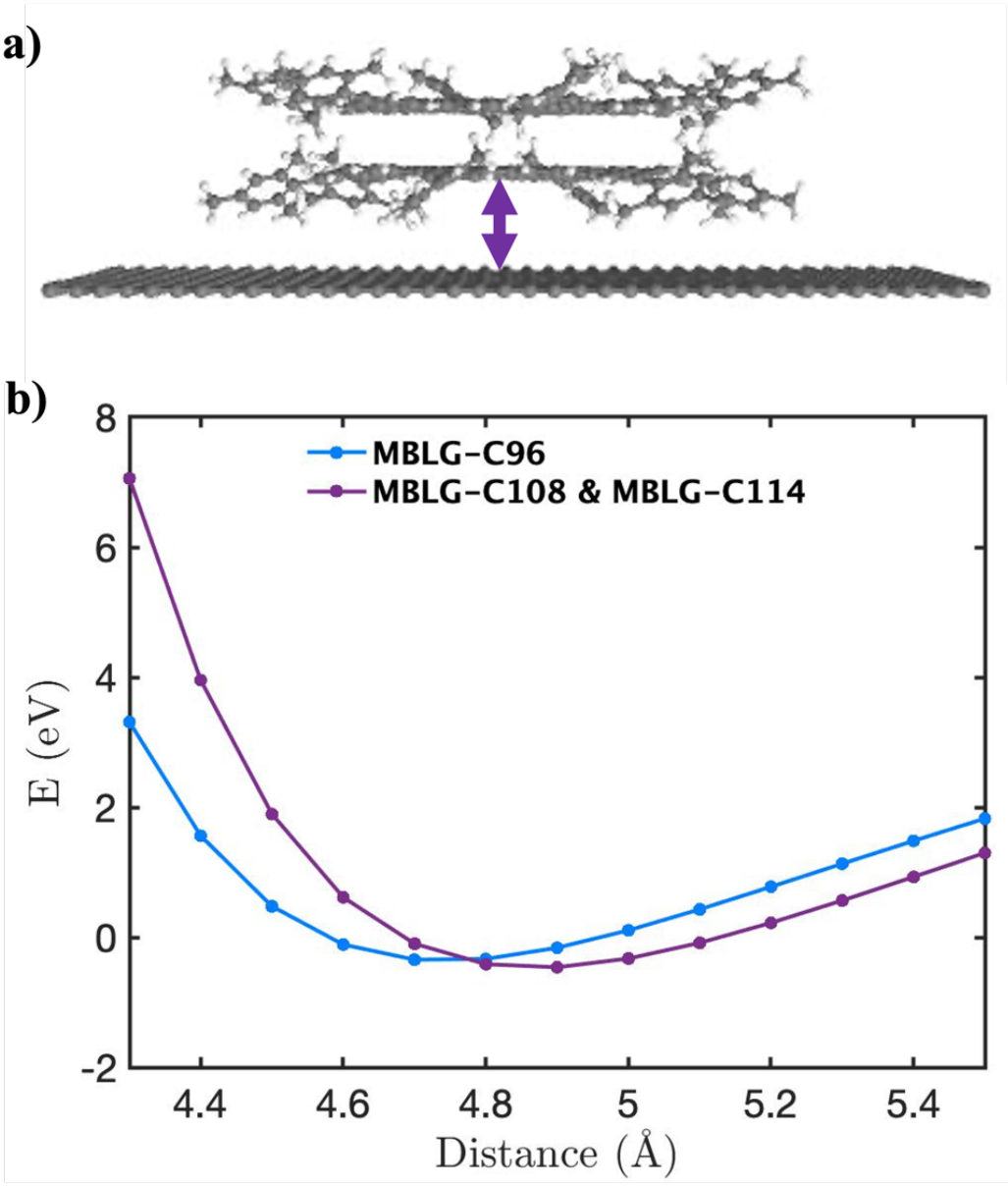

Figure 4.12. Total energy versus distance of MBLG molecules in which the peripheral mesityl groups are rotated to 30°. (a) The MBLG-C114 molecule where the side mesityl groups rotated to 30° is positioned above the graphene electrode. (b) Evolutions of total energy versus distance between graphene flake of MBLG and one graphene sheet for MBLG-C96, MBLG-C108, and MBLG-C114 where the side groups rotated to 30°.

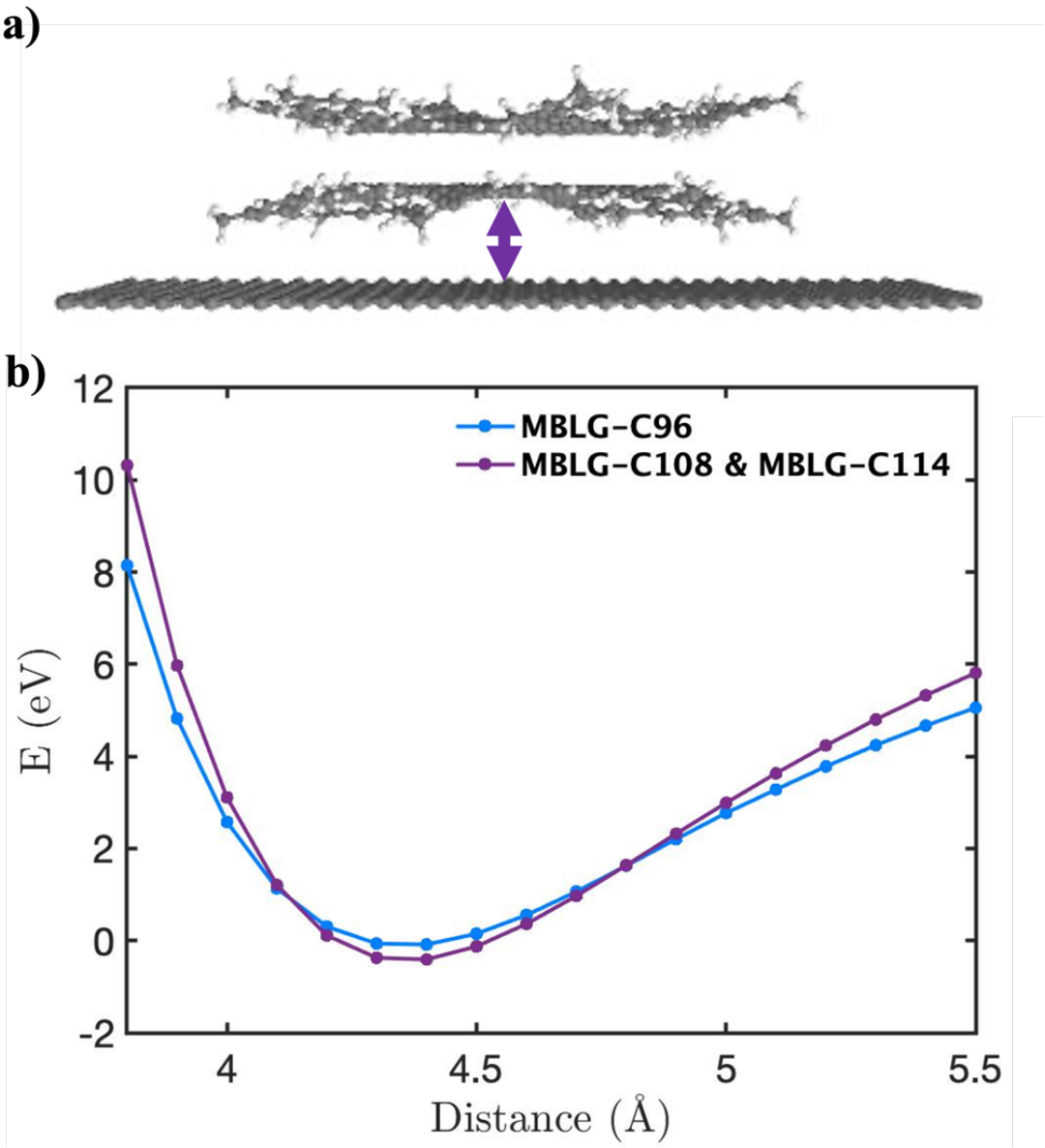

Figure 4.13. Total energy versus distance of MBLG molecules in which the peripheral mesityl groups are rotated to 10°. (a) The MBLG-C114 molecule where the side groups rotated to 10° is positioned above the graphene electrode. (b) Evolutions of total energy versus distance between graphene flake of MBLG and one graphene sheet for MBLG-C96, MBLG-C108, and MBLG-C114 where the side groups rotated to 10°.

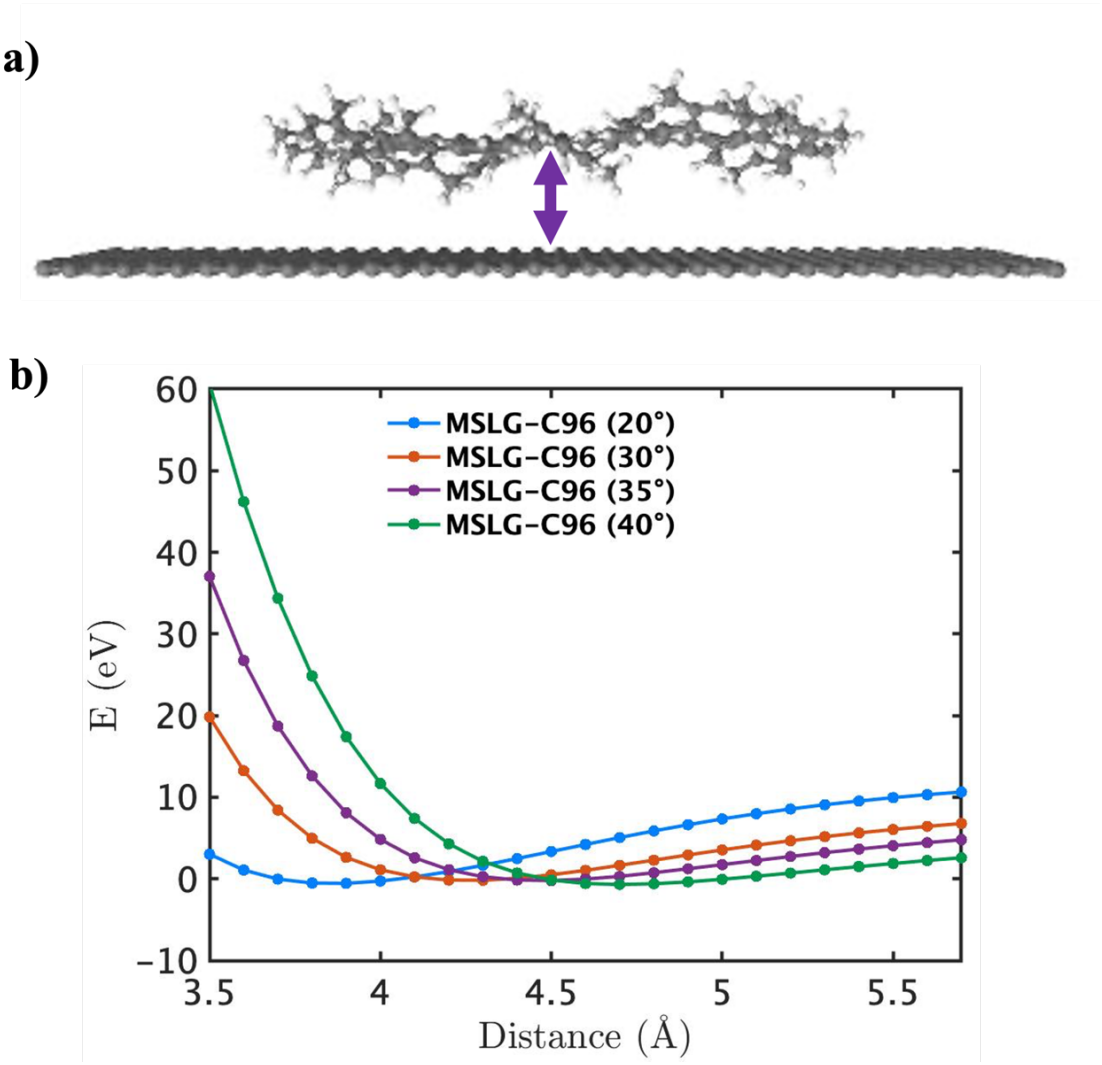

Figure 4.14. Total energy versus distance of MSLG-C96 in which the peripheral mesityl groups are rotated to 40°, 35°, 30°, and 20°. (a) The MSLG-C96 molecule where the side groups rotated to 20°, 30°, 35°, and 40° is positioned above the graphene electrode. (b) Total energy (after subtracting a large negative number for simplicity) versus distance between the graphene flake of MSLG-C96 and the bottom graphene sheet, in which the side groups of MSLG are rotated to different angles 20°, 30°, 35°, and 40°, relative to the flake.

Tables 4.2, 4.3, 4.4 and 4.5 summarize the results discussed above in this section.

MBLG molecules (in which the peripheral mesityl groups are close to 90°)		
	The distance($A°$)	**The total energy(eV)**
MBLG-C114	6.2	-160355.3
MBLG-C108	6.4	-158688
MBLG-C96	6.3	-154795.8

Table 4.2. Total energy versus distance of MBLG molecules in which the peripheral mesityl groups are close to 90°.

MBLG molecules (in which the peripheral mesityl groups are rotated to 30°)		
MBLG-C114	4.9	-160337.4
MBLG-C108	4.9	-160337.4
MBLG-C96	4.7	-154740.3

Table 4.3. Total energy versus distance of MBLG molecules in which the peripheral mesityl groups are rotated to 30°.

MBLG molecules (in which the peripheral mesityl groups are rotated to 10°)		
MBLG-C114	4.3	-160336.3
MBLG-C108	4.3	-160336.3
MBLG-C96	4.4	-154775

Table 4.4. Total energy versus distance of MBLG molecules in which the peripheral mesityl groups are rotated to 10°.

MSLG-C96		
	The distance($A°$)	**The total energy(eV)**
40°	4.7	-134846.6
35°	4.5	-134846.2
30°	4.3	-134844.1
20°	3.9	-134838.5

Table 4.5. Total energy versus distance of MSLG-C96 in which the peripheral mesityl groups are rotated to 40°, 35°, 30°, and 20°.

4.7 Configurations between MBLGs (MSLG) molecules and graphene sheets

The DFT calculations I performed consider nine different configurations of MBLGs (MSLG) molecules and graphene sheets, as shown in Figure 4.15 (a-d) and Figure 4.16 (a-e). The colours are used to distinguish the molecule (in this case MBLG-C114) from the graphene sheets (grey colour). Below I will describe the steps involved in obtaining each geometry.

There are four configurations between the MBLG-C114 and the graphene sheets shown in Figure 4.15. (a) shows the Top-Hollow position (blue colour), where the C atom of the graphene sheet overlaps the centre of MBLG-C114, (b) the Hollow-Hollow position (orange colour) in which the centre of MBLG-C114 was shifted from the position in (Figure 4.15 a) to up by 1.42 Å, (c) the centre of MBLG-C114 was shifted from the position in (Figure 4.15 a) to the right by 1.23 Å (purple colour).

Next, I select the geometry shown in (Figure 4.15 b) and rotate the molecule inside to several different angles. Based on the geometry shown in Figure 4.15 (b), the molecule inside is rotated by 10° to obtain Figure 4.15 d (green colour).

Figure 4.16 shows another different configuration between the MBLGs (MSLG) molecules and the graphene sheets. Using the junction shown in Figure 4.15 (b), the molecule inside is rotated by 20°, 30°, 40°, 50° and 60° to obtain the geometry in Figure 4.16 a (yellow colour), b (light blue colour), c (dark grey colour), d (pink colour) and e (light green colour), respectively.

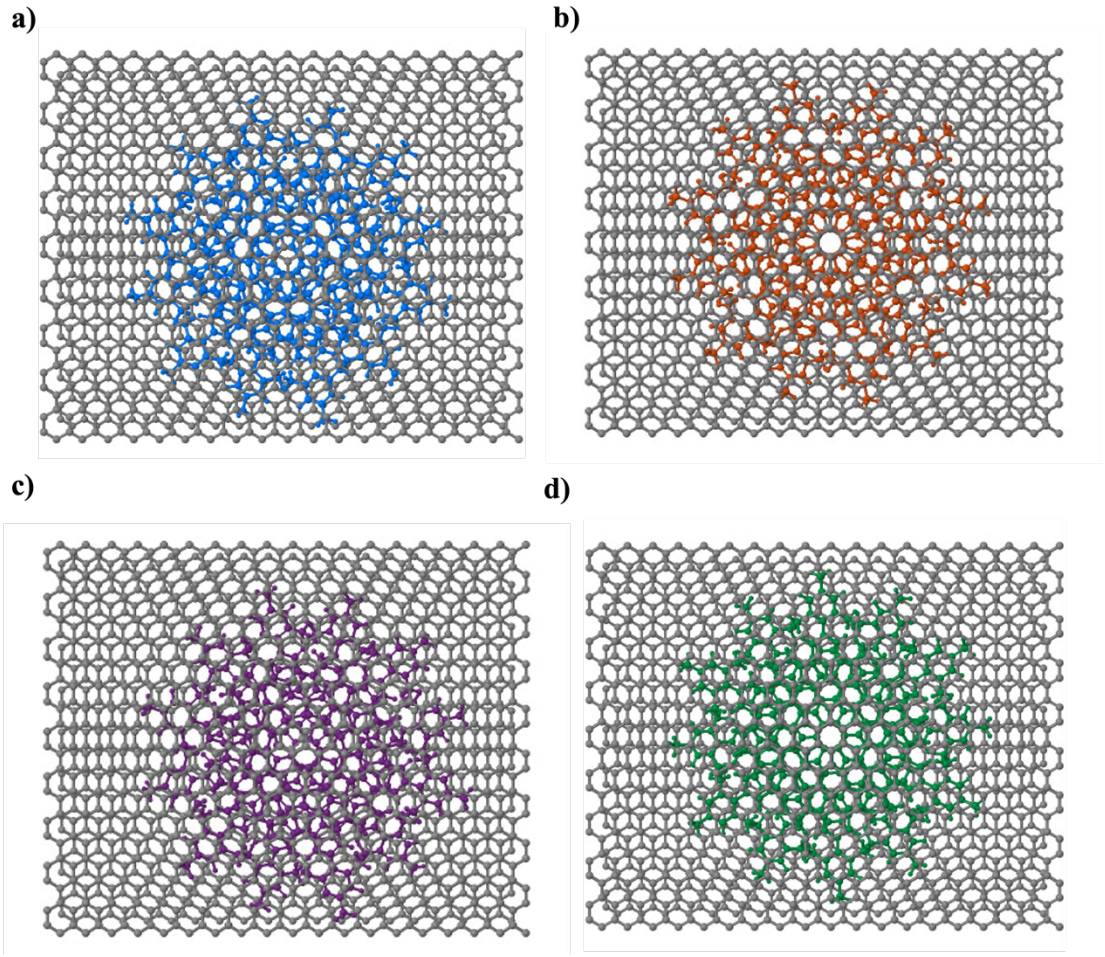

Figure 4.15. Different configurations between MBLGs (MSLG) molecules and the graphene sheets from a top view. The colours are used to distinguish the molecule (in this case MBLG-C114) from the graphene sheets (grey colour).

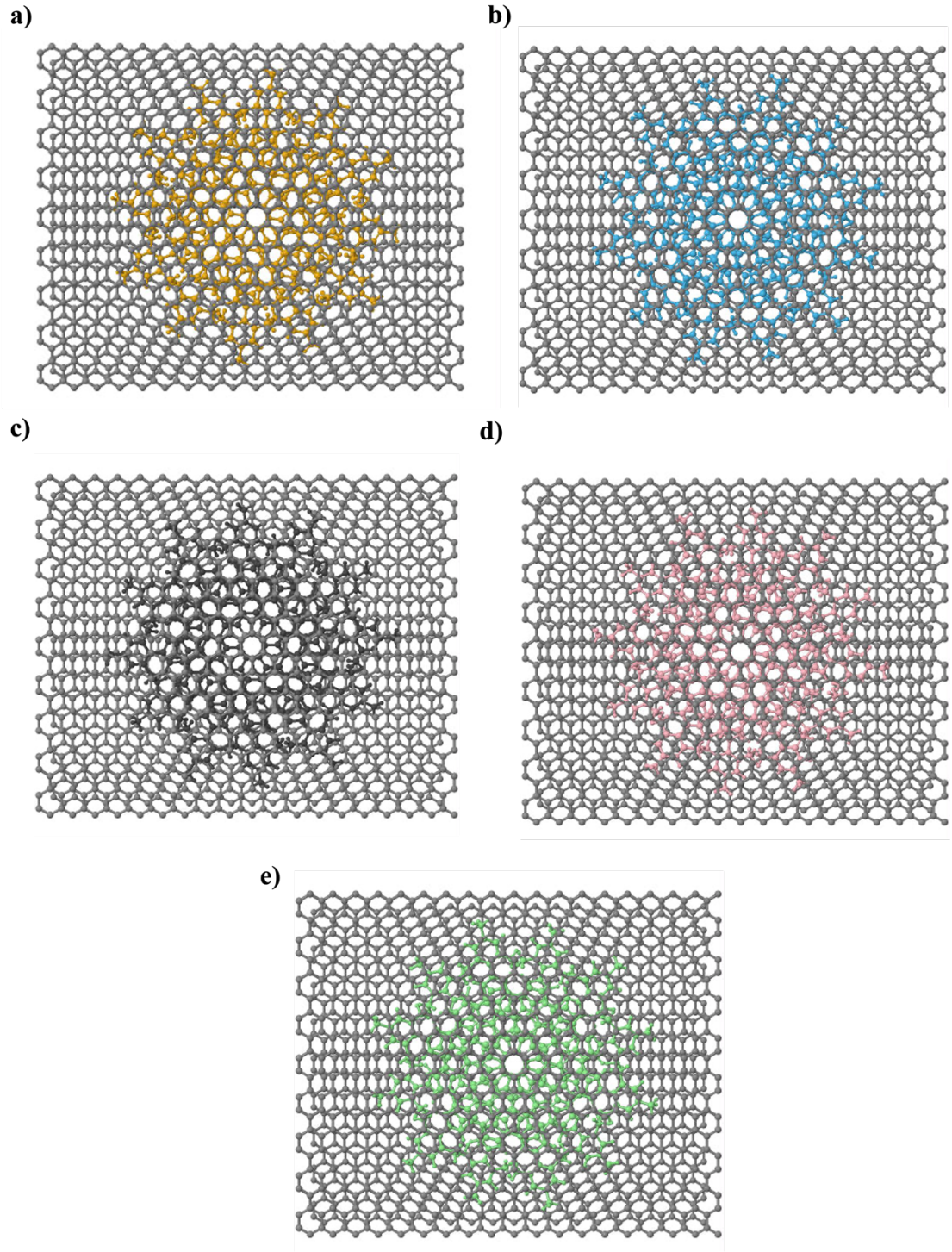

Figure 4.16. Different configurations between MBLGs (MSLG) molecules and the graphene sheets from a top view. The colours are used to distinguish the molecule (in this case MBLG-C114) from the graphene sheets (grey colour).

4.8 Transmission function calculations

The purpose of this section is to calculate the transmission function of MBLG-C96, MBLG-C108, MBLG-C114, and MSLG-C96 for each of the cases discussed in section (4.5). For each structure, the transmission coefficients $T(E)$ were calculated using the Gollum quantum transport code [30], which uses the DFT mean-field Hamiltonian and overlap matrices from SIESTA.

To begin, I will describe the graphene sheet and the leads I used to perform my DFT calculations. Figure 4.17 shows the graphene sheets and the green colour is used to distinguish the four leads (or electrodes) which form the electrodes in the calculations. Each graphene sheet is extended to ± infinity in the z-direction, while in the y-direction, periodic boundary conditions are used. In Figure 4.17 (b), the finite graphene sheet is shown with a width of 45.52 Å and a length of 36.92 Å. Also, the lead on the right contains 72 atoms.

The electrons are injected from leads 1 and 2 and collected by leads 3 and 4 (see the purple arrows in Figure 4.17 a). In other words, the transmission function curves plotted in this section represent a summation of the transmission function from lead 1 to lead 3 and lead 4 ($T_{1,3}$+$T_{1,4}$), together with the transmission function collected from lead 2 to lead 3 and lead 4 ($T_{2,3}$+$T_{2,4}$). The MBLGs and MSLG-C96 are placed between the two graphene sheets and their electrical properties are calculated as described below.

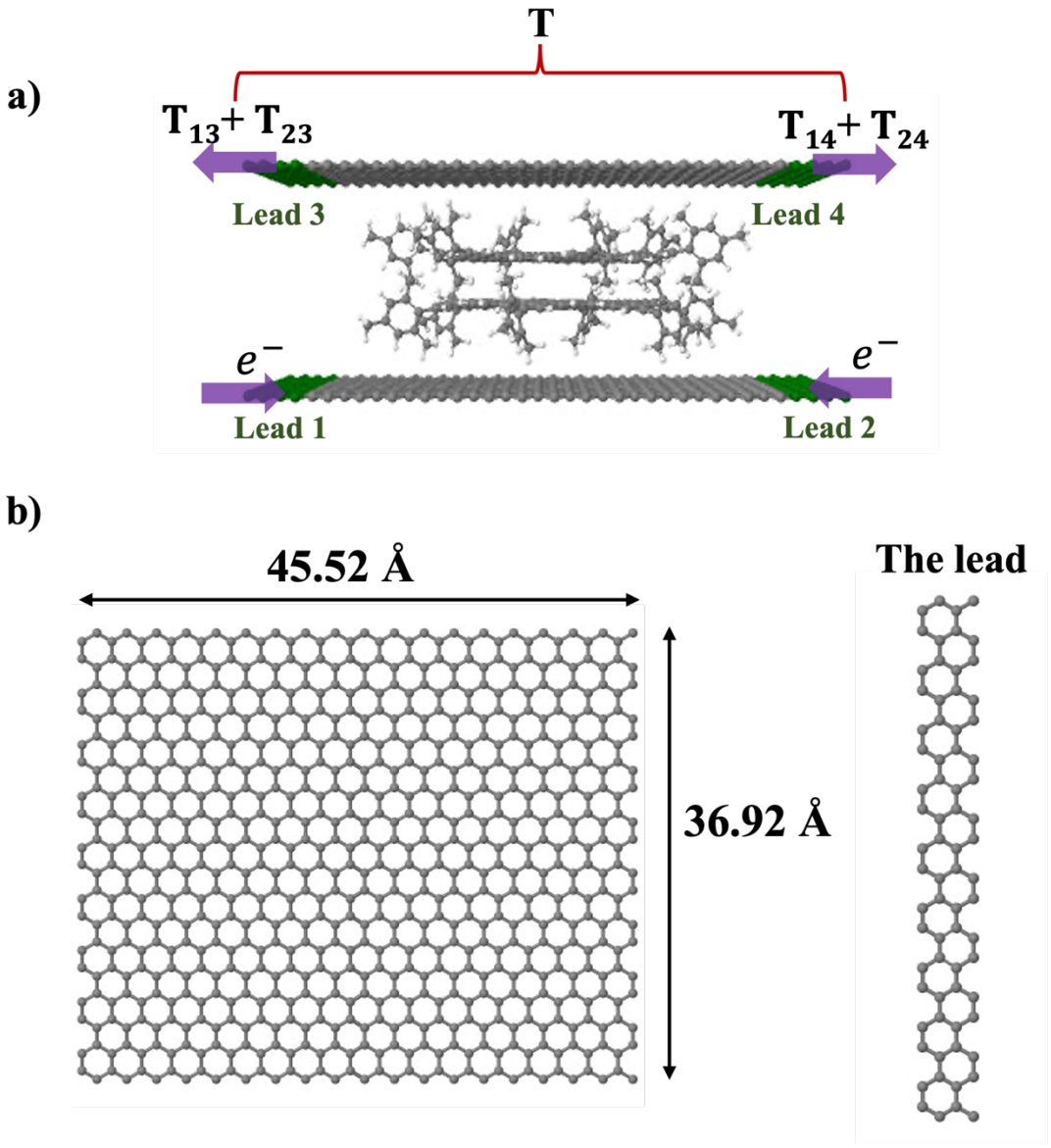

Figure 4.17. (a) Sandwiched structures of the molecular junction based on MBLG-C114, the green colour is used to distinguish lead 1, 2, 3 and 4 which form the electrodes in the calculations. The electron is injected from lead 1 and 2 and the transmission coefficient T is collected by lead 3 and 4 (the transmission function curves represent the summation of $T = T_{13}+T_{14}+T_{23}+T_{24}$). (b) The finite graphene sheet (left), The lead (right).

4.8.1 Transmission function calculations of MBLGs for case (a)

Using the distances given in Table 4.2, I constructed molecular graphene junctions based on MBLG-C114, MBLG-C108, and MBLG-C96, in which the angles between the graphene flake and the mesityl groups are around 90° (case a). Then, the transmission coefficients of MBLG molecules are calculated as shown in Figure 4.18.

Figure 4.18 (b) shows the transmission spectra of MBLG-C96 (blue curve), MBLG-C108 (orange curve), and MBLG-C114 (purple curve). The results show that MBLG-C114 has the highest transmission coefficient, originating from the smallest HOMO–LUMO gap and the largest molecular area (see Table 4.1). MBLG-C108 possesses a higher transmission compared to MBLG-C96, due to a stronger coupling with electrodes (indicated by wider HOMO and LUMO transmission resonances) even though the former has a larger HOMO–LUMO gap than the latter as shown in Table 4.1. However, the results show low conductance (10^{-10}~10^{-9} G_0) between the two graphene sheets compared to the experimental values (10^{-5}~10^{-4} G_0) (see Figure 4.35 for the experimental data). Consequently, it is estimated that the angles between the side mesityl groups and the graphene flake of MBLGs would be smaller than 90°.

4.8.2 Transmission function calculations of MBLGs for case (b)

In this section, the transmission functions of molecular graphene junctions formed from MBLG-C114, MBLG-C108, and MBLG-C96 with their side mesityl groups rotated to 30° (case b) are calculated using the distances shown in Table 4.3, for the nine configurations shown in Figures (4.15 and 4.16). The transmission spectra of MBLG-C96, MBLG-C108 and MBLG-C114 f with their side mesityl groups rotated to 30°, for configurations described in Figure 4.15, can be seen in Figures 4.19, 4.21 and 4.23.

Also, Figures 4.20, 4.22 and 4.24 present the transmission spectra of MBLG-C96, MBLG-C108 and MBLG-C114 with their side mesityl groups rotated to 30° for configurations described in Figure 4.16. Results demonstrate that all junctions of 30° exhibit transmission functions between 10^{-7} G_0 and 10^{-6} G_0 at Fermi energy E_F, which are higher than those in the previous section (4.8.1) (see Figure 4.18).

4.8.3 Transmission function calculations of MBLGs for case (c)

For each of the nine configurations shown in Figures (4.15 and 4.16), the distances shown in Table 4.4 for the molecular graphene junctions containing MBLG-C114, MBLG-C108, and MBLG-C96 with their side mesityl groups rotated to 10° (case c) are used to calculate the transmission functions.

The transmission spectra of MBLG-C96, MBLG-C108 and MBLG-C114 with their side mesityl groups rotated to 10° are shown in Figures 4.25, 4.27, and 4.29 for configurations described in Figure 4.15. Further, the transmission spectra of MBLG-C96, MBLG-C108 and MBLG-C114 with their side mesityl groups rotated to 10° are shown in Figures 4.26, 4.28, and 4.30 for configurations described in Figure 4.16. These results indicate that the transmission probability at Fermi energy E_F varies between10^{-6} G_0 and 10^{-4} G_0, which is higher than the result mentioned above in sections (4.8.1) and (4.8.2).

4.8.4 Transmission function calculations of MSLG for case (d)

In this section, cross-plane junctions of MSLG-C96 with the side groups rotated to 40°, 35°, 30°, and 20° were constructed using the distances shown in Table 4.5. The transmission functions were then calculated, as shown in Figure 4.31. As shown in

Figure 4.31 (b), MSLG-C96 exhibits a greater transmission spectrum at Fermi energy E_F as the angle of the side mesityl groups decreases from 40° to 20°.

It is also found that a side group angle of 40° relative to the plane of MSLG-C96 gives the closest agreement with the experimental conductance (see the horizontal black dotted line in Figure 4.31 (b) which represents the experimental value of the conductance of molecular junctions for MSLG-C96).

Furthermore, a variety of configurations described in Figure 4.15 and Figure 4.16 between the graphene sheets and the MSLG-C96 with side groups rotated to 40° are studied. Figures 4.32 and 4.33 show the nine-transmission spectrum of MSLG-C96 with side groups rotated to 40°corresponds to nine different configurations described in Figures 4.15 and 4.16.

The results show that the transmission spectrum of MSLG-C96 at Fermi energyE_F when the side groups are rotated to 40° varies between 10^{-5} G_0 and 10^{-4} G_0. As shown in the section (4.8), charge transport through molecular junctions of MBLGs and MSLG-C96 is sensitive to the angle between the graphene flake and peripheral mesityl groups and the rotation angles of the mesityl groups could tune the charge transport between the two graphene sheets.

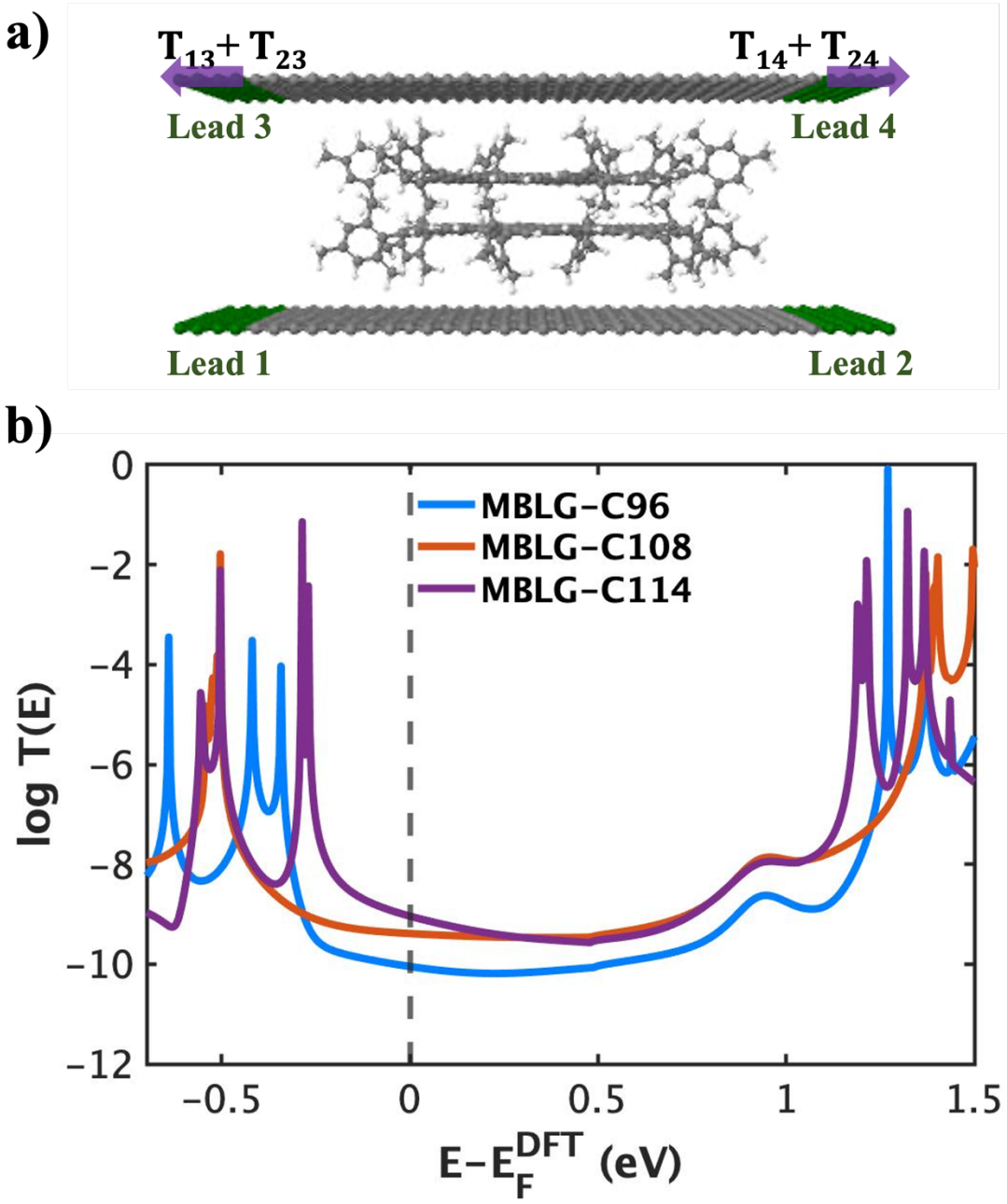

Figure 4.18. Transport properties of MBLG molecules in which the peripheral mesityl groups are close to 90°. (a) Sandwiched structure of the molecular junction of MBLG-C114. (b) Transmission spectra of MBLG-C96, MBLG-C108, and MBLG-C114 (The black dotted line represents Fermi energyE_F, estimated by density functional theory (DFT) and the transmission function curves represent the summation of T_{13}+T_{14}+T_{23}+T_{24}.

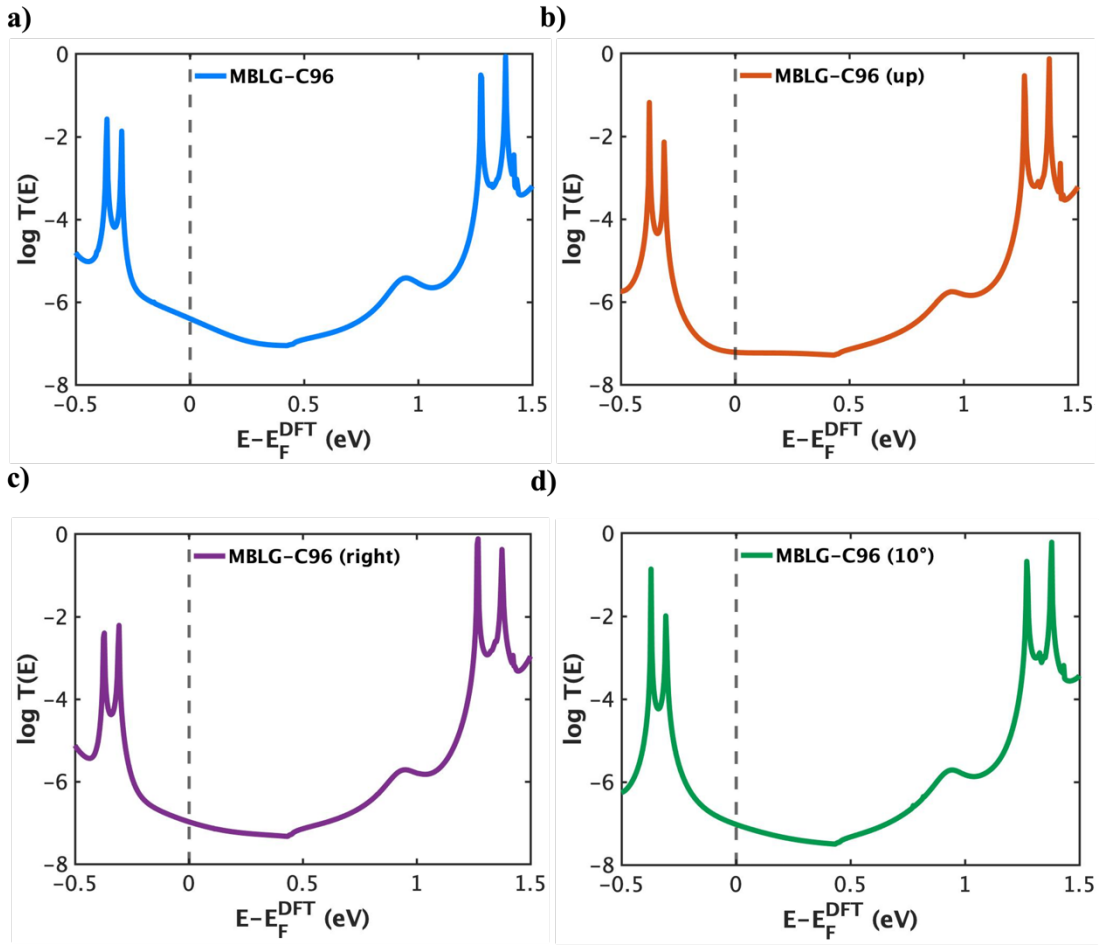

Figure 4.19. Transmission spectra of the different configurations (described in Figure 4.15) of MBLG-C96 as rotating the side groups to 30° relative to the graphene flake (The black dotted line represents Fermi energyE_F, estimated by density functional theory (DFT).

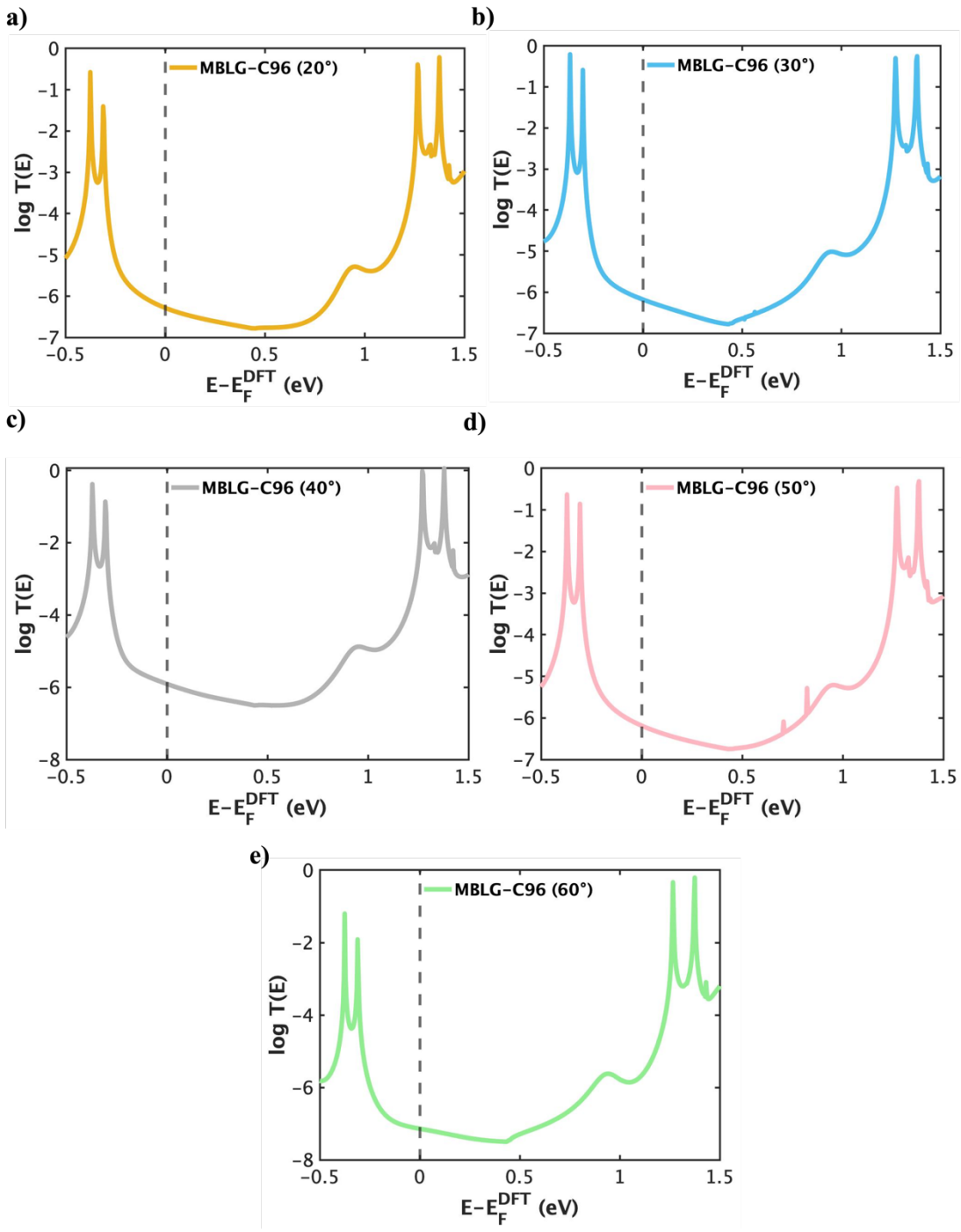

Figure 4.20. Transmission spectra of the different configurations (described in Figure 4.16) of MBLG-C96 as rotating the side groups to 30° relative to the graphene flake (The black dotted line represents Fermi energyE_F, estimated by density functional theory (DFT).

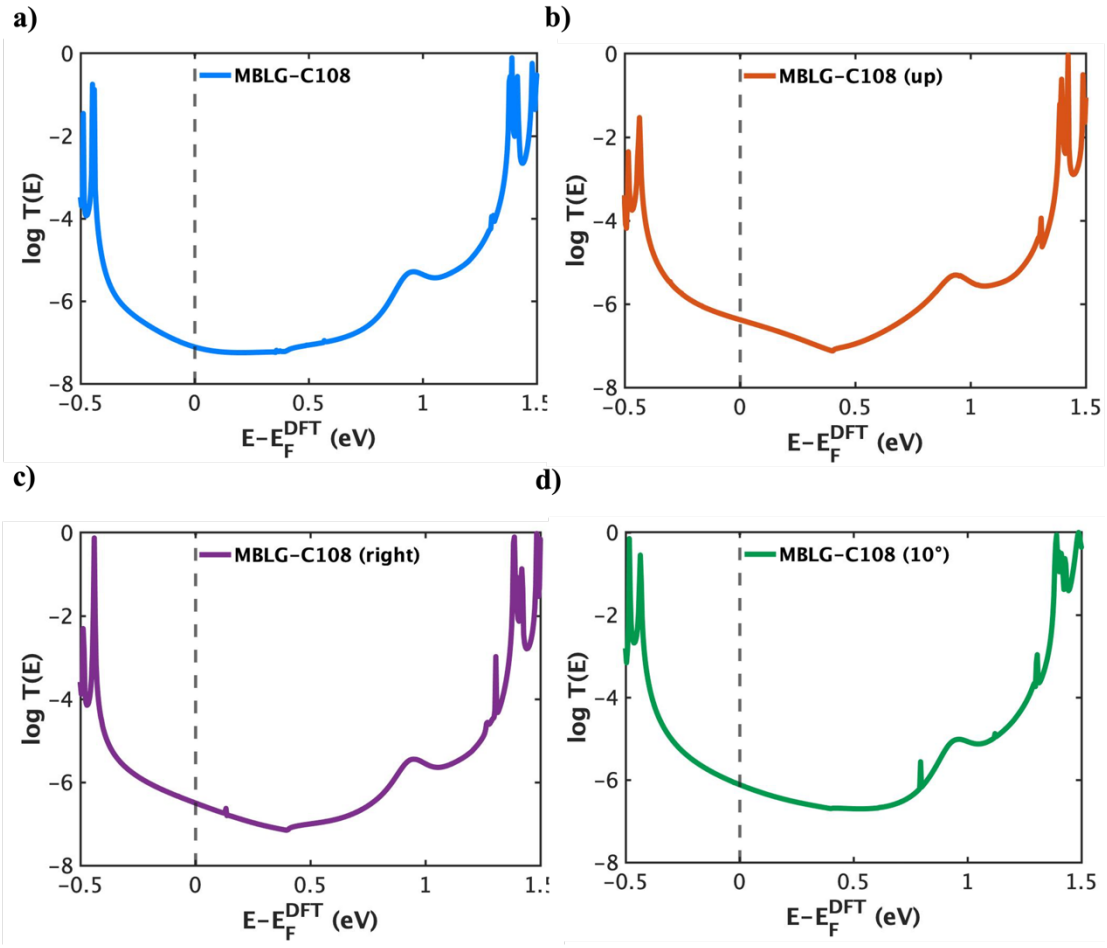

Figure 4.21. Transmission spectra of the different configurations (described in Figure 4.15) of MBLG-C108 as rotating the side groups to 30° relative to the graphene flake (The black dotted line represents Fermi energyE_F, estimated by density functional theory (DFT).

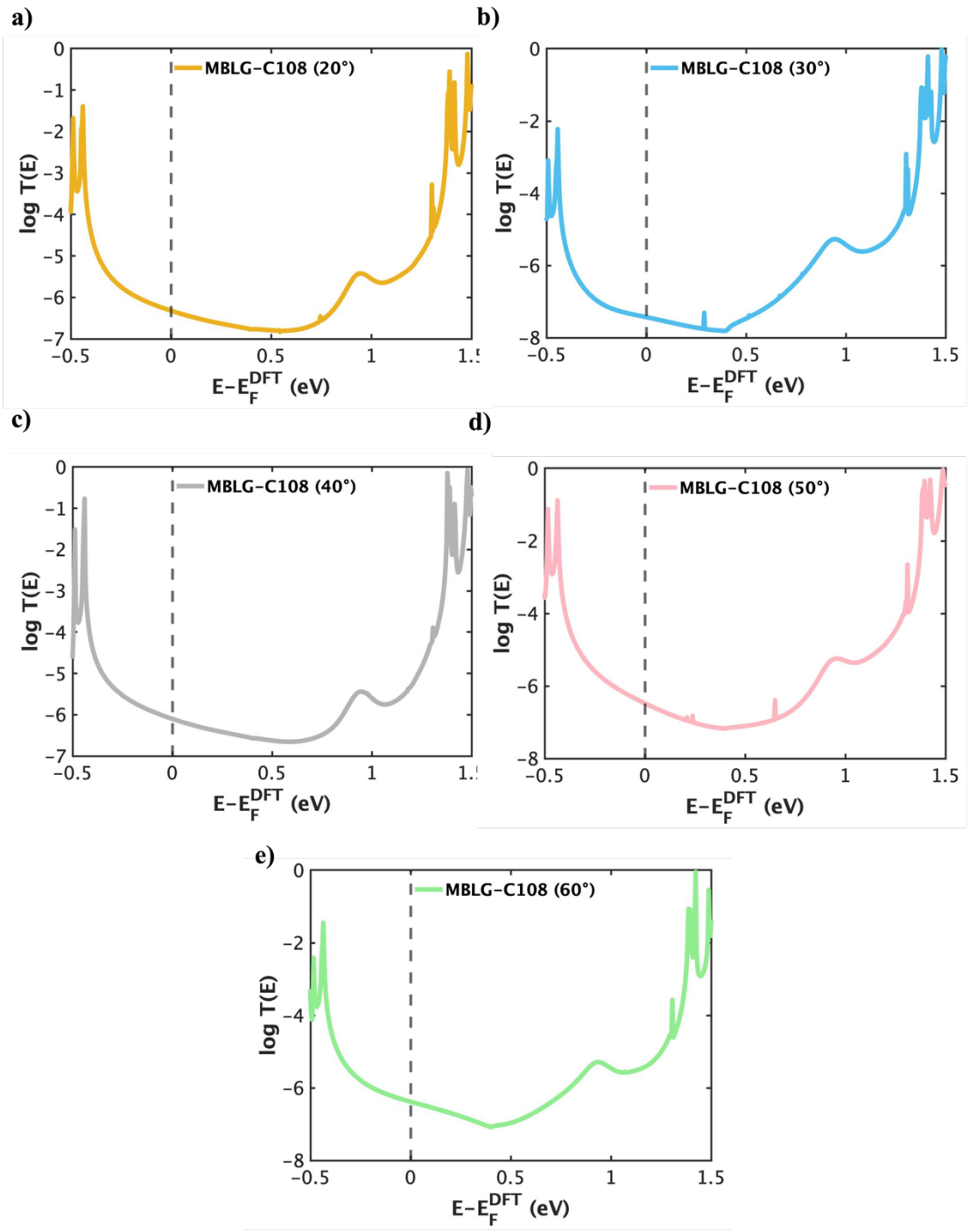

Figure 4.22. Transmission spectra of the different configurations (described in Figure 4.16) of MBLG-C108 as rotating the side groups to 30° relative to the graphene flake (The black dotted line represents Fermi energyE_F, estimated by density functional theory (DFT).

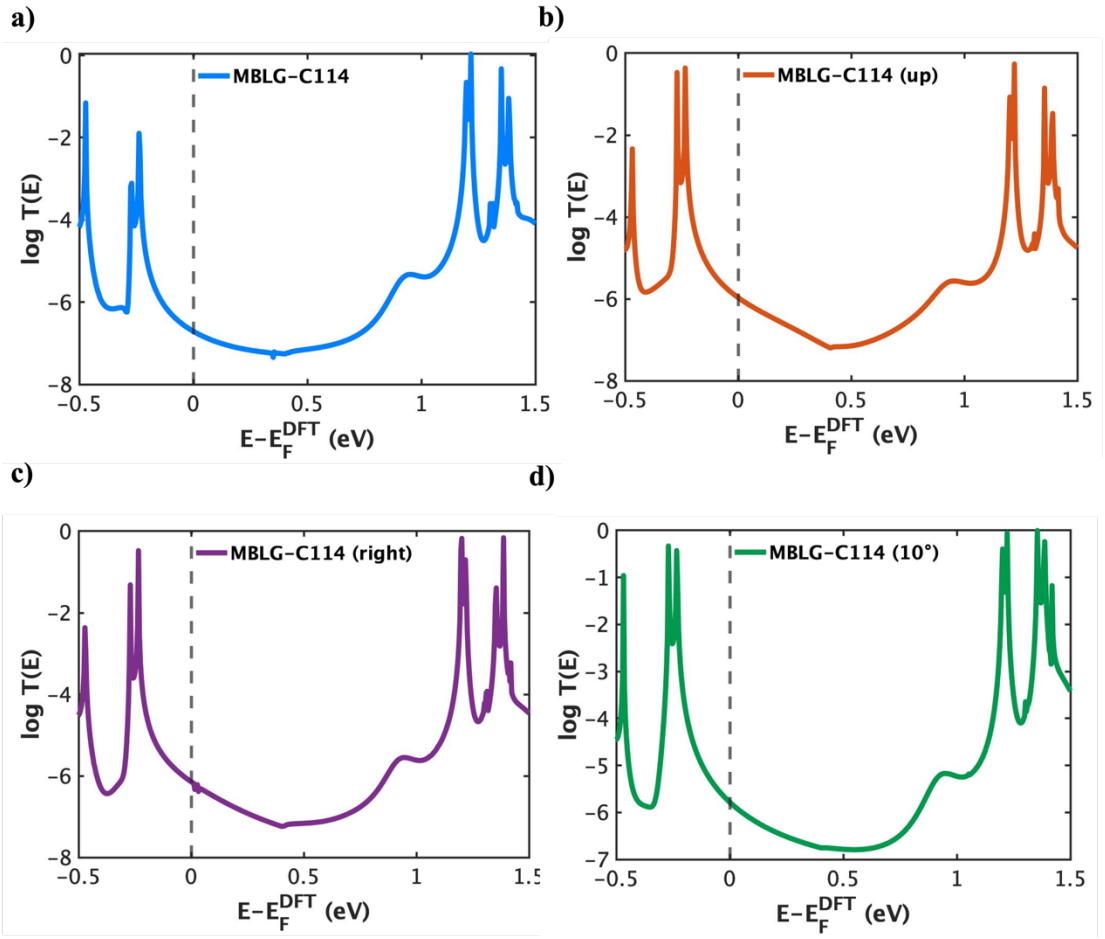

Figure 4.23. Transmission spectra of the different configurations (described in Figure 4.15) of MBLG-C114 as rotating the side groups to 30° relative to the graphene flake (The black dotted line represents Fermi energyE_F, estimated by density functional theory (DFT).

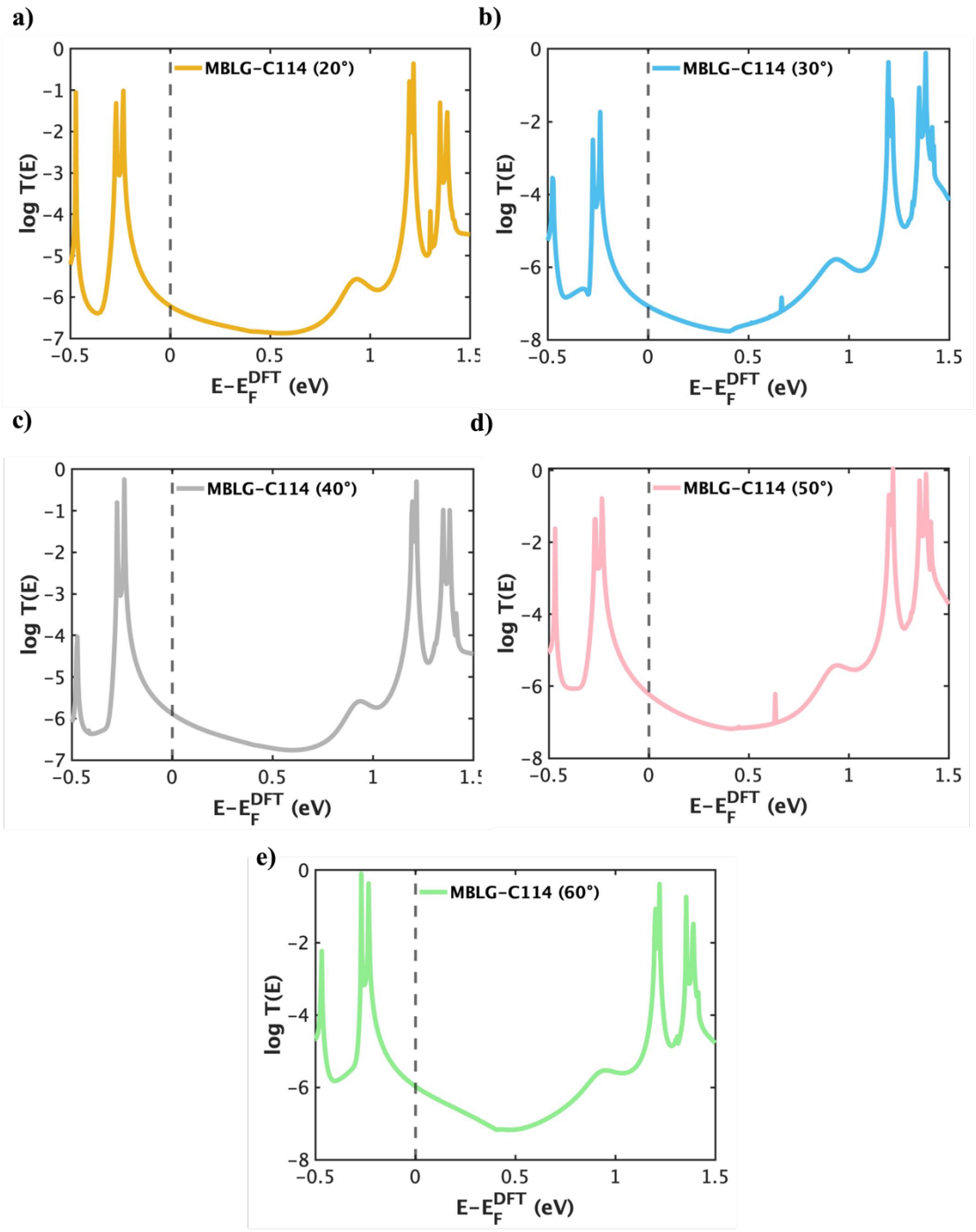

Figure 4.24. Transmission spectra of the different configurations (described in Figure 4.16) of MBLG-C114 as rotating the side groups to 30° relative to the graphene flake (The black dotted line represents Fermi energyE_F, estimated by density functional theory (DFT).

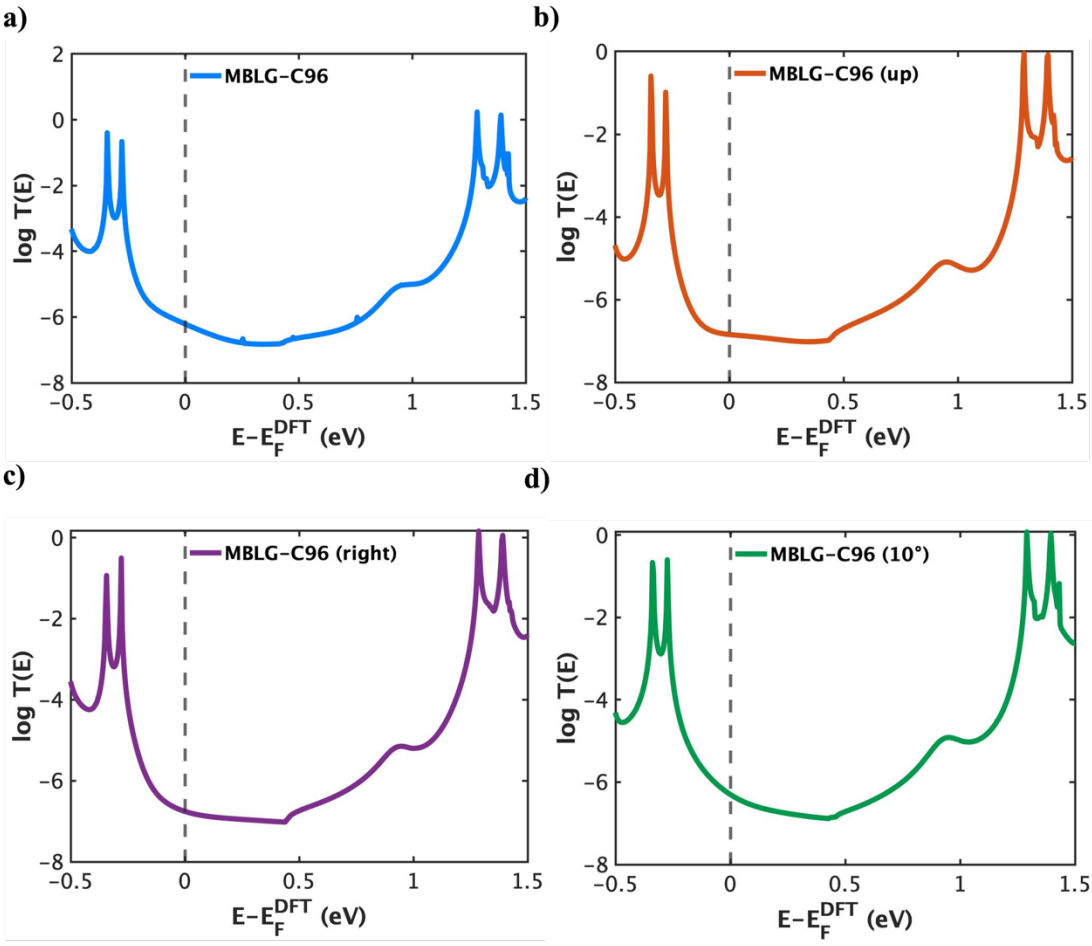

Figure 4.25. Transmission spectra of the different configurations (described in Figure 4.15) of MBLG-C96 as rotating the side groups to 10° relative to the graphene flake (The black dotted line represents Fermi energyE_F, estimated by density functional theory (DFT).

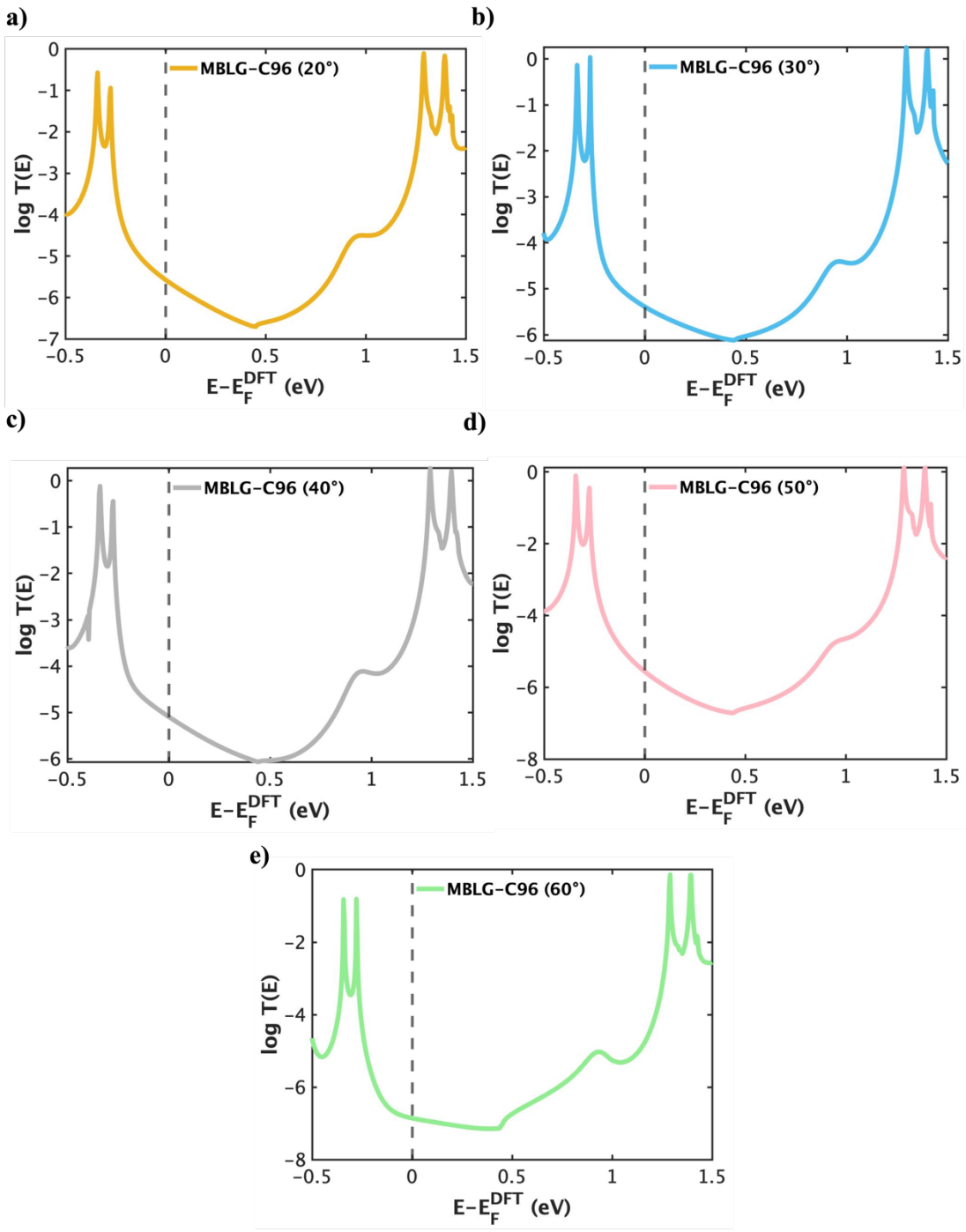

Figure 4.26. Transmission spectra of the different configurations (described in Figure 4.16) of MBLG-C96 as rotating the side groups to 10° relative to the graphene flake (The black dotted line represents Fermi energyE_F, estimated by density functional theory (DFT).

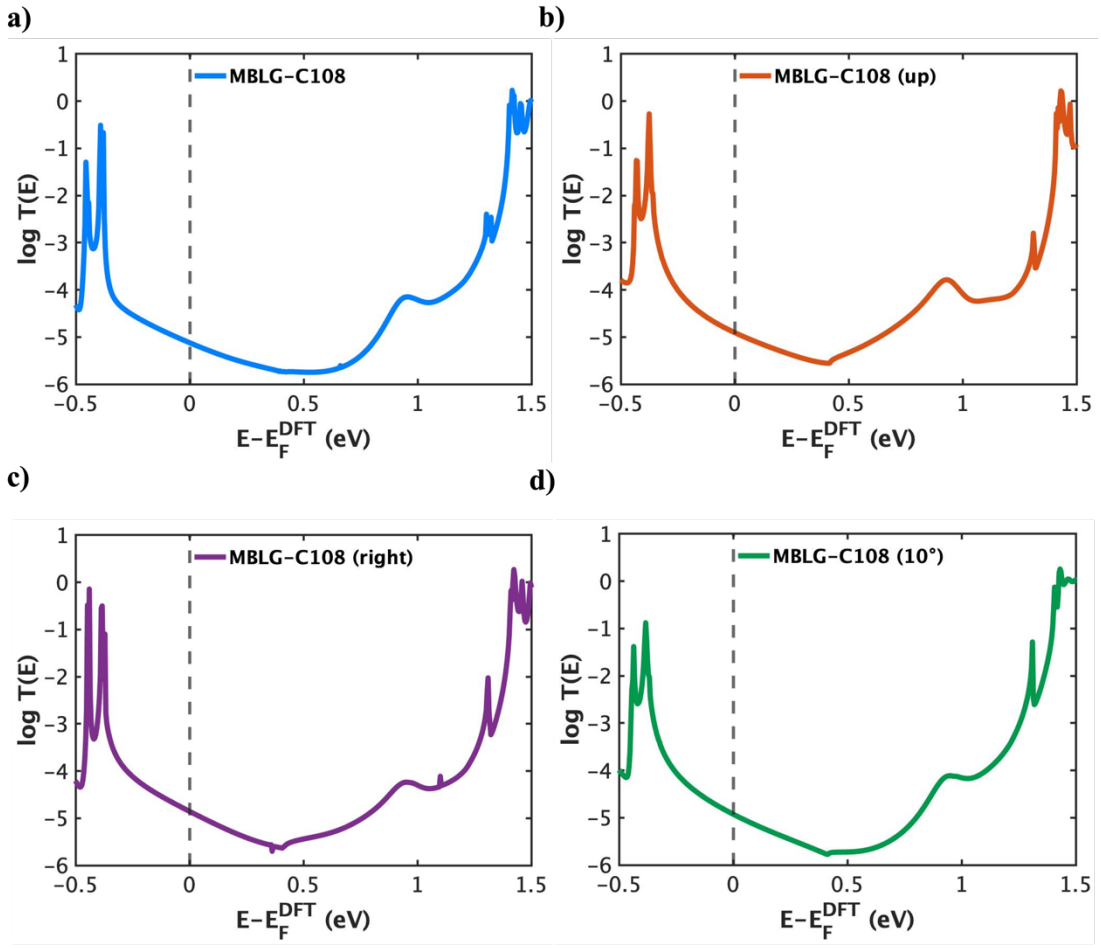

Figure 4.27. Transmission spectra of the different configurations (described in Figure 4.15) of MBLG-C108 as rotating the side groups to 10° relative to the graphene flake (The black dotted line represents Fermi energyE_F, estimated by density functional theory (DFT).

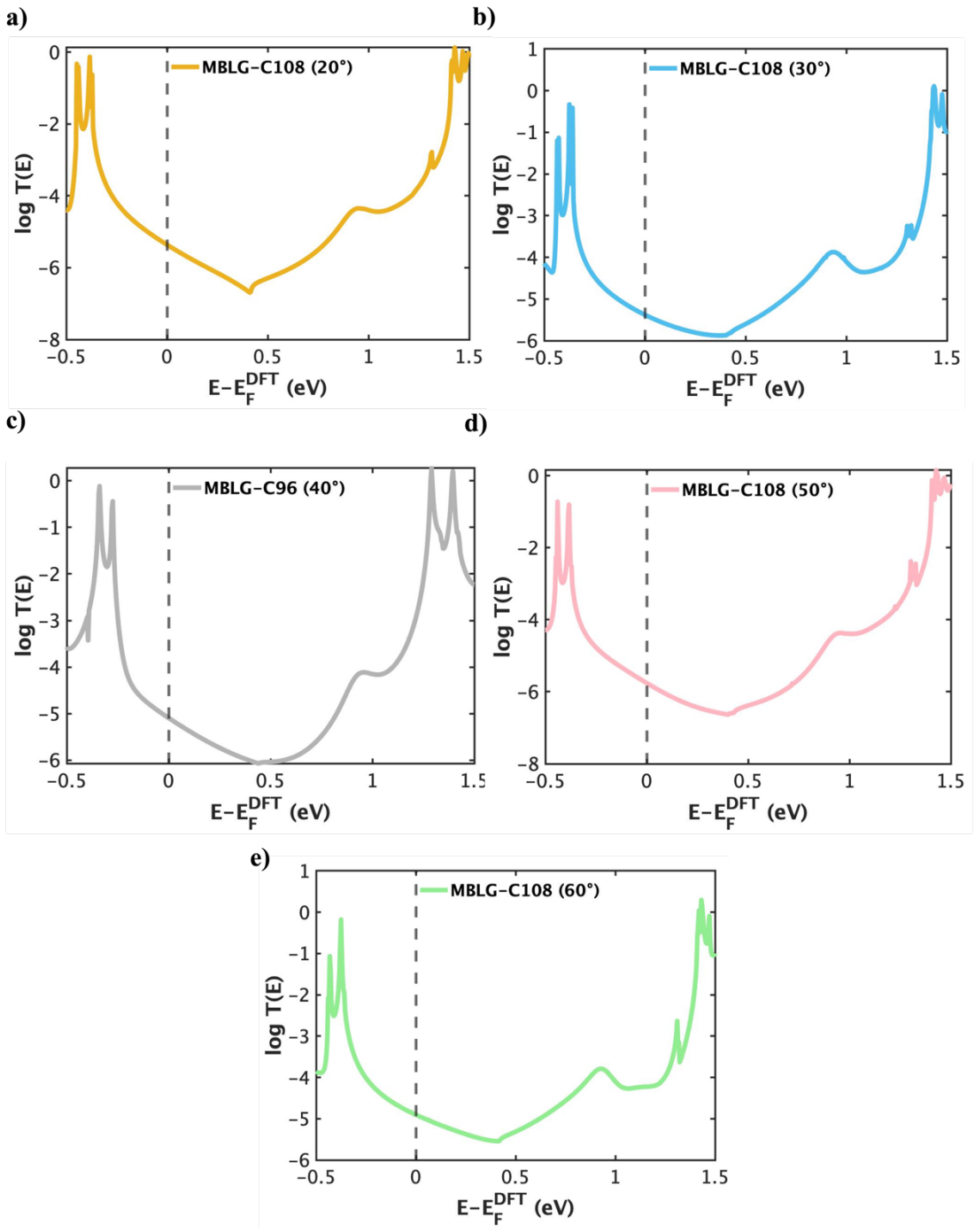

Figure 4.28. Transmission spectra of the different configurations (described in Figure 4.16) of MBLG-C108 as rotating the side groups to 10° relative to the graphene flake (The black dotted line represents Fermi energyE_F, estimated by density functional theory (DFT).

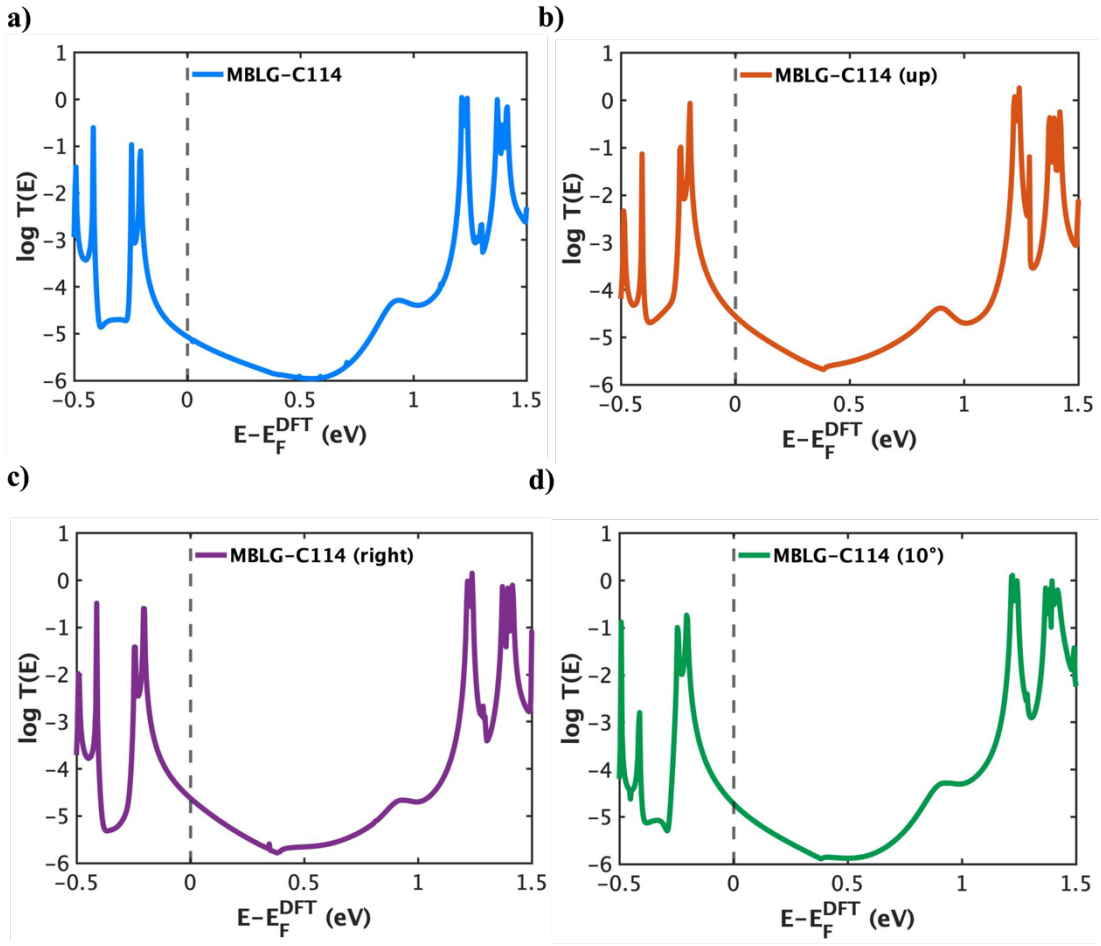

Figure 4.29. Transmission spectra of the different configurations (described in Figure 4.15) of MBLG-C114 as rotating the side groups to 10° relative to the graphene flake (The black dotted line represents Fermi energyE_F, estimated by density functional theory (DFT).

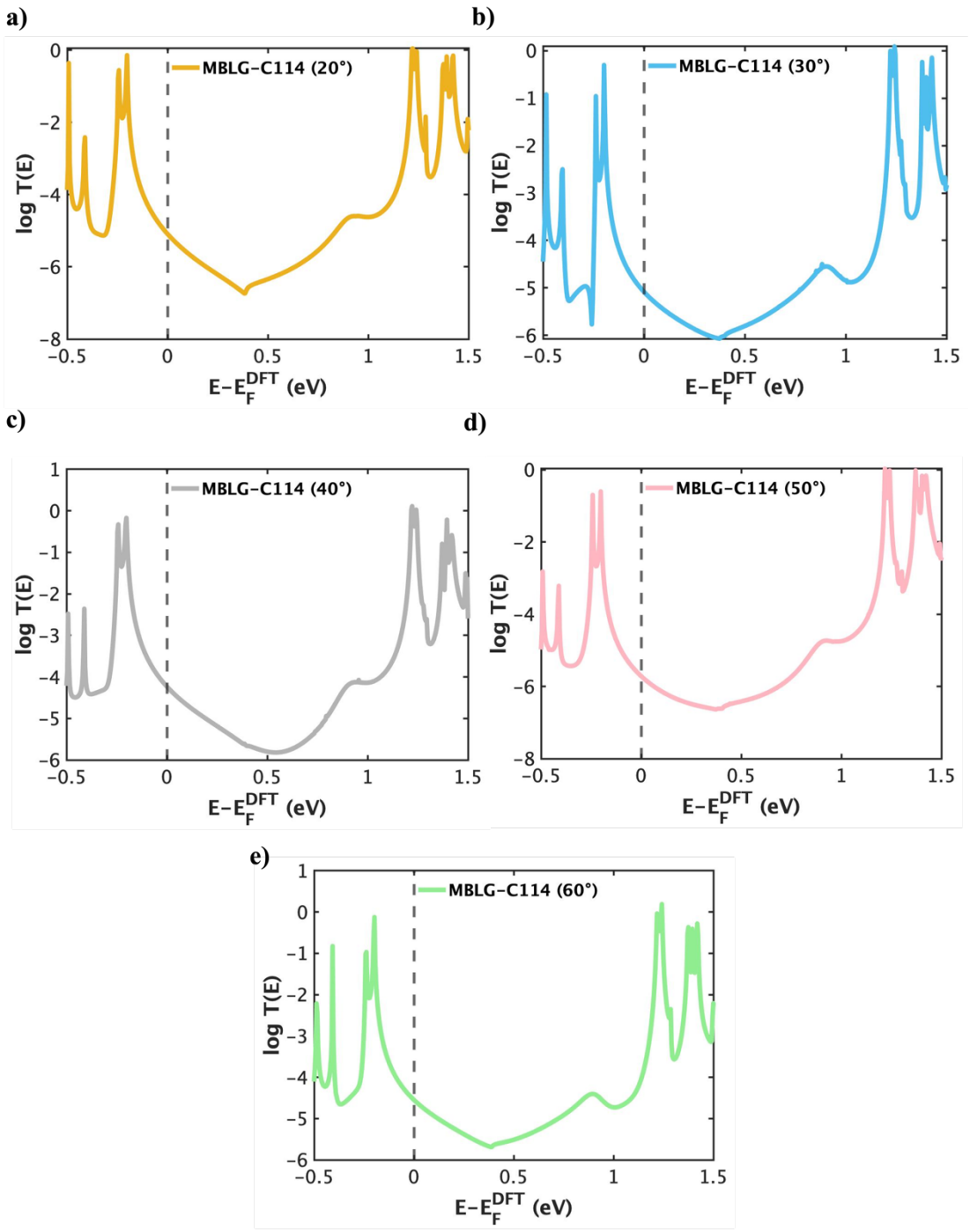

Figure 4.30. Transmission spectra of the different configurations (described in Figure 4.16) of MBLG-C114 as rotating the side groups to 10° relative to the graphene flake (The black dotted line represents Fermi energyE_F, estimated by density functional theory (DFT).

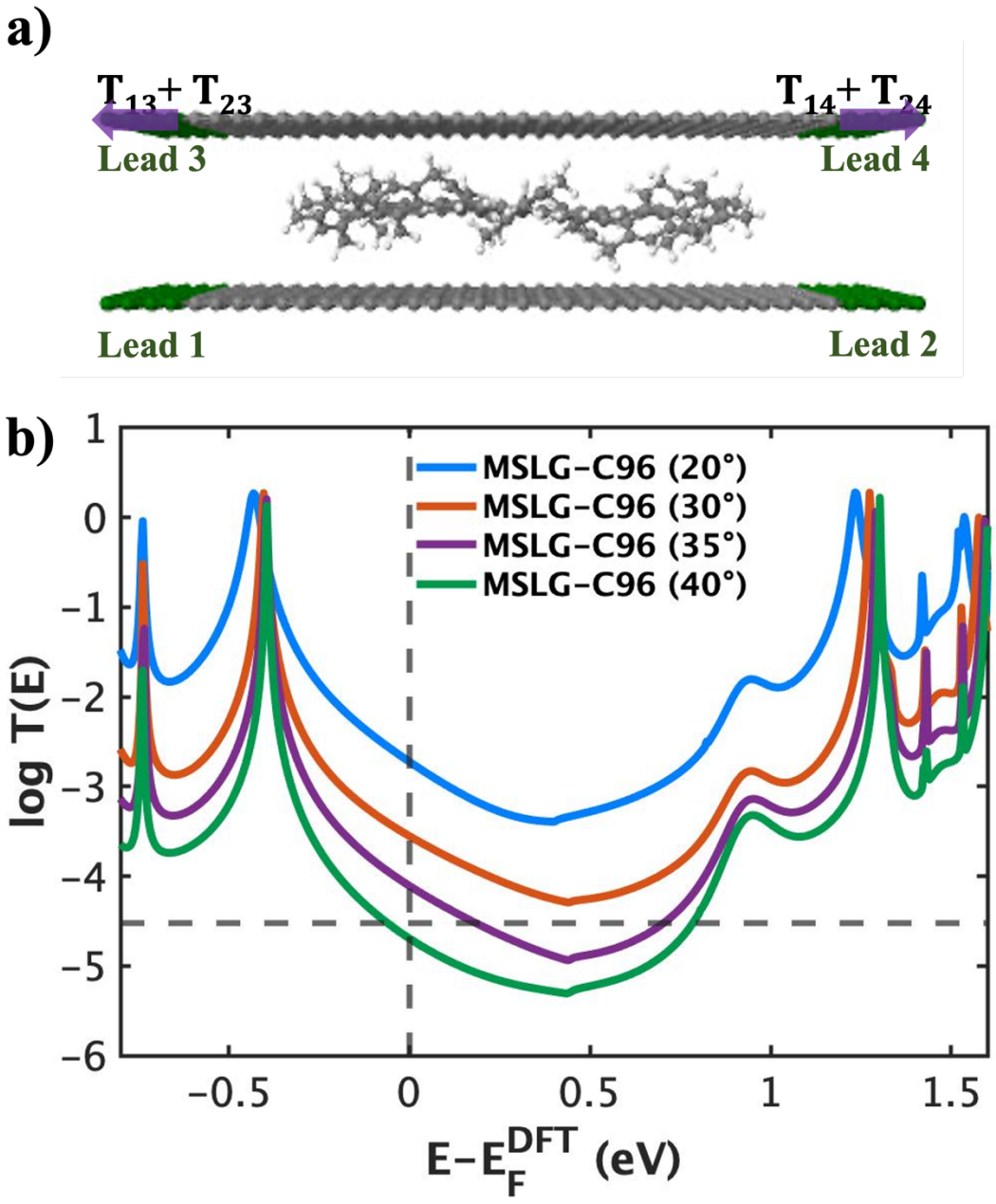

Figure 4.31. (a) Sandwiched structure of the molecular junction of MSLG-C96. (b) Transmission spectra of geometries with varying angles of rotation in which the transmission function curves represent the summation of T_{13}+T_{14}+T_{23}+T_{24} (the horizontal black dotted line represents the experimental value of the conductance of molecular junctions for MSLG-C96 as shown in Figure 4.35 (b)).

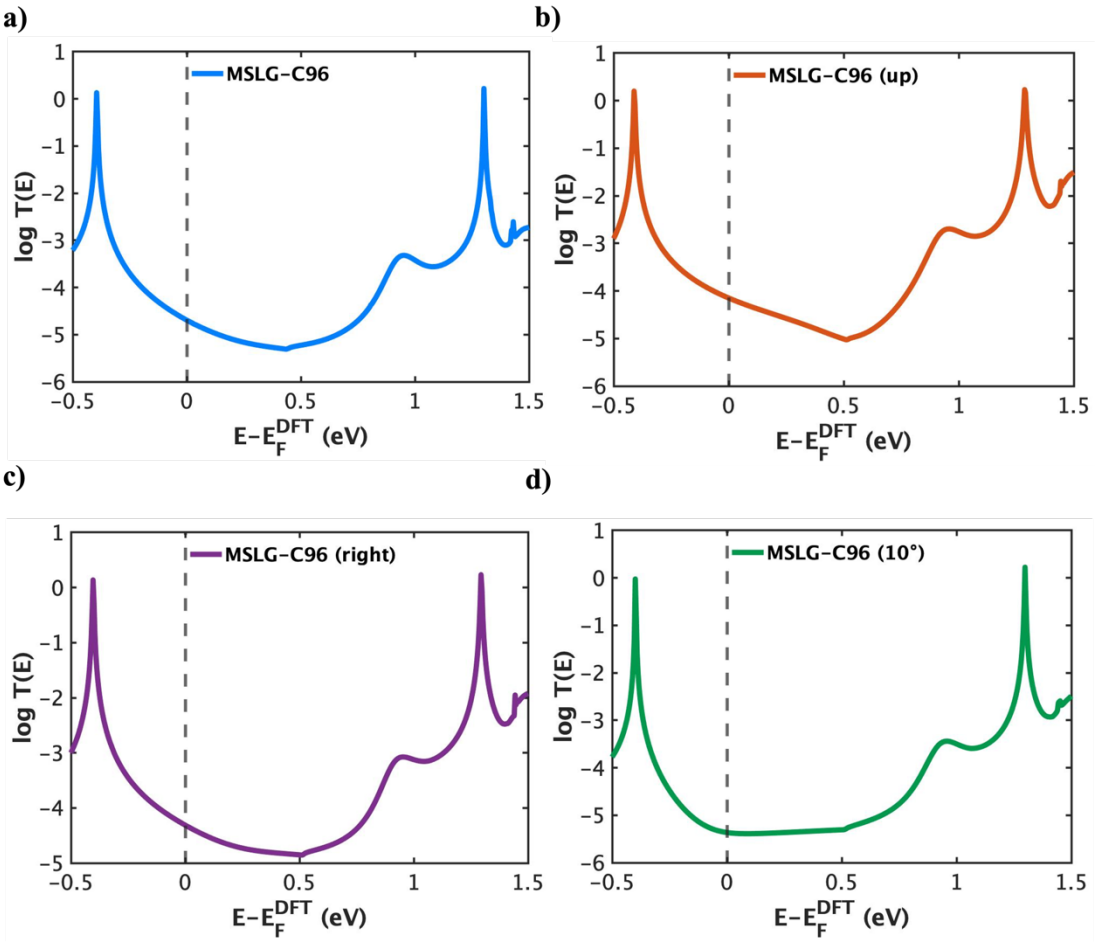

Figure 4.32. Transmission spectra of several configurations (described in Figure 4.15) of MSLG of C96 with side groups rotated to 40° (The black dotted line represents Fermi energyE_F, estimated by density functional theory (DFT).

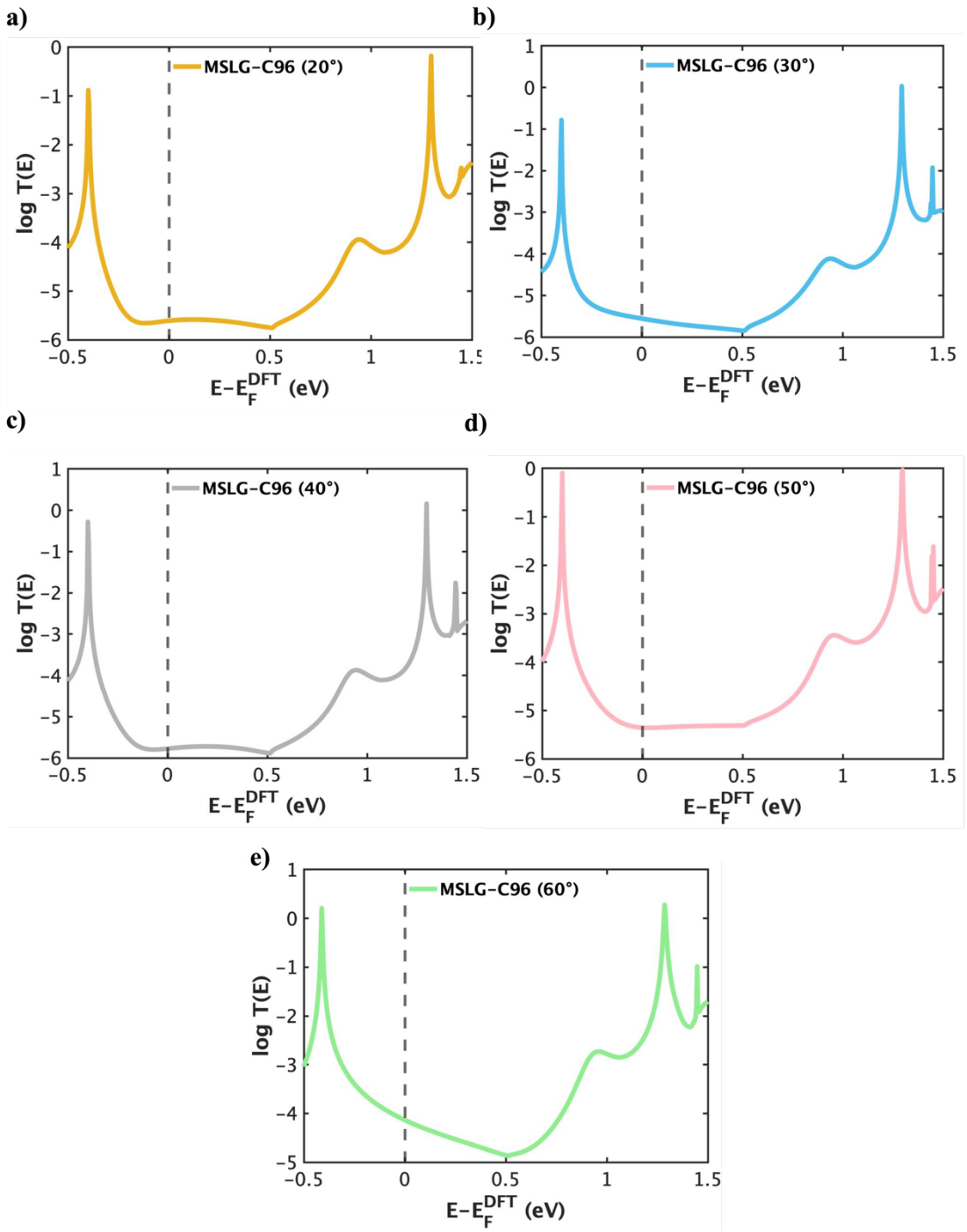

Figure 4.33. Transmission spectra of several configurations (described in Figure 4.16) of MSLG of C96 with side groups rotated to 40° (The black dotted line represents Fermi energyE_F, estimated by density functional theory (DFT).

4.9 The average of the transmission functions of MBLG and MSLG molecules

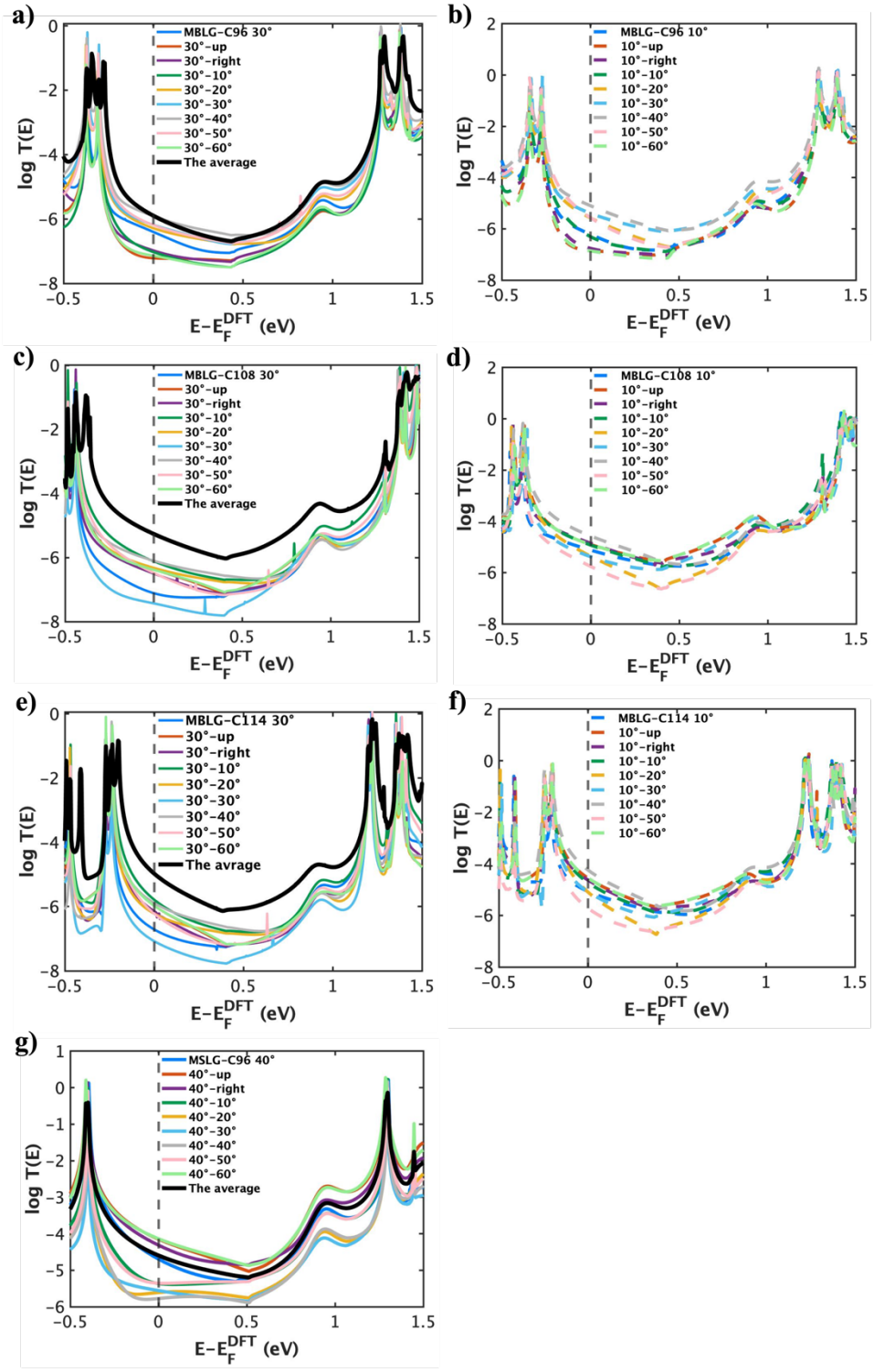

Figure 4.34. The average of the transmission spectra of the different geometries of, (a)MBLG-C96 as rotating the side groups to 30° relative to the graphene flake (solid curves). (b) MBLG-C96 as rotating the side groups to 10° relative to the graphene flake (dotted curves). (c) MBLG-C108 as rotating the side groups to 30° relative to the graphene flake (solid curves). (d) MBLG-C108 as rotating the side groups to 10° relative to the graphene flake (dotted curves). (e) MBLG-C114 as rotating the side groups to 30° relative to the graphene flake (solid curves). (f) MBLG-C114 as rotating the side groups to 10° relative to the graphene flake (dotted curves). And (g) MSLG-C96 as rotating the side groups to 40° relative to the graphene flake (solid curves) and the average of all 18 transmission curves (black solid curve).

In this section, the average transmission functions of MBLG-C96, MBLG-C108, and MBLG-C114 with side groups rotated to 30° and 10°**,** and MSLG-C96 with side groups rotated to 40° are calculated. In Figure 4.34, I grouped the transmission spectra of several configurations of MBLG-C96 with side groups rotated to 30° (a) and 10° (b), the solid-coloured curves are collected from Figures (4.19 and 4.20) and the dotted coloured curves collected from Figures (4.25 and 4.26). The black solid curves present the average of all 18 transmission curves of MBLG-C96.

Similarly, for MBLG-C108 and MBLG-C114, the solid-coloured curves are collected from Figures (4.21 and 4.22, 4.23 and 4.24) and the dotted-coloured curves from Figures (4.27 and 4.28, 4.29 and 4.30) and the black solid curves, presents the average of all 18 transmission curves of MBLG-C108 and MBLG-C114. Figure 4.34 shows that the higher transmission functions of 10° geometries make the majority of contributions

to the average ones. Also, Figure 4.34 (g) shows transmission curves of several configurations of MSLG-C96 with side groups rotated to 40° relative to the graphene flake (collected from Figures 4.32 and 33) and the black solid curve presents the average of all nine transmission curves of MSLG.

4.10 Comparison of DFT results with experimental results

To discuss DFT results and compare them with experimental results, Figure 4.35 presents (a) the averages of MBLG-C114, MBLG-C108, MBLG-C96, and MSLG-C96 separately, and (b-c) show the experimental results (The Figures are taken from [26])

In Figure 4.35 (a), the DFT results indicate that MBLG-C114, which has the largest molecular area, has the highest transmission function, compared to the smaller molecules MBLG-C108 and MBLG-C96. It is shown in Figure 4.28 b, that the DFT results are in agreement with experimental data, in which the molecular junction of MBLG-C114 exhibits the highest measured conductance, and MBLG-C96 exhibits the lowest.

Also, DFT results presented in Figure 4.35 (a) demonstrate that MSLG-C96 (green colour) has a greater transmission spectrum than MBLG molecules, which is also consistent with experimental results (Figure 4.28 c).

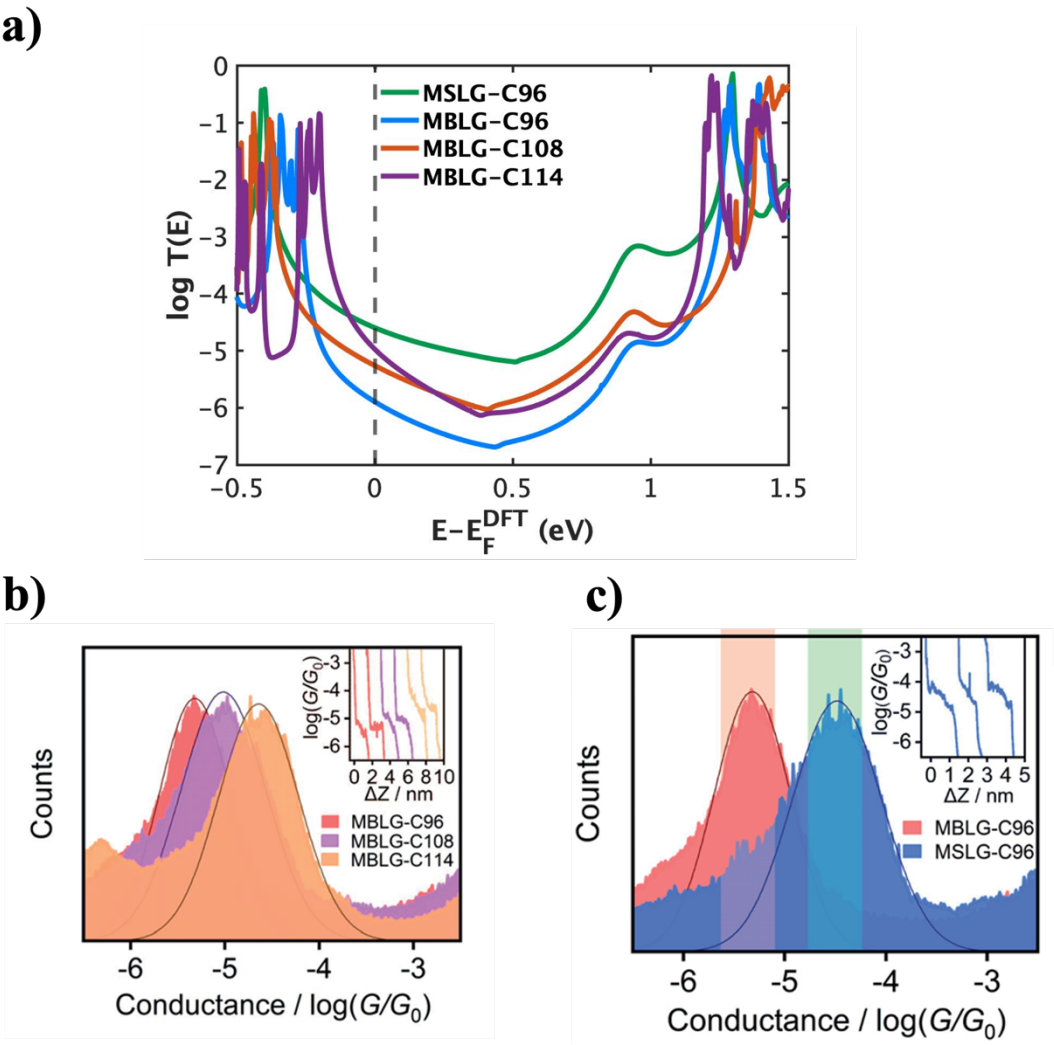

Figure 4.35. Comparison of DFT results with experimental results (a) The average transmission function of MBLG-C96 (blue curve), MBLG-C108 (orange curve), MBLG-C114 (purple curve), and MSLG-C96 (green curve) as a function of the Fermi energyE_F, estimated by density functional theory (DFT). (b) 1D conductance histograms of MBLG-C96, MBLG-C108, and MBLG-C114. (c) Comparison of 1D conductance histograms of the single-molecule junctions for MBLG-C96 and MSLG-C96 with Gaussian fitting.

4.11 Theoretical simulations for MSLG-C96 with side groups that rotated to 30° and without it.

It is also interesting to note that the mesityl groups can also mediate electron transport. Figure 4.26 presents theoretical simulations of MSLG-C96 with its side groups rotated to 30°(blue curve), as well as MSLG-C96 with its side groups manually cut (orange curve). It is shown that by artificially removing the mesityl groups, whilst maintaining the spacing between the graphene electrodes, the electrical conductance is reduced.

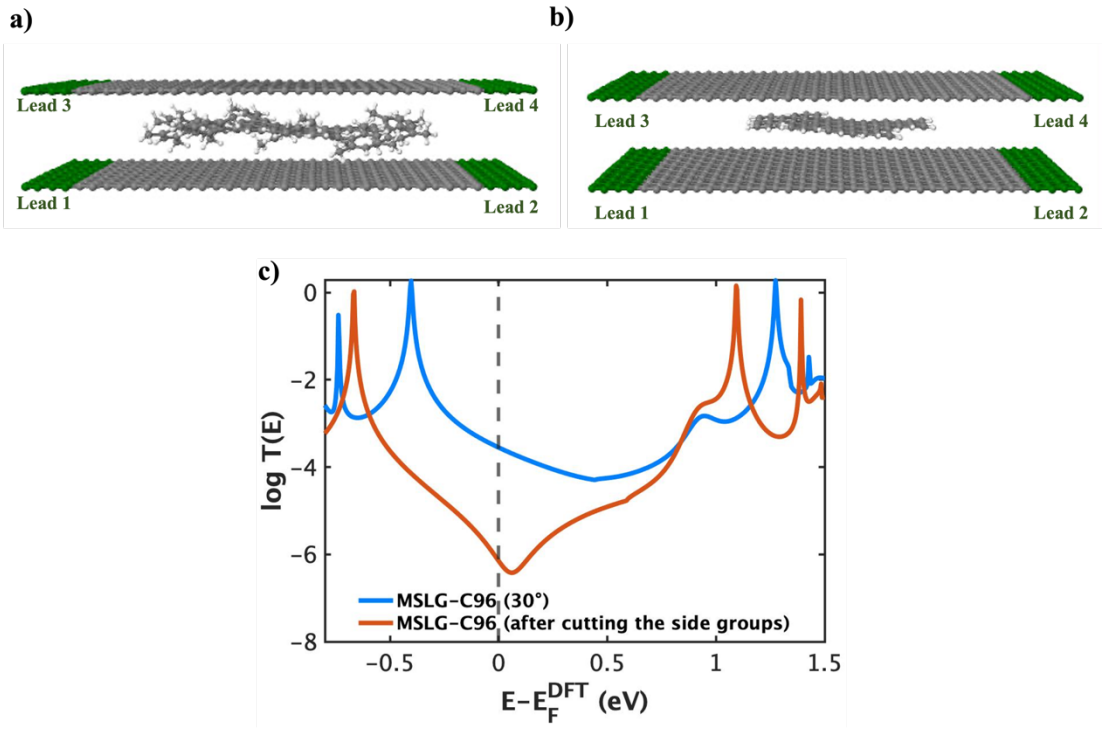

Figure 4.36. Theoretical simulations for MSLG-C96 with side groups that rotated to 30° and without it. (a) The sandwiched structure for MSLG-C96 with side groups rotated to 30°. (b) The sandwiched structure for MSLG-C96 after manually cutting the side groups. (c) DFT-based transmission functions for MSLG-C96 with side groups (blue curve) and MSLG-C96 after cutting the side

groups (orange curve) (The black dotted line represents Fermi energyE_F, estimated by density functional theory (DFT).

4.12 Conclusion

In this work, I investigated charge transport through molecular bilayer graphene (MBLG) junctions with graphene electrodes using ab initio density functional theory (DFT). The DFT results show that the electrical conductance of molecular junctions based on MBLG-C114 is larger than those of the smaller molecules MBLG-C96 and MBLG-C108, suggesting that the size of MBLG could be used to tune charge transport through vdW heterojunctions. Also, it was found that the molecular junctions based on MSLG-C96 are more conductive than MBLG-C96.

Furthermore, DFT calculations demonstrate that the angle between the core of molecular graphene and peripheral mesityl groups has a significant effect on the charge transport through single-molecule graphene junctions, and the flattening of the mesityl groups leads to higher electrical conductance.

4.13 Bibliography

[1] Novoselov KS, Fal'ko VI, Colombo L, Gellert PR, Schwab MG, Kim K. A roadmap for graphene. Nature 2012; 490:192-200.

[2] Tan C, Cao X, Wu XJ, He Q, Yang J, Zhang X, Chen J, Zhao W, Han S, Nam GH, Sindoro M, Zhang H. Recent Advances in Ultrathin Two-Dimensional Nanomaterials. Chem Rev 2017; 117:6225-6331.

[3] Fan FR, Wang R, Zhang H, Wu W. Emerging beyond-graphene elemental 2D materials for energy and catalysis applications. Chem Soc Rev 2021; 50:10983-11031.

[4] Cao Y, Fatemi V, Fang S, Watanabe K, Taniguchi T, Kaxiras E, Jarillo-Herrero P. Unconventional superconductivity in magic-angle graphene superlattices. Nature 2018.

[5] Matthew Yankowitz, Shaowen Chen, Hryhoriy Polshyn, Yuxuan Zhang, K. Watanabe, T. Taniguchi, David Graf, Andrea F. Young, Dean. CR. Tuning superconductivity in twisted bilayer graphene. Science 2019.

[6] Jeroen B. Oostinga HBH, Xinglan Liu, Alberto F. Morpurgo and Lieven M. K. V andersypen. Gate-induced insulating state in bilayer graphene devices. 2008.

[7] Cao Y, Fatemi V, Demir A, Fang S, Tomarken SL, Luo JY, Sanchez-Yamagishi JD, Watanabe K, Taniguchi T, Kaxiras E, Ashoori RC, Jarillo-Herrero P. Correlated insulator behaviour at half-filling in magic-angle graphene superlattices. Nature 2018.

[8] Jin C, Regan EC, Yan A, Iqbal Bakti Utama M, Wang D, Zhao S, Qin Y, Yang S, Zheng Z, Shi S, Watanabe K, Taniguchi T, Tongay S, Zettl A, Wang F. Observation of moire excitons in WSe2/WS2 heterostructure superlattices. Nature 2019; 567:76-80.

[9] Li J, Yang X, Liu Y, Huang B, Wu R, Zhang Z, Zhao B, Ma H, Dang W, Wei Z, Wang K, Lin Z, Yan X, Sun M, Li B, Pan X, Luo J, Zhang G, Liu Y, Huang Y, Duan X, Duan X. General synthesis of two-dimensional van der Waals heterostructure arrays. Nature 2020; 579:368-374.

[10] Tran K, Moody G, Wu F, Lu X, Choi J, Kim K, Rai A, Sanchez DA, Quan J, Singh A, Embley J, Zepeda A, Campbell M, Autry T, Taniguchi T, Watanabe K, Lu N, Banerjee SK, Silverman KL, Kim S, Tutuc E, Yang L, MacDonald AH, Li X. Evidence for moire excitons in van der Waals heterostructures. Nature 2019; 567:71-75.

[11] Wang Z, Rhodes DA, Watanabe K, Taniguchi T, Hone JC, Shan J, Mak KF. Evidence of high-temperature exciton condensation in two-dimensional atomic double layers. Nature 2019; 574:76-80.

[12] Zhou Y, Sung J, Brutschea E, Esterlis I, Wang Y, Scuri G, Gelly RJ, Heo H, Taniguchi T, Watanabe K, Zarand G, Lukin MD, Kim P, Demler E, Park H. Bilayer Wigner crystals in a transition metal dichalcogenide heterostructure. Nature 2021; 595:48-52.

[13] Zhu X, Lei S, Tsai SH, Zhang X, Liu J, Yin G, Tang M, Torres CM, Jr., Navabi A, Jin Z, Tsai SP, Qasem H, Wang Y, Vajtai R, Lake RK, Ajayan PM, Wang KL. A Study of Vertical Transport through Graphene toward Control of Quantum Tunneling. Nano Lett 2018; 18:682-688.

[14] Prins F, Barreiro A, Ruitenberg JW, Seldenthuis JS, Aliaga-Alcalde N, Vandersypen LM, van der Zant HS. Room-temperature gating of molecular junctions using few-layer graphene nanogap electrodes. Nano Lett 2011; 11:4607-4611.

[15] Aragones AC, Haworth NL, Darwish N, Ciampi S, Bloomfield NJ, Wallace GG, Diez-Perez I, Coote ML. Electrostatic catalysis of a Diels-Alder reaction. Nature 2016; 531:88-91.

[16] Xiang D, Jeong H, Lee T, Mayer D. Mechanically controllable break junctions for molecular electronics. Adv Mater 2013; 25:4845-4867.

[17] Kaneko S, Montes E, Suzuki S, Fujii S, Nishino T, Tsukagoshi K, Ikeda K, Kano H, Nakamura H, Vazquez H, Kiguchi M. Identifying the molecular adsorption site of a

single molecule junction through combined Raman and conductance studies. Chem Sci 2019; 10:6261-6269.

[18] Li H, Garner MH, Shangguan Z, Zheng Q, Su TA, Neupane M, Li P, Velian A, Steigerwald ML, Xiao S, Nuckolls C, Solomon GC, Venkataraman L. Conformations of cyclopentasilane stereoisomers control molecular junction conductance. Chem Sci 2016; 7:5657-5662.

[19] Naher M, Milan DC, Al-Owaedi OA, Planje IJ, Bock S, Hurtado-Gallego J, Bastante P, Abd Dawood ZM, Rincon-Garcia L, Rubio-Bollinger G, Higgins SJ, Agrait N, Lambert CJ, Nichols RJ, Low PJ. Molecular Structure-(Thermo)electric Property Relationships in Single-Molecule Junctions and Comparisons with Single- and Multiple-Parameter Models. J Am Chem Soc 2021; 143:3817-3829.

[20] Zhou J, Wang K, Xu B, Dubi Y. Photoconductace from Exciton Binding in Molecular Junctions. J Am Chem Soc 2018; 140:70-73.

[21] Zheng J, Liu J, Zhuo Y, Li R, Jin X, Yang Y, Chen ZB, Shi J, Xiao Z, Hong W, Tian ZQ. Electrical and SERS detection of disulfide-mediated dimerization in single-molecule benzene-1,4-dithiol junctions. Chemical Science 2018; 9:5033-5038.

[22] S. Zhao QW, J. Pi, J. Liu, J. Zheng, S. Hou, J. Wei, R. Li, H. Sadeghi, Y. Yang, J. Shi, Z. Chen, Z. Xiao, C. Lambert, W. Hong,. Cross-plane transport in a single-molecule two-dimensional van der Waals heterojunction. SCIENCE ADVANCES 2020.

[23] Zhao S, Chen H, Qian Q, Zhang H, Yang Y, Hong W. Non-covalent interaction-based molecular electronics with graphene electrodes. Nano Research 2021.

[24] Zhao XJ, Hou H, Fan XT, Wang Y, Liu YM, Tang C, Liu SH, Ding PP, Cheng J, Lin DH, Wang C, Yang Y, Tan YZ. Molecular bilayer graphene. NATURE COMMUNICATIONS 2019; 10:3057.

[25] Xin-Jing Zhao HH, Peng-Peng Ding, Ze-Ying Deng, Yang-Yang Ju, Shun-He Liu, Yu-Min Liu, Chun Tang, Liu-Bin Feng, Yuan-Zhi Tan†. Molecular defect-containing bilayer graphene exhibiting brightened luminescence. SCIENCE ADVANCES 2020.

[26] Zhao S, Deng ZY, Albalawi S, Wu Q, Chen L, Zhang H, Zhao XJ, Hou H, Hou S, Dong G, Yang Y, Shi J, Lambert CJ, Tan YZ, Hong W. Charge transport through single-molecule bilayer-graphene junctions with atomic thickness. Chemical Science 2022; 13:5854-5859.

[27] Jose´ M Soler EA, Julian D Gale, Alberto Garc´ıa, Javier Junquera, Pablo Ordejo´n and Daniel Sa´nchez-Portal. The SIESTA method for ab initio order-N materials simulation. JOURNAL OF PHYSICS: CONDENSED MATTER 2002.

[28] Van der Waals Density Functional for General Geometries. PHYSICAL REVIEW LETTERS 2004; 92.

[29] k. Berland PH. Exchange functional that tests the robustness of the plasmon description of the van der Waals density functional 2014.

[30] J Ferrer CJL, V M García-Suárez, D Zs Manrique, D Visontai, L Oroszlany, R Rodríguez-Ferradás, I Grace,, S W D Bailey KG, Hatef Sadeghi and L A Algharagholy. GOLLUM: a next-generation simulation tool for electron, thermal and spin transport. New Journal of Physics 2014.

Chapter 5.

5 Regulation of cross-plane transport by changing substituents and conjugation

In this project, my DFT calculations at Lancaster University formed part of a collaboration with experimentalists at Xiamen University in China.

In this work, the effect of substituents and conjugation of molecules on charge transport through single-molecule junctions (SMJs) are investigated utilizing density functional theory (DFT). I find that the conductance of pyrene increases after being substituted by both electron-withdrawing and electron-donating groups, unlike the in-plane transport in the single-molecule junctions. On the other hand, I also find that hydrogenation disrupts conjugation reduces conductance. This work provides an important reference value for the precise regulation of electron transport in graphene-based molecular junctions by changing the degree of conjugation and substituents of molecules.

This work will be published soon in the name of Aromaticity changes the single-molecule conductance of the graphene-based cross-plane junctions.

5.1 Introduction

In the past decades, the electrical properties of many molecular electronic devices have been investigated, such as molecular wires [1-3], molecular switches [4-6], molecular rectifiers [7, 8], and molecular transistors [9, 10].

On the electrical properties of molecular electronic devices, electrode materials and anchoring groups of molecules have vital influences [11]. Currently, the main electrode materials are metallic and carbon-based materials, like carbon nanotubes or graphene. Compared with metallic electrodes, the graphene electrode has a highly dispersive density of states around the Fermi energy [12], remarkable mechanical strength, and robust chemical stability. Besides, graphene electrodes can be coupled with molecules through covalent bonds [5, 13] or π-π stacking interactions [14-18] to be fabricated as graphene-based molecular junctions.

Based on the features of graphene, several fabrication approaches for single-molecule junctions have been developed such as electroburning [19, 20], dash-line lithography [21, 22], and break junction [18]. In comparison, the break junction technique can be utilized for reproducible conductance measurement by forming thousands of single-molecule junctions within a short time and the size of the nano-scale gaps could be tuned to adapt different lengths of molecules during the pulling process to form molecular junctions.

Recently, a novel cross-plane break junction (XPBJ) technique together with DFT has been utilized to construct graphene M-vdWHs with polycyclic aromatic hydrocarbons effectively [17]. It is proved that the charge transport of this model was significantly different from that of conventional in-plane transport.

In this study, two sets of molecules were examined using Density Functional Theory (DFT) to analyse the impact of electron-withdrawing and electron-donating groups on the backbone molecules by introducing different types of substituents in the cross-plane charge transport junctions. Additionally, the influence of conjugation on electron transport in cross-plane molecular junctions was investigated.

5.2 Studied molecules

A study of the electrical properties of two groups of molecules is presented in this Chapter to study the effect of substituents and conjugation of molecules on charge transport in cross-plane molecular junctions. Using group (1), I study the effects of introducing electron-withdrawing substituents (-Br) and electron-donating substituents ($-NH_2$) on electron transport, since the introduction of the substituents changes the energy distribution within the molecule. In Group (1), three molecules have been selected, 1,6-diaminopyrene (DAPyr), 1,6-dibromopyrene (DBPyr), with substituents at the 1 and 6 sites of Pyrene respectively as shown in Figure 5.1.

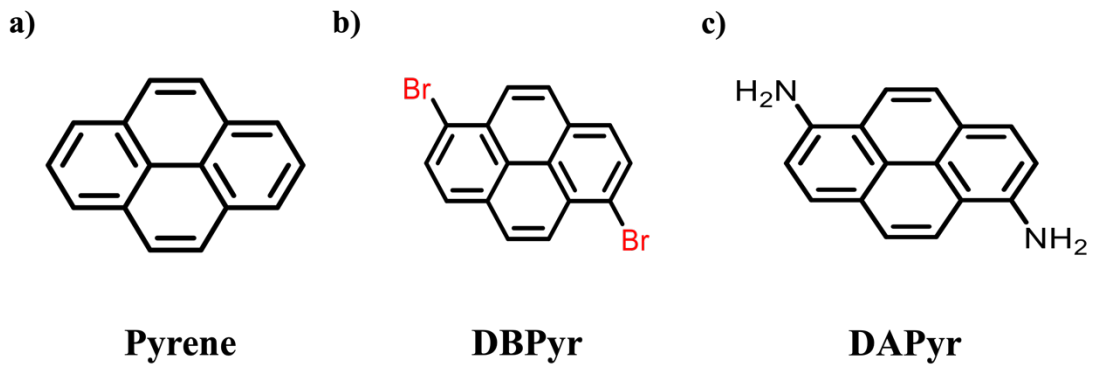

Figure 5.1. The chemical structures of the group (1) molecules: (a) Pyrene, (b) DBPyr and (c) DAPyr.

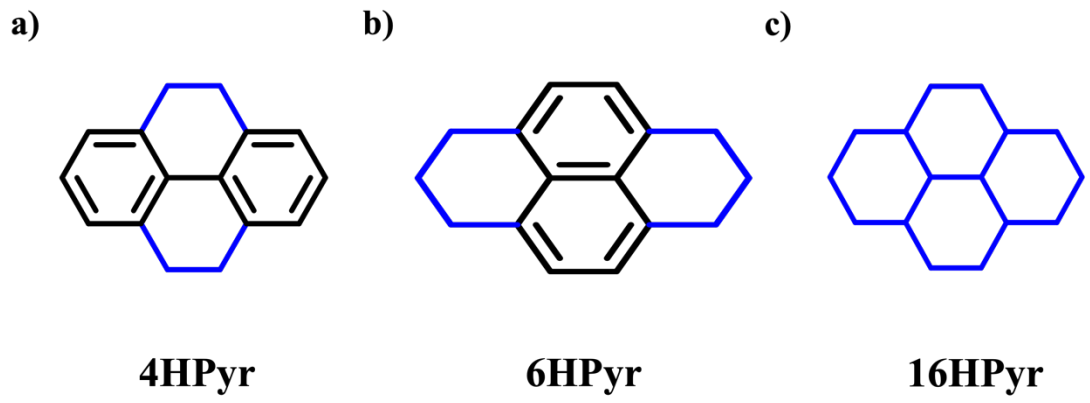

Figure 5.2. The chemical structures of the group (2): (a) 4HPyr, (b) 6HPyr and (c) 16HPyr.

In addition, group (2) includes the following molecular systems: hexahydropyrene (6HPyr), Tetrahydropyrene (4HPyr) and hexadecahydropyrene (16HPyr) as shown in Figure 5.2.

The number of aromatic rings decreases sequentially in the molecular structure, the aromatic rings are replaced by semi-saturated six-membered rings, and the planarity of the four molecules decreases sequentially. For the three-dimensional spatial structure of the four molecules, the molecule Pyrene is completely planar, while 16HPyr consists of fully saturated cyclohexane, which is the least planar. For 6HPyr the two aromatic rings are located in the middle of the molecule and can make the molecule as a whole closer to planarity, while for 4HPyr the two aromatic rings are located at the ends of the molecule and the planarity of the molecule as a whole is poor compared to 6HPyr. The order of the conjugation of the four molecules is pyrene, 6HPyr, 4HPyr and 16HPyr.

5.3 The geometry optimization

The geometrical optimization of the studied molecules (see Figure 5.1 and 5.2) is achieved using the density functional theory (DFT) code SIESTA [23]. The Van der Waals density functional (vdW-DF) [24], was used with a double-polarised atomic orbital basis set for carbon, bromine, nitrogen and hydrogen. The Mesh cut-off energy is set to 200 Rydberg. A relaxation process was applied to the molecules until the forces between the atoms reached 0.02 eV/ Å. Figures 5.3 and 5.4 show the fully relaxed isolated molecules.

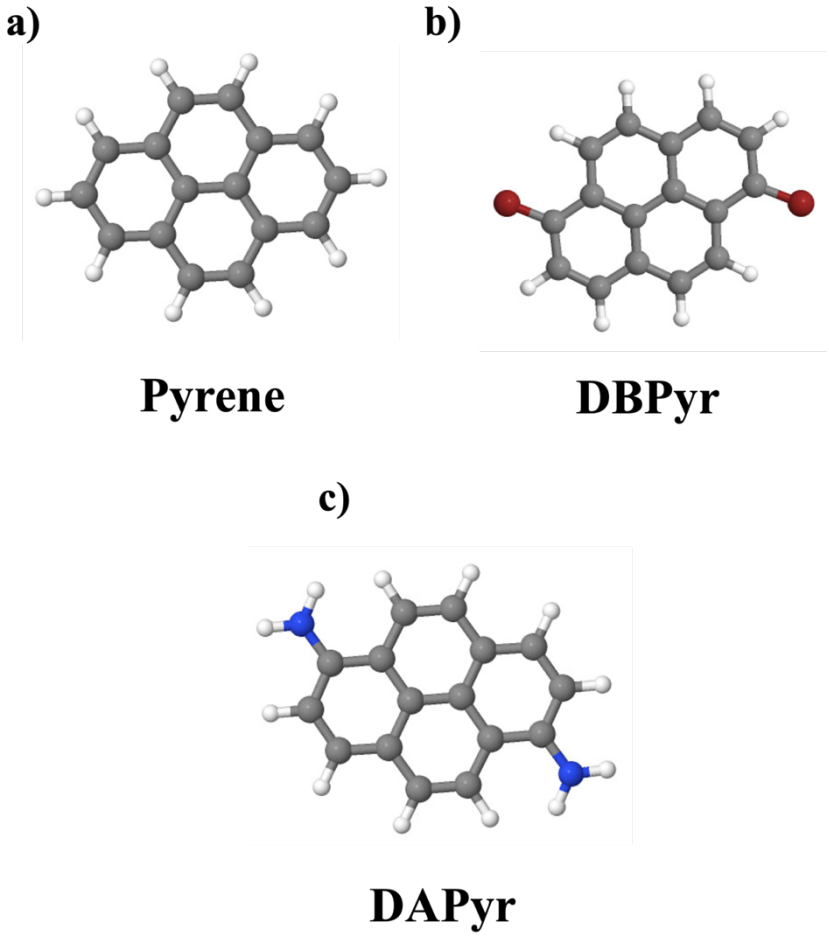

Figure 5.3. Top view of fully relaxed isolated molecules. (a) Pyrene (b) DBPyr (c) DAPyr. (Key: Carbon C = grey, Bromine Br = red, Nitrogen N = blue and Hydrogen H = white).

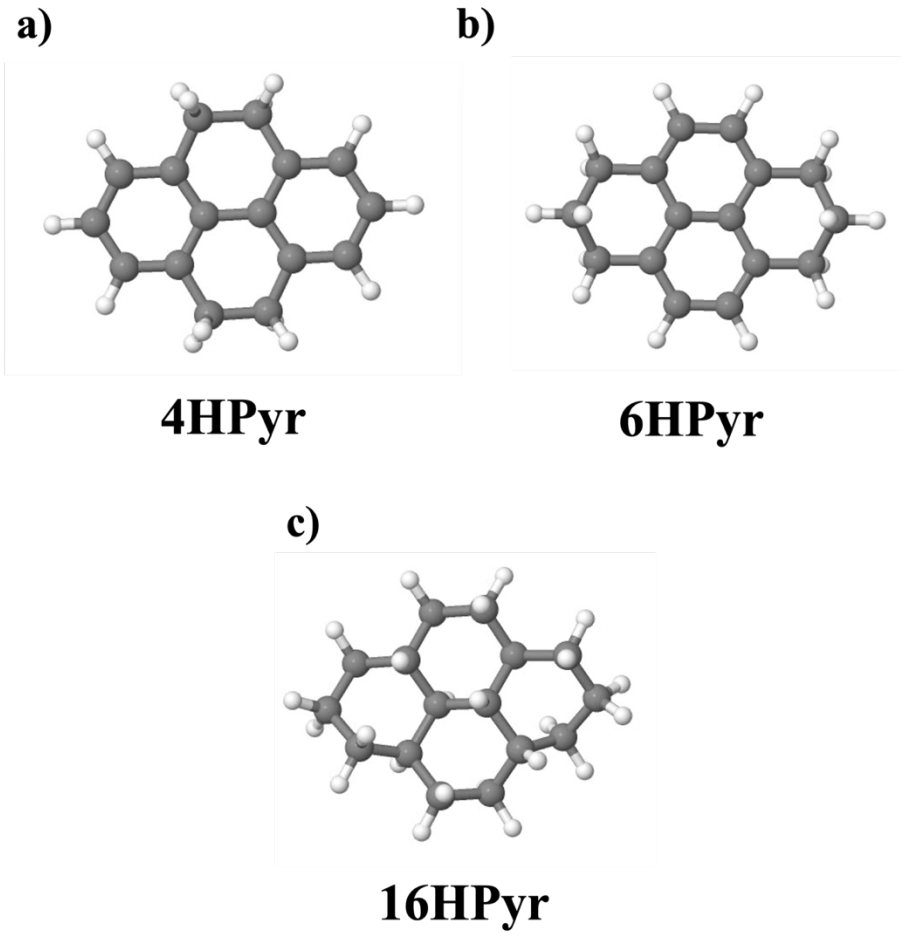

Figure 5.4. Top view of fully relaxed isolated molecules. (a) 4HPyr (b) 6HPyr (c) 16HPyr-a (d) 16HPyr-b. (Key: C = grey and H = white).

5.4 Frontier orbitals

As part of the DFT calculations, I used the methods described in Chapter 2, to first evaluate the wave functions of the molecules (see Figures 5.1 and 5.2) and calculate the HOMO-LUMO gaps in order to gain a detailed understanding of their transport characteristics.

A plot of the frontier orbitals of the group (1): Pyrene, DBPyr, and DAPyr molecules is shown in figures 5.5 to 5.7. The highest occupied molecular orbitals (HOMO), lowest unoccupied molecular orbitals (LUMO), HOMO-1, and LUMO+1 along with their respective energies are shown. In Figures 5.8 to 5.10, the frontier orbitals for the group (2): 4HPyr, 6HPyr, and 16HPyr are also plotted; the highest occupied molecular orbitals HOMO, the lowest unoccupied molecular orbitals LUMO, HOMO-1, and LUMO+1 are also displayed.

According to Table 5.1, Pyrene, DBPyr, and DAPyr have HOMO-LUMO gaps of 2.6, 2.3, and 2.2, respectively. The HOMO-LUMO gaps for 4HPyr, 6HPyr, and 16HPyr are 3.3, 3.1, and 5.1, respectively, as shown in Table 5.1.

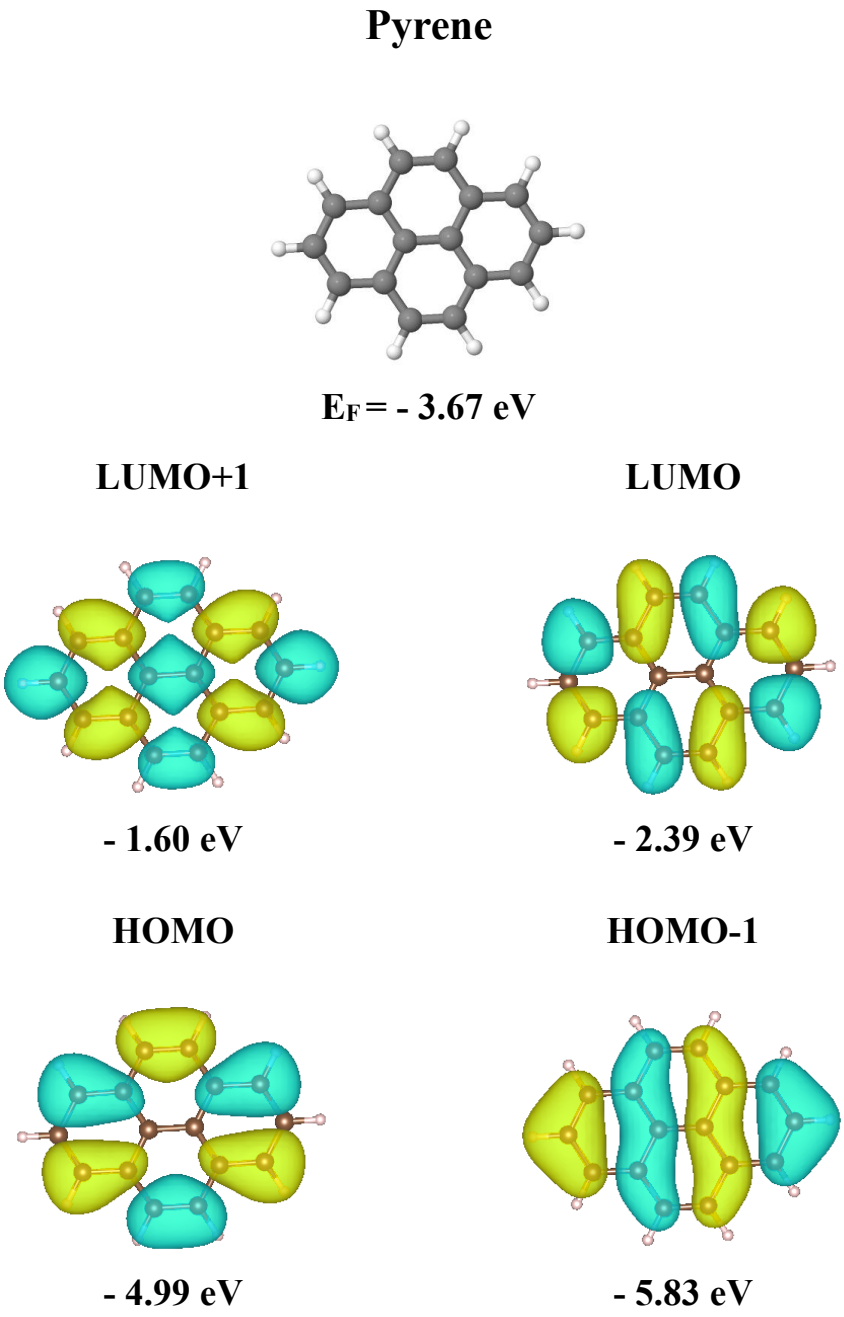

Figure 5.5. Wave functions of Pyrene. Top panel: fully optimised geometry of Pyrene. Lower panel: HOMO, LUMO, HOMO-1, LUMO+1 of pyrene along with their energies.

DBPyr

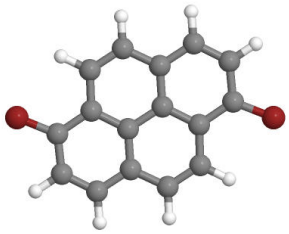

E_F = - 3.68 eV

LUMO+1 **LUMO**

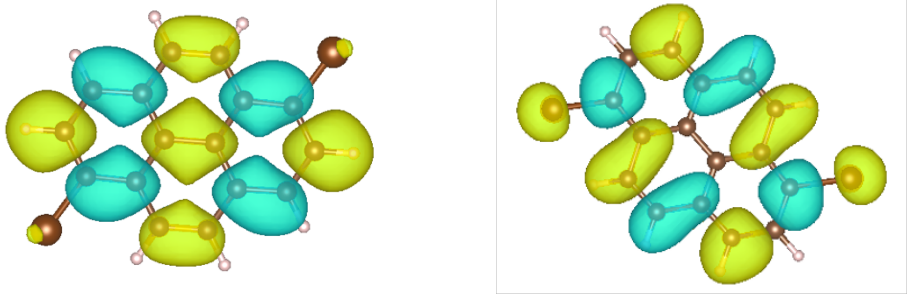

-1.76 eV **-2.50 eV**

HOMO **HOMO-1**

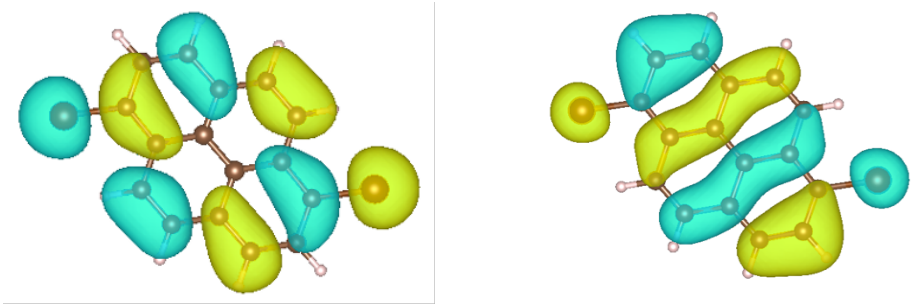

-4.81 eV **-5.81 eV**

Figure 5.6. Wave functions of DBPyr. Top panel: fully optimised geometry of DBPyr. Lower panel: HOMO, LUMO, HOMO-1, LUMO+1 of DBPyr along with their energies.

DAPyr

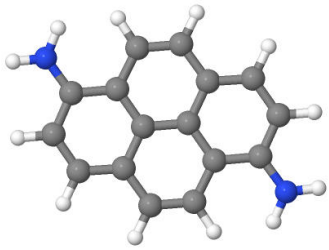

E_F = - 2.72 eV

LUMO+1 **LUMO**

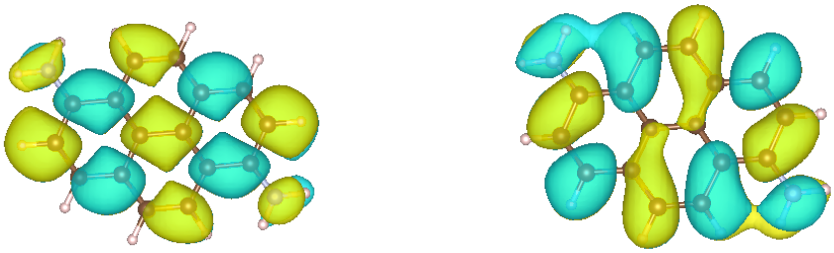

- 1.16 eV **- 1.74 eV**

HOMO **HOMO-1**

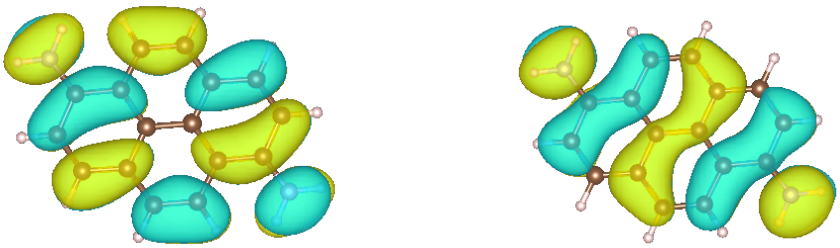

- 3.86 eV **- 5.15 eV**

Figure 5.7. Wave functions of DAPyr. Top panel: fully optimised geometry of DAPyr. Lower panel: HOMO, LUMO, HOMO-1, LUMO+1 of DAPyr along with their energies.

4HPyr

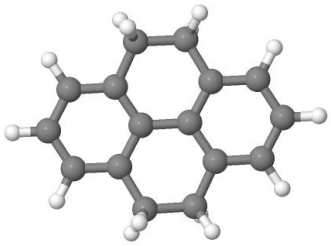

E_F = - 3.54 eV

LUMO+1 **LUMO**

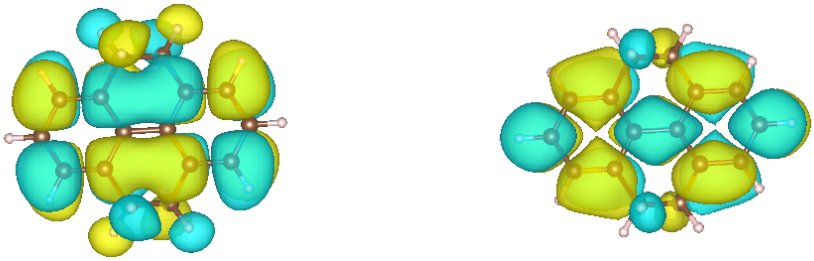

- 1.00 eV **- 1.68 eV**

HOMO **HOMO-1**

- 4.93 eV **- 5.45 eV**

Figure 5.8. Wave functions of 4HPyr. Top panel: fully optimised geometry of 4HPyr. Lower panel: HOMO, LUMO, HOMO-1, LUMO+1 of 4HPyr along with their energies.

6HPyr

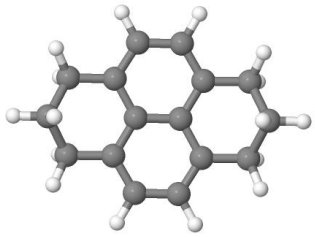

E_F = - 3.73 eV

LUMO+1 **LUMO**

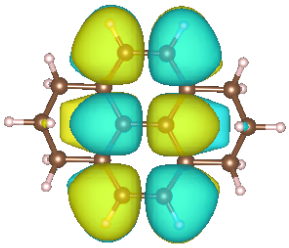

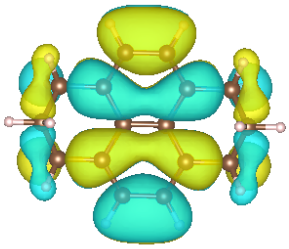

- 1.04 eV **- 1.66 eV**

HOMO **HOMO-1**

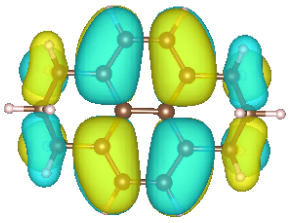

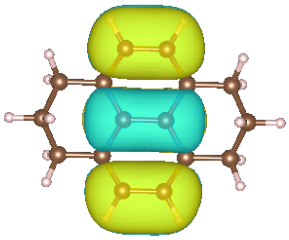

- 4.78 eV **- 5.86 eV**

Figure 5.9. Wave functions of 6HPyr. Top panel: fully optimised geometry of 6HPyr. Lower panel: HOMO, LUMO, HOMO-1, LUMO+1 of 6HPyr along with their energies.

16HPyr

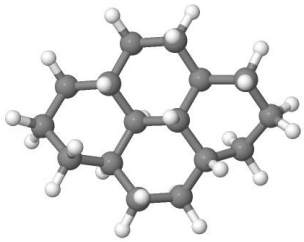

E_F = - 5.19eV

LUMO+1 **LUMO**

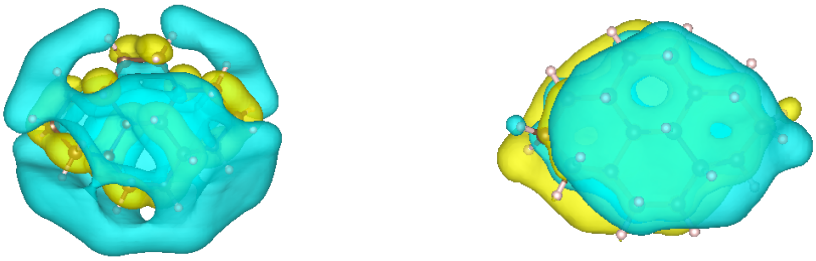

1.16 eV **0.83 eV**

HOMO **HOMO-1**

- 6.21 eV **- 6.23 eV**

Figure 5.10. Wave functions of 16HPyr. Top panel: fully optimised geometry of 16HPyr. Lower panel: HOMO, LUMO, HOMO-1, LUMO+1 of 16HPyr along with their energies.

The studied molecules		The HOMO-LUMO gap
Group (1)	Pyrene	2.6
	DBPyr	2.3
	DAPyr	2.1
Group (2)	4HPyr	3.3
	6HPyr	3.1
	16HPyr	5.19

Table 5.1. HOMO-LUMO gap of studied molecules: group (1) molecules: Pyrene, DBPyr, and DAPyr. And group (2) molecules: 4HPyr, 6HPyr, and 16HPyr.

5.5 Configurations between the studied molecules and graphene sheets

The calculations presented in this study take into account two different stacking configurations between the studied molecules and graphene sheets: AB stacking and AA stacking. Figure 5.11 illustrates AB and AA stacking for the group (1): Pyrene, DBPyr, and DAPyr and Figure 5.12 shows AB and AA stacking for the group (2): 4HPyr, 6HPyr, and 16HPyr.

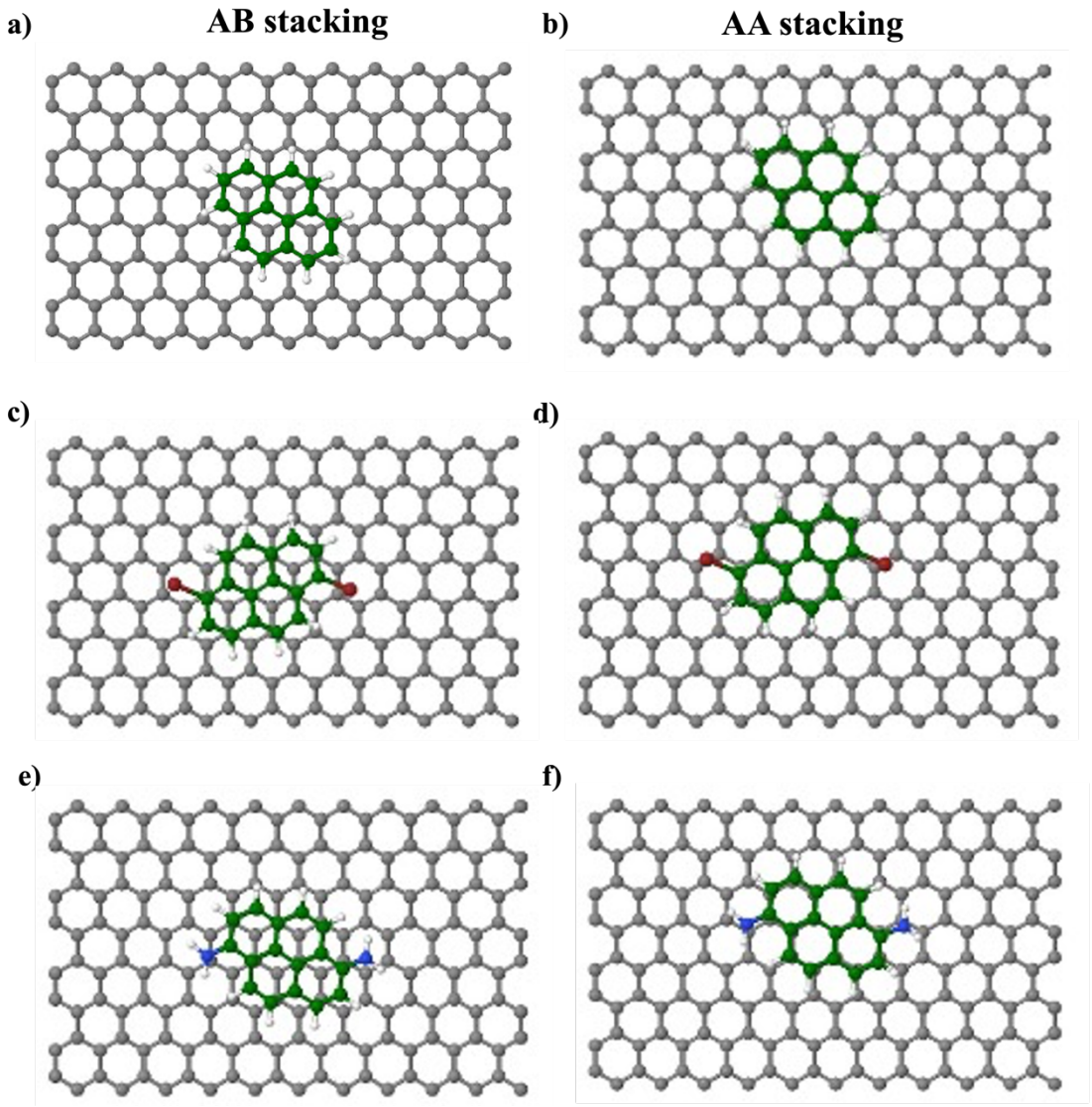

Figure 5.11. Configurations between group (1) molecules and graphene sheet. a) Pyrene form AB stacking with graphene sheet, b) Pyrene form AA stacking with graphene sheet, c) DBPyr form AB stacking with graphene sheet, d) DBPyr form AA stacking with graphene sheet, e) DAPyr form AB stacking with graphene sheet, f) DAPyr form AA stacking with graphene sheet. (The green colour is to distinguish the molecule from the graphene sheet).

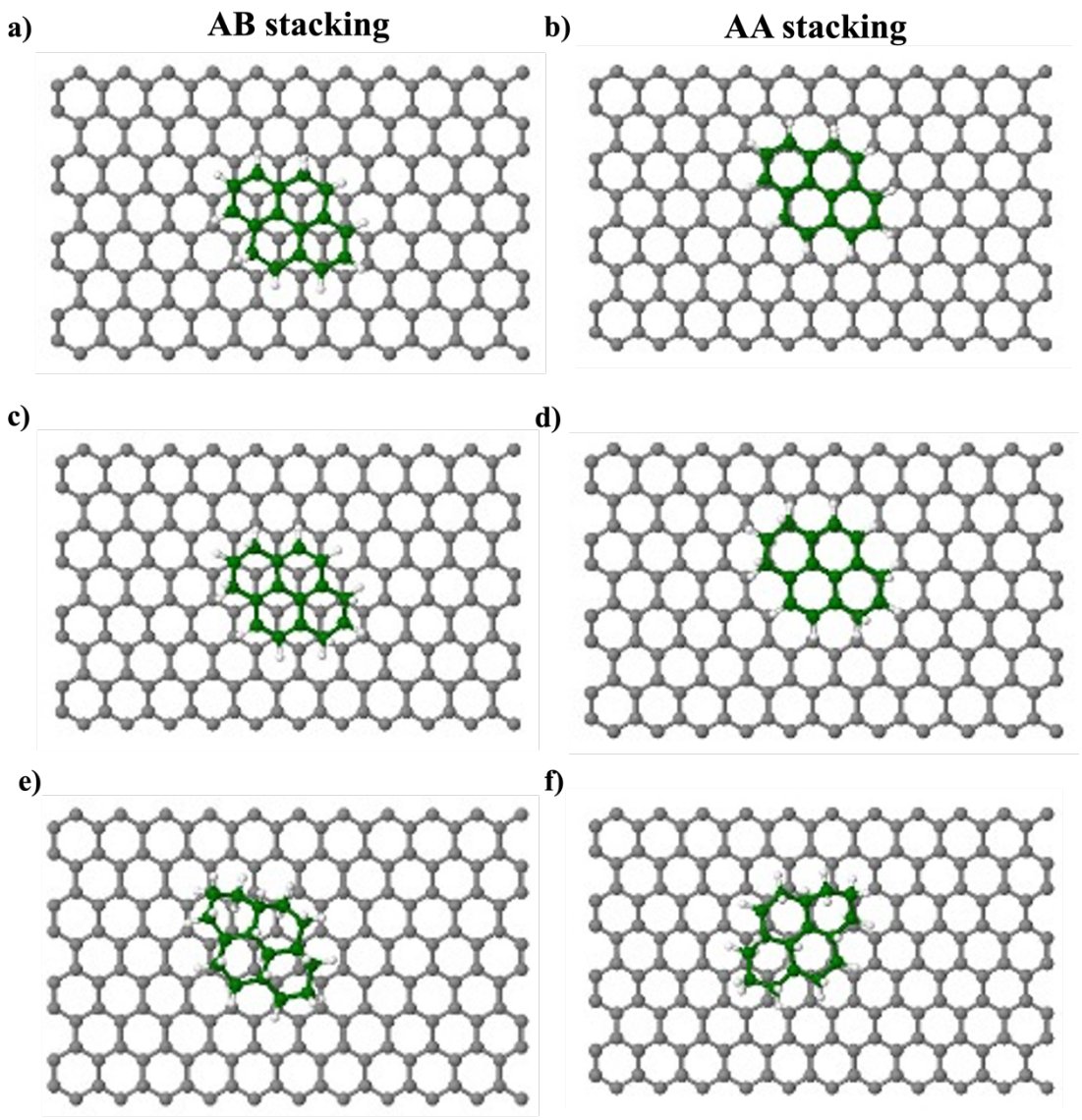

Figure 5.12. Configurations between group (2) molecules and graphene sheet. a) 4HPyr form AB stacking with graphene sheet, b) 4HPyr form AA stacking with graphene sheet, c) 6HPyr form AB stacking with graphene sheet, d) 6HPyr form AA stacking with graphene sheet, e) 16HPyr form AB stacking with graphene sheet, f) 16HPyr form AA stacking with graphene sheet. (The green colour is to distinguish the molecule from the graphene sheet).

5.6 Determine the distance by optimising

The purpose of this section is to determine the distance between the graphene sheet and the molecules under study. To achieve that, the molecules of group (1) and group (2) were placed above the graphene sheet and then the half-junction was relaxed using SIESTA [23]. The Van der Waals density functional [24] (vdW-DF) was used with a double-polarized atomic orbital basis for carbon, bromine, nitrogen, and hydrogen. The Mesh cut-off energy is set to 200 Rydberg. The molecules relax over the fixed graphene sheet until the force between atoms becomes 0.02 eV/ Å. Below, I describe the measured optimum distance between the molecules in groups (1) and (2) and the graphene sheet.

5.6.1 Determine the distance for the group (1)

Here, the optimised half-junctions for Pyrene, DBPyr, and DAPyr are obtained, and the optimum distance between the bottom graphene sheet and the group (1) molecules is measured.

As shown in Figure 5.13, the optimum distance in the case of AB stacking is found to be 3.17 Å with a total energy of -29802.7 eV for Pyrene, 3.20 Å with a total energy of -30491eV for DBPyr and 3.15Å with a total energy of -30374.7 eV, for DAPyr. Additionally, the optimum distances are measured for AA stacking and found to be 3.27 Å with a total energy of -29802.5 eV, 3.31 Å a with total energy of -30490.8 eV and 3.27 Å with a total energy of -30374.5 eV for Pyrene, DBPyr, and DAPyr respectively.

Table 5.2 and Table 5.3 summarize the optimum distances and their corresponding total energies mentioned above.

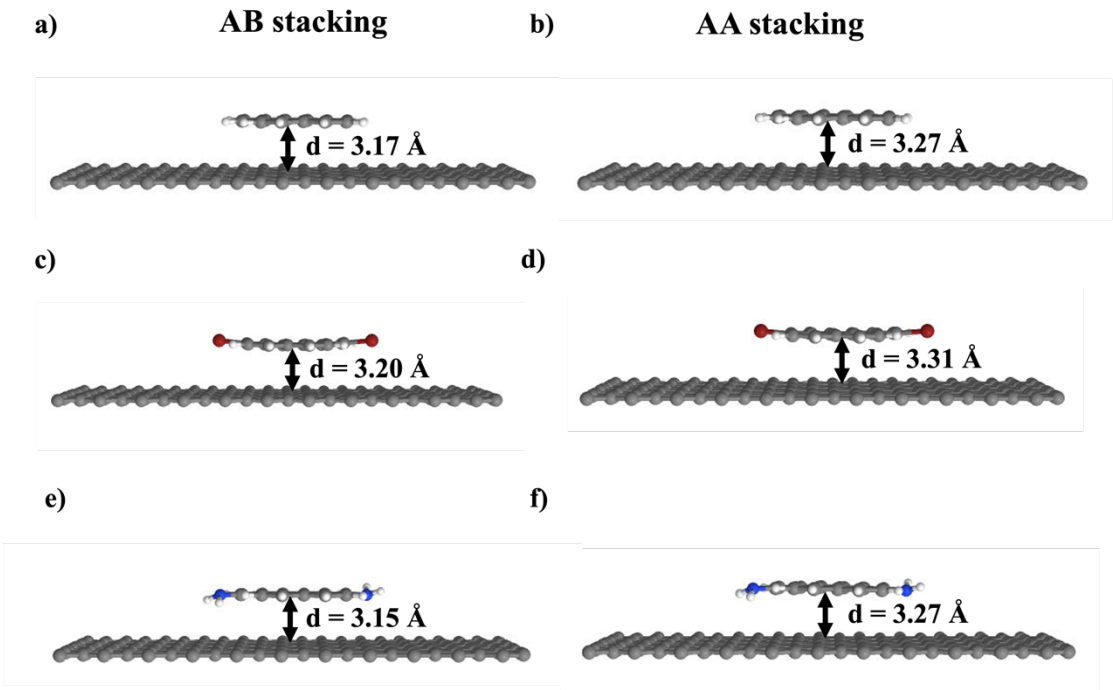

Figure 5.13. The optimised half-junctions of the group (1) in the case of AB and AA stacking. a) half-junction based on Pyrene in the case of AB stacking, b) half-junction based on Pyrene in case of AA stacking, c) half-junction based on DBPyr in case of AB stacking, d) half-junction based on DBPyr in case of AA stacking, e) half-junction based on DAPyr in case of AB stacking, f) half-junction based on DAPyr in case of AA stacking.

Group (1) molecules AB configuration		
	The distance($A°$)	**The total energy(eV)**
Pyrene	3.17	-29802.7
DBPyr	3.20	-30491
DAPyr	3.15	-30374.7

Table 5.2. The optimum distances with their corresponding total energy for group (1) molecules for AB configuration.

Group (1) molecules AA configuration		
	The distance($A°$)	**The total energy(eV)**
Pyrene	3.27	-29802.5
DBPyr	3.31	-30490.8
DAPyr	3.27	-30374.5

Table 5.3. The optimum distances with their corresponding total energy for group (1) molecules for AA configuration.

5.6.2 Determine the distance for the group (2)

The optimised half-junctions based on 4HPyr, 6HPyr, and 16HPyr are obtained for both AB and AA stacking, and then the optimum distance between the bottom graphene sheet and the molecules is determined.

As described in section (5.2), group (2) molecules have different degrees of conjugation as a result of planarity. Therefore, to calculate the optimum distances, I measured the distance between each carbon atom of the molecules and the graphene sheet and then calculated the average of all distances. Figure 5.14 shows the average optimum distances for 4HPyr, 6HPyr and 16HPyr are 3.29 Å, 3.46 Å and 3.79 Å with total energy -29867.4 eV, -29900.2 eV and -30062.8 eV respectively for AB stacking configuration. While, in the case of AA stacking configuration the average optimum distances for 4HPyr, 6HPyr and 16HPyr are measured to be 3.43 Å, 3.51 Å and 4.02 Å with total energies -29867.3 eV, -29900 eV and -30062.8 eV respectively. Clearly, compared to 4HPyr and 6HPyr, non-planar 16HPyr is the most weakly coupled to the graphene

electrodes. The optimum distances mentioned above with their total energies are summarized in Table 5.4 and Table 5.5.

Group (2) molecules AB configuration		
	The distance($A°$)	**The total energy(eV)**
4HPyr	3.29	-29867.4
6HPyr	3.46	-29900.2
16HPyr	3.79	-30062.8

Table 5.4. The optimum distances with their corresponding total energy for group (2) molecules for AB configuration.

Group (2) molecules AA configuration		
	The distance($A°$)	**The total energy(eV)**
4HPyr	3.43	-29867.3
6HPyr	3.51	-29900
16HPyr	4.02	-30062.8

Table 5.5. The optimum distances with their corresponding total energy for group (2) molecules for AA configuration.

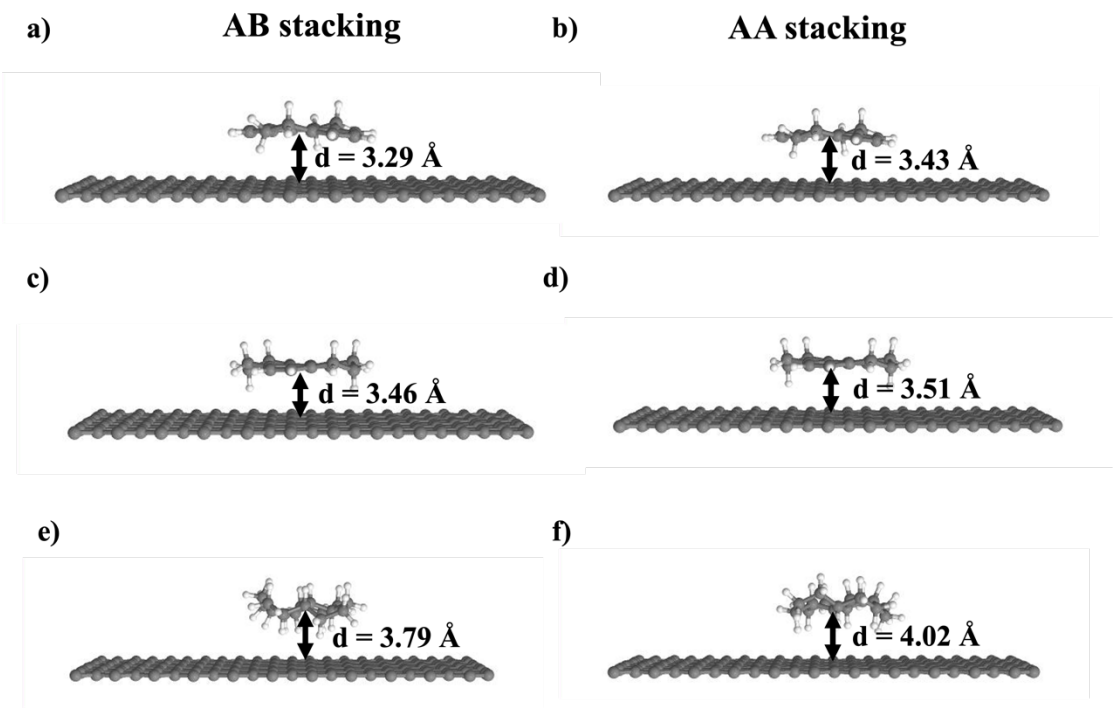

Figure 5.14. The optimised half-junction of the group (2) for AB and AA stacking. a) half-junction based on 4HPyr in case of AB stacking, b) half-junction based on 4HPyr in case of AA stacking, c) half-junction based on 6HPyr in case of AB stacking with, d) half-junction based on 6HPyr in case of AA stacking, e) half-junction based on 16HPyr in case of AB stacking, f) half-junction based on 16HPyr in case of AA stacking.

5.7 The optimized cross-plane molecular junctions

After obtaining the optimum geometry for each half-junction, as discussed in the previous section, I used the optimum distance to construct the cross-plane junction in which the studied molecule lies between two graphene sheets.

In the following step, I used the SIESTA code again to optimise the cross-plane junctions formed by the studied molecules. The Van der Waals density function (vdW-

DF) with double-polarized atomic orbital bases set for carbon, bromine, nitrogen, and hydrogen was used and the Mesh cut-off energy was set to 200. The studied molecules are relaxed between two fixed graphene sheets until the tolerance force reaches 0.02 eV/ Å. Figure 5.15 shows the top and side views of the optimized cross-plane junctions for Pyrene, DBPyr, and DAPyr in the group (1). Also, Figure 5.16 illustrates both the top and side views of the optimized cross-plane junction for the group (2): 4HPyr, 6HPyr, and 16HPyr. The green colour is used to distinguish molecules in the junction from grey graphene sheets. It is clear from the top view of the junction that the molecules studied, and the graphene sheets are arranged in AB and AA configurations. Also, due to the non-planarity of 16HPyr, the AB and AA stacking is not perfect.

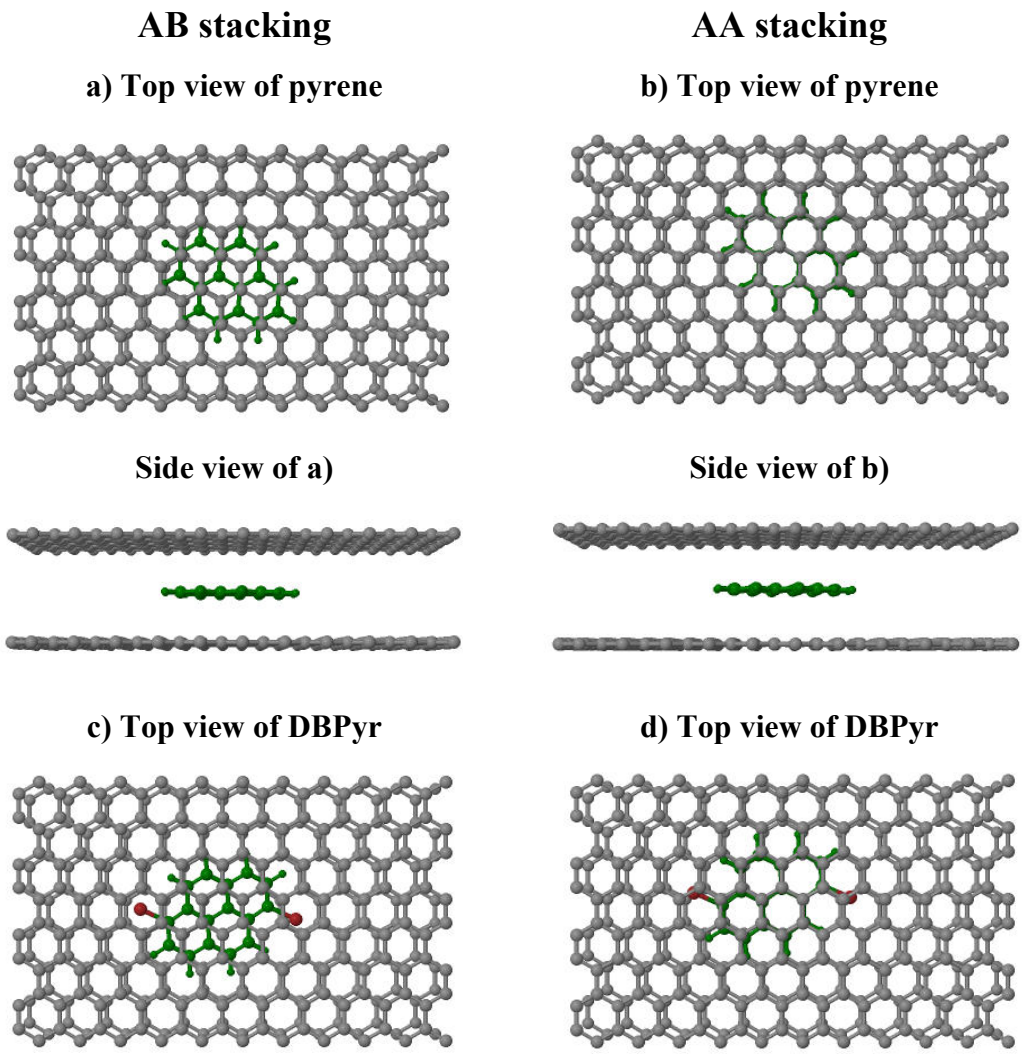

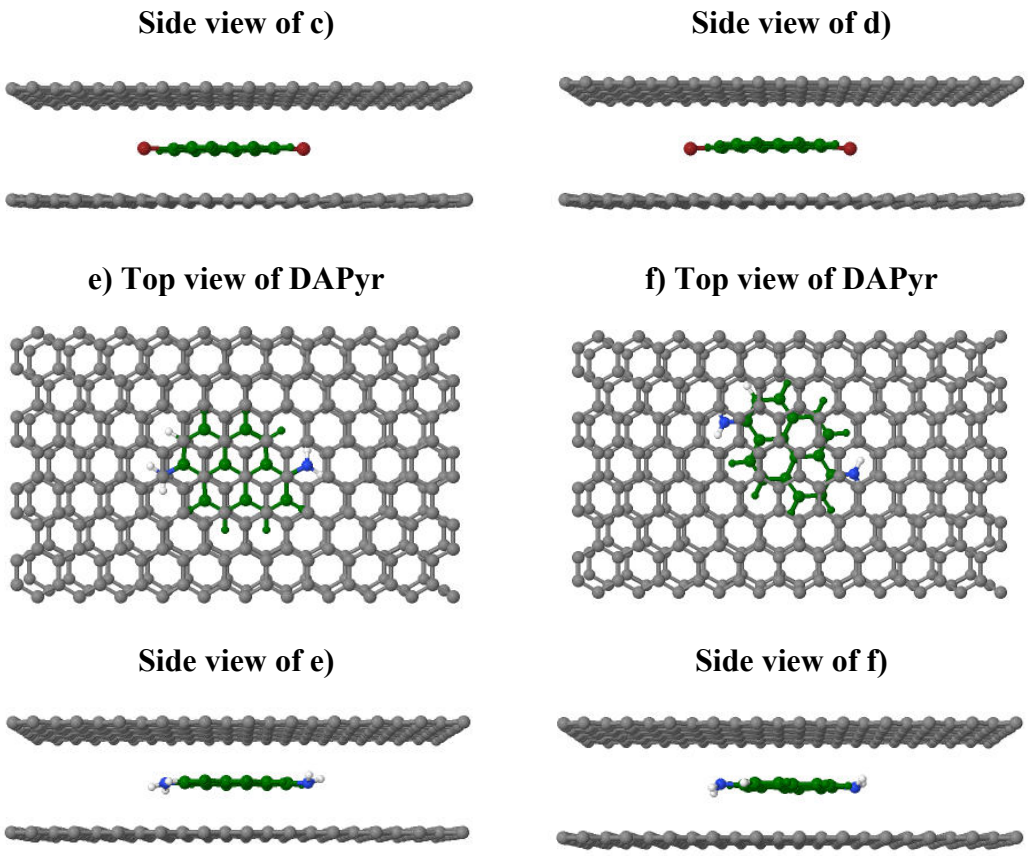

Figure 5.15. Top row: (a) Top view of the cross-plane junction of pyrene, Bottom row (a) Side view of the sandwiched cross-plane junction of pyrene for AB configuration. Top row: (b) Top view of the cross-plane junction of pyrene, Bottom row (b) Side view of the sandwiched cross-plane junction of pyrene for AA configuration. (c) Top view of the cross-plane junction of DBPyr, Bottom row (c) Side view of the sandwiched cross-plane junction of DBPyr for AB configuration. (d) Top view of the cross-plane junction of DBPyr, Bottom row (d) Side view of the sandwiched cross-plane junction of DBPyr for AA configuration. (e) Top view of the cross-plane junction of DAPyr, Bottom row (e) Side view of the sandwiched cross-plane junction of DAPyr for AB configuration. (f) Top view of the cross-plane junction of DAPyr, Bottom row (f) Side view of the sandwiched cross-plane junction of DAPyr for AA configuration.

AB stacking

a) Top view of 4HPyr

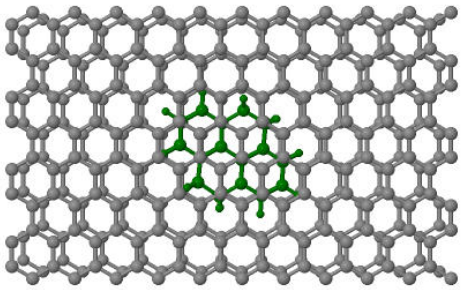

Side view of a)

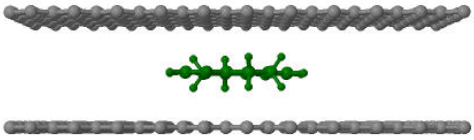

c) Top view of 6HPyr

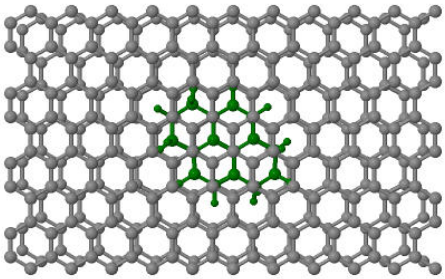

Side view of c)

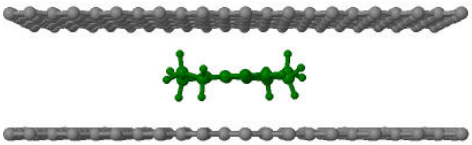

e) Top view of 16HPyr

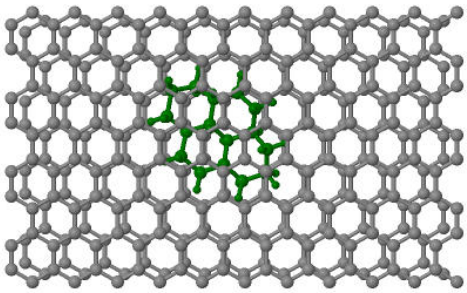

Side view of e)

AA stacking

b) Top view of 4HPyr

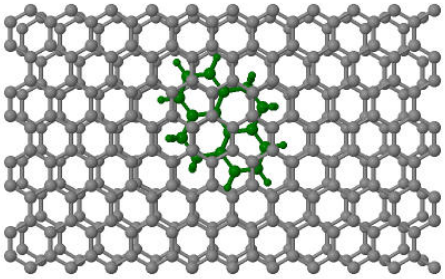

Side view of b)

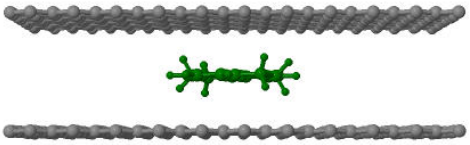

d) Top view of 6HPyr

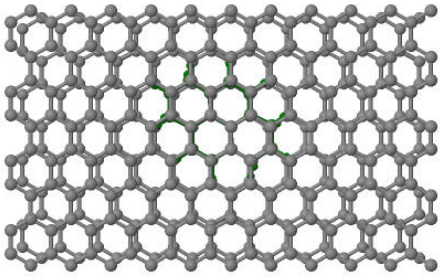

Side view of d)

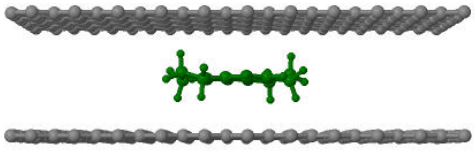

f) Top view of 16HPyr

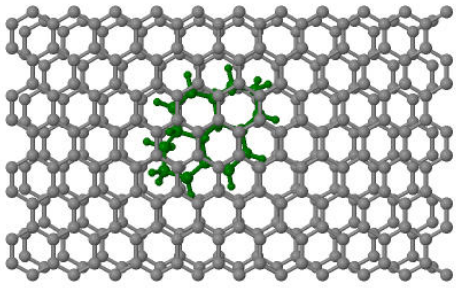

Side view of f)

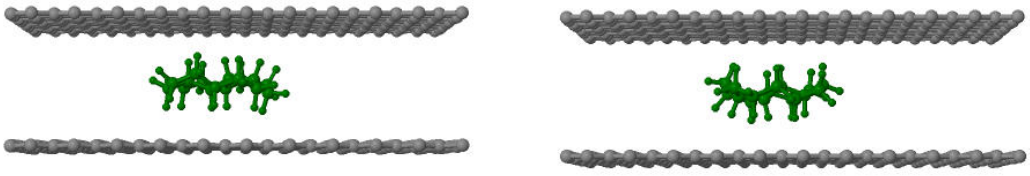

Figure 5.16. Top row: (a) Top view of the cross-plane junction of 4HPyr, Bottom row (a) Side view of the sandwiched cross-plane junction of pyrene for AB configuration. Top row: (b) Top view of the cross-plane junction of 4HPyr, Bottom row (b) Side view of the sandwiched cross-plane junction of pyrene for AA configuration. (c) Top view of the cross-plane junction of 6HPyr, Bottom row (c) Side view of the sandwiched cross-plane junction of 6HPyr for AB configuration. (d) Top view of the cross-plane junction of 6HPyr, Bottom row (d) Side view of the sandwiched cross-plane junction of 6HPyr for AA configuration. (e) Top view of the cross-plane junction of 16HPyr, Bottom row (e) Side view of the sandwiched cross-plane junction of 16HPyr for AB configuration. (f) Top view of the cross-plane junction of 16HPyr, Bottom row (f) Side view of the sandwiched cross-plane junction of 16HPyr for AA configuration.

5.8 Transmission function calculations

To further reveal the electrical properties of cross-plane molecular junctions, the transmission coefficients *T(E)* are calculated using the density functional code SIESTA [23] and the quantum transport code GOLLUM [25].

My first step will be to describe the graphene sheet and the leads that are used in my DFT calculations. An example of a cross-plane molecular junction is shown in Figure 5.17 (a), where the molecule is sandwiched between two graphene sheets. Each graphene sheet is extended to $\mp\infty$ in the z-direction and periodic boundary conditions are used in the y-direction to avoid edge effects. A total of four leads are involved in the calculations (see Figure 5.17 a; I used green to discriminate the leads). Figure 5.17 (b) provides additional information about the graphene sheet and the leads. The graphene sheet has a length of 25.84 Å and a width of 15.62 Å. As can be seen on the right, the lead contains 32 atoms. Following this, cross-plane currents are injected from lead 1 and collected from leads 3 and 4. Therefore, the transmission function curves plotted in this section represent the summation of the transmission functions from lead 1 to lead 3 and lead 4 (see the purple arrows in Figure 5.17 a). The transmission function of group (1) and (2) molecules is calculated by sandwiching them between the two graphene sheets as described below.

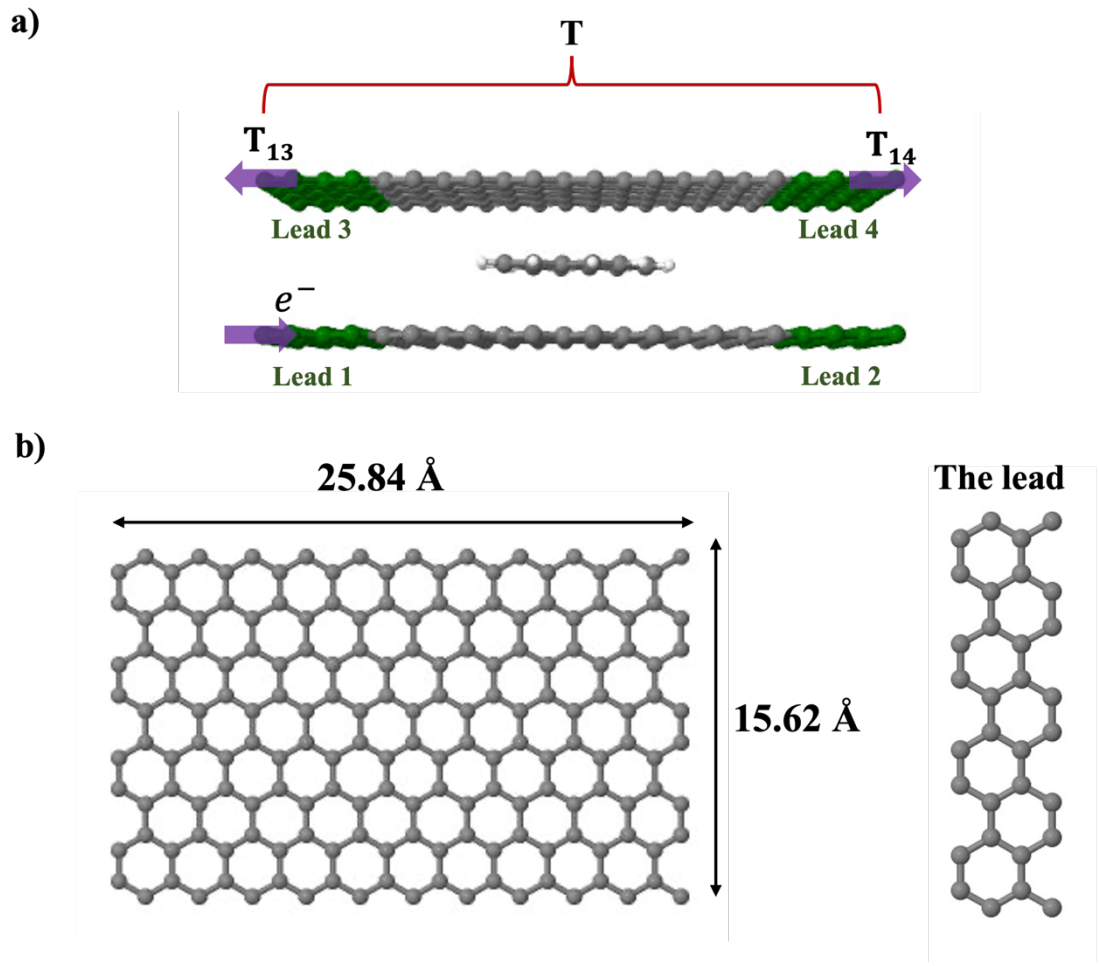

Figure 4.17. (a) Sandwiched structures of the molecular junction formed from Pyrene. The green colour represents lead 1, 2, 3 and 4, which are used as electrodes. The electron is injected from lead 1 and the transmission coefficient T is collected by lead 3 and 4 (the transmission function curves represent the summation of $T = T_{13}+T_{14}$). (b) The finite graphene sheet (left), The lead (right).

5.8.1 Transmission function calculations for group (1)

This section presents the transmission functions for group (1) molecules: Pyrene, DBPyr and DAPyr to study the effect of introducing electron-withdrawn substituents (-Br) and electron-donating substituents (-NH_2) on electron transport in cross-plane molecular junctions.

Figure 5.18 shows transmission spectra for both AB and AA configurations for Pyrene (a-b), DBPyr (c-d) and DAPyr (e-f). To compare DFT results and demonstrate the effect of substituent groups, including electron-withdrawn groups (-Br) as well as electron-donating groups (-NH_2), I have collected transmission function curves of Pyrene, DBPyr, and DAPyr for the AB configuration in Figure 5.19 (a), while the transmission function curves of Pyrene, DBPyr, and DAPyr for the AA configuration are shown in Figure 5.19 (b). The results indicate that in both AB and AA configurations, the transmission functions of the molecular junctions containing DAPyr and DBPyr are higher than those in Pyrene at Fermi energy E_F (dotted vertical black line, predicted by DFT), which can be related to a decrease in the HOMO -LUMO gap for the corresponding molecules (see Table 5.1).

It can be concluded that the introduction of substituent groups, both electron-withdrawn and electron-donating groups, enhances the electron transport in cross-plane molecular junctions to different degrees. It is possible that the introduction of substituents around the aromatic ring of pyrene provides more transport channels for electron transport. This shows a different pattern from conventional metal electrode in-plane transport where the electron-donating substituents increase the molecular junction conductance, and the electron-withdrawing substituents decrease the molecular junction conductance [26].

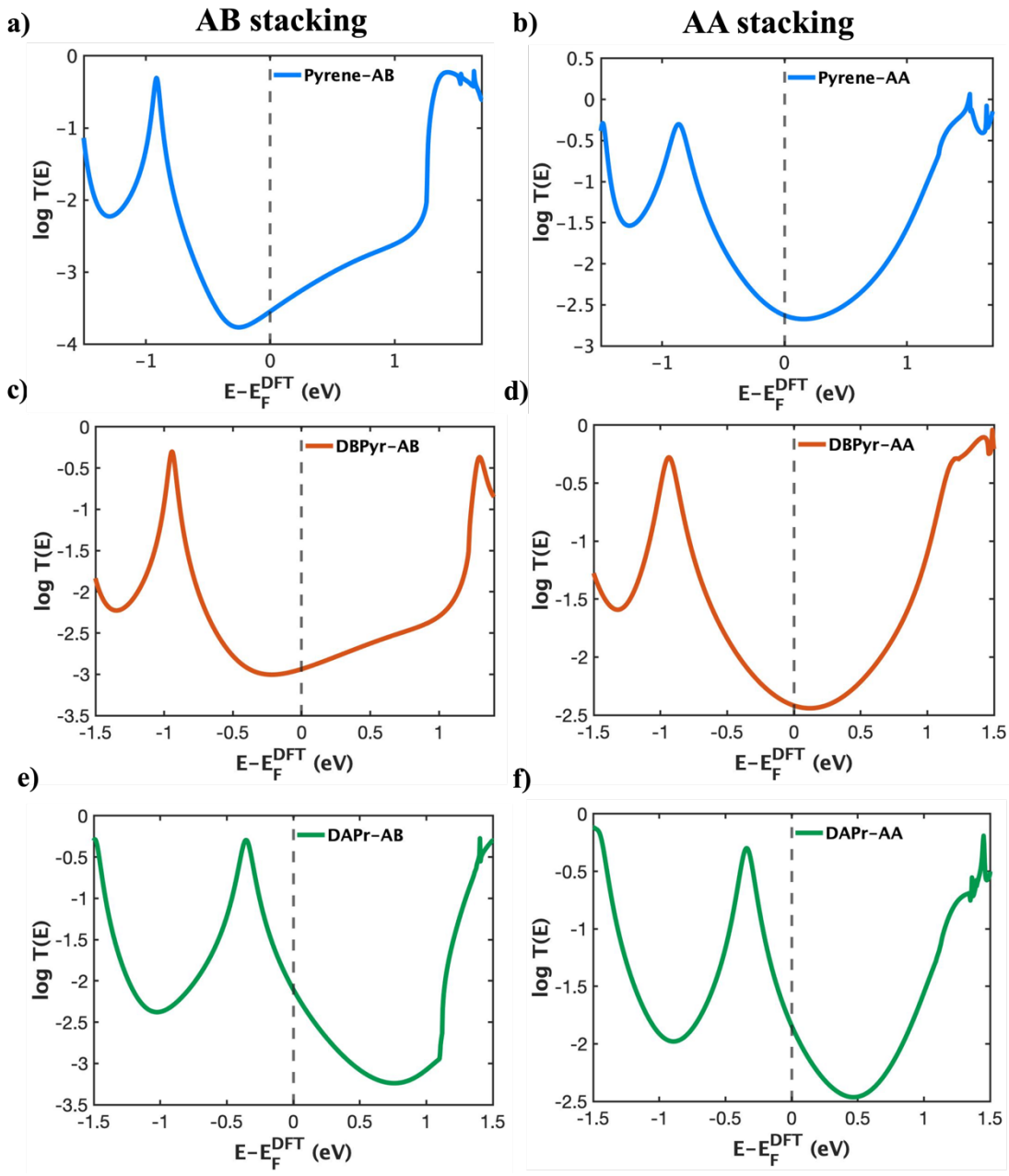

Figure 5.18. DFT-based transmission functions of Pyrene, DBPyr and DAPyr for both AB and AA configurations. (a) Transmission functions for Pyrene in case of AB configuration, (b) Transmission functions for Pyrene in case of AA configuration, (c) Transmission functions for DBPyr in case of AB configuration, (d) Transmission functions for DBPyr in case of AA configuration, (e) Transmission functions for DAPyr in case of AB configuration, and (f) Transmission functions for DAPyr in case of AA configuration.

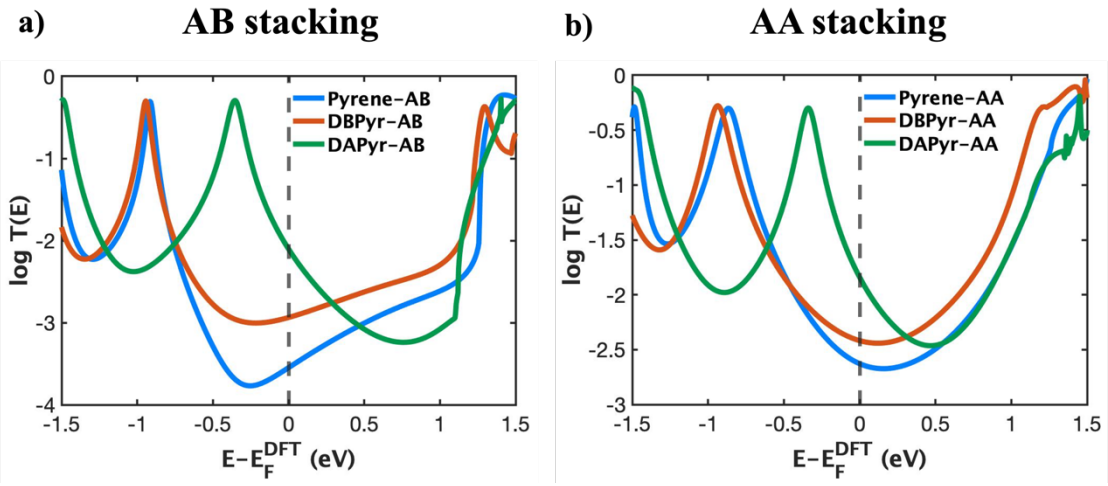

Figure 5.19. Theoretical simulations for group (1) molecules for AB and AA stacking. (a) Transmission spectra for Pyrene (blue), DBPyr (orange), and DAPyr (green) in AB stacking case, (b) Transmission spectra for Pyrene (blue), DBPyr (orange), and DAPyr (green) in AA stacking case.

5.8.2 Transmission function calculations for group (2)

To study the effects of conjugation and planarity in cross-plane molecular graphene junctions, I calculate the transmission function of 4HPyr, 6HPyr, and 16HPyr. Figure 5.20 shows the transmission spectra of molecular junctions based on 4HPyr, 6HPyr and 16HPyr for both AB and AA stacking.

The molecular junction constructed by 6HPyr exhibits higher transmission than the molecular junction of 4HPyr and 16HPyr at Fermi energy E_F (indicated by a black dotted line) for AB stacking as shown in Figure 5.21 (a). Moreover, For AA stacking Figure 5.21 (b) shows that 6HPyr has the highest transmission spectra compared to 4HPyr and 16HPyr. According to these results, the conductance of the cross-plane graphene junctions decreases with decreasing conjugation of the π system. As the

degree of conjugation of the three molecules gradually decreases, the conductance of their constructed molecular junctions decreases accordingly, which is consistent with the conclusion that disruption of the conjugated structure affects the electrical transport of graphene/fullerene single molecule/graphene junctions [27].

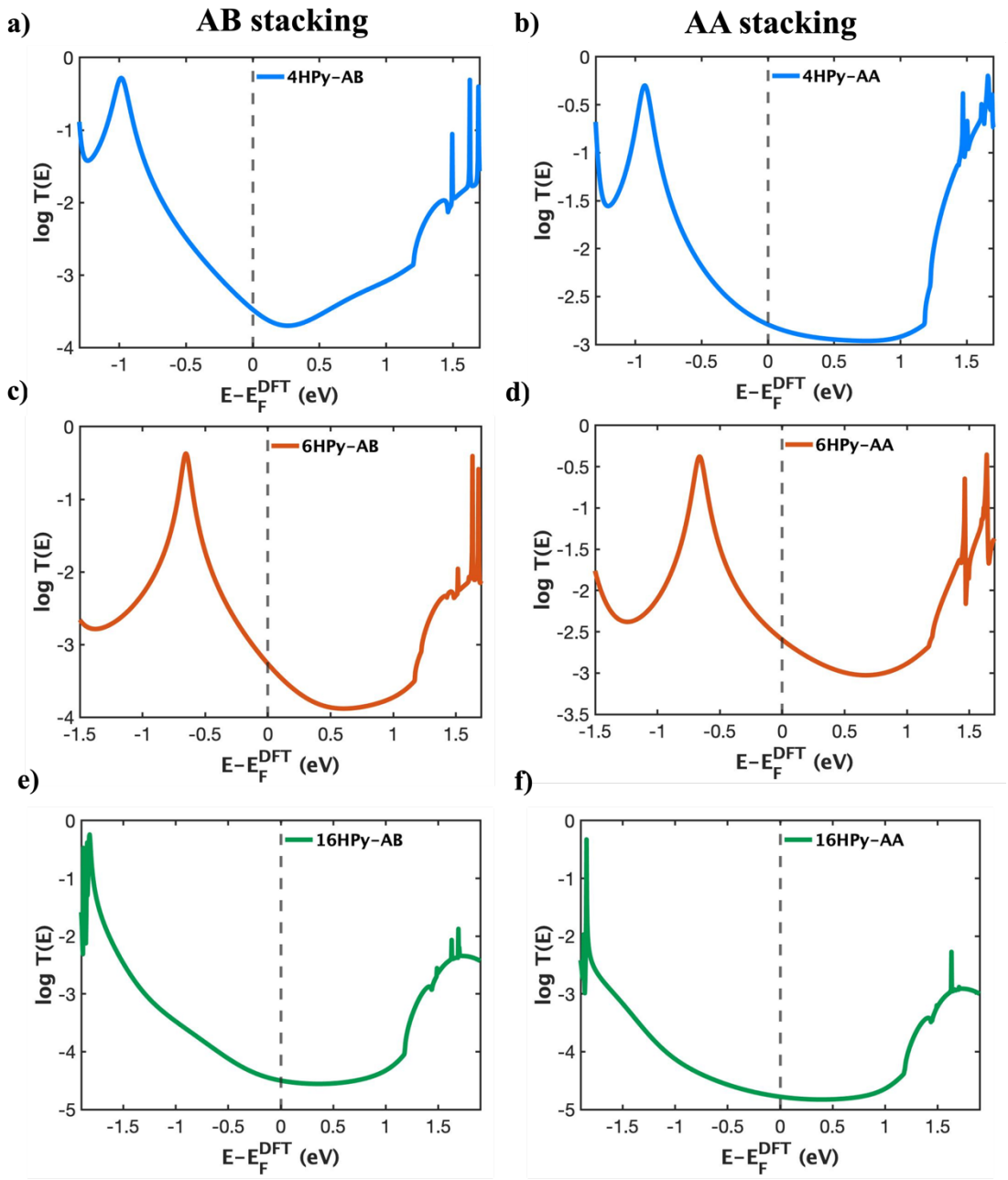

Figure 5.20. DFT-based transmission functions of 4HPyr, 6HPyr and 16HPyr for AB and AA configurations. (a) Transmission functions for 4HPyr in case of AB configuration, (b) Transmission functions for 4HPyr in case of AA configuration, (c) Transmission functions for 6HPyr in case of AB configuration, (d) Transmission functions for 6HPyr in case of AA configuration, (e) Transmission functions for 16HPyr in case of AB configuration, and (f) Transmission functions for 16HPyr in case of AA configuration.

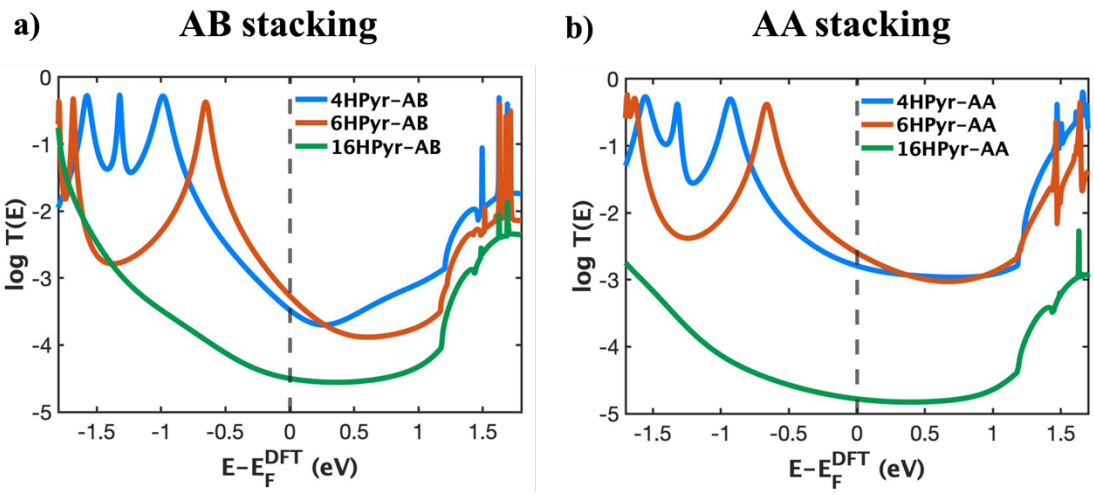

Figure 5.21. Theoretical simulations for group (2) molecules for AB and AA stacking. (a) Transmission spectra for 4HPyr (blue), 4HPyr (orange), and 16HPyr (green) in AB stacking, (b) Transmission spectra for 4HPyr (blue), 4HPyr (orange), and 16HPyr (green) in AA stacking.

5.9 Comparison of DFT results with experimental results

The purpose of this section is to compare the DFT results (discussed in the previous section) with experimental data obtained by collaborators at Xiamen University as shown in Figure 5.22.

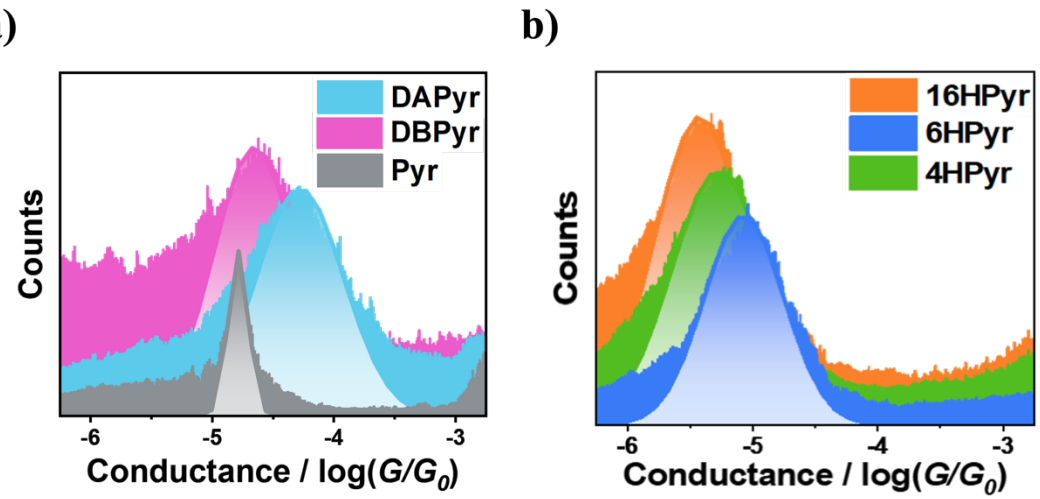

Figure 5.22. a) 1D conductance histograms for Pyr (grey), DAPyr (light blue) and DBPyr (pink) Molecule-vdWHs. b) The 1D conductance histograms for 6HPyr (blue), 4HPyr (green), and 16HPyr (orange) Molecule-vdWHs.

In Figure 5.22 (a), 1D conductance histograms are shown for DAPyr, DBPyr, and pyrene. According to the results, DAPyr and DBPyr have greater electrical conductance than pyrene. This is in agreement with the DFT results for both AB and AA stackings (see section 5.8.1). Additionally, Figure 5.22 (b) shows the electrical conductance of the molecular junctions based on 6HPyr, 4HPyr, and 16HPyr. In this case, the electrical conductance of the molecular junction decreases with the weakening of the molecular conjugation, which is consistent with the DFT calculations presented in section (5.8.2).

5.10 Conclusion

To summarize, I have investigated the impact of substituents on the cross-plane charge transport in graphene-molecule-graphene junctions using density functional theory DFT. I found that both electron-withdrawing and electron-donating substituents can

enhance electron transport of interlayer transport, which is different from the regular in-plane transport of conventional metal electrodes. DFT calculations show that this increase appears to be correlated with a decrease in the HOMO - LUMO gap of the corresponding molecules.

In addition, non-fully planar organic molecules with different degrees of conjugation and planarity have been chosen to construct single molecular junctions. The results show that the conductance of molecular junctions gradually decreases as the degree of molecular conjugation decreases, which is consistent with the electron transport variation pattern of in-plane transport of molecular junctions in conventional metal electrodes.

5.11 Bibliography

[1] Guldi DM, Nishihara H, Venkataraman L. Molecular wires. Chem Soc Rev 2015; 44:842-844.

[2] Sedghi G, Garcia-Suarez VM, Esdaile LJ, Anderson HL, Lambert CJ, Martin S, Bethell D, Higgins SJ, Elliott M, Bennett N, Macdonald JE, Nichols RJ. Long-range electron tunnelling in oligo-porphyrin molecular wires. Nat Nanotechnol 2011; 6:517-523.

[3] Seong Ho Choi BK, C. Daniel Frisbie. Electrical Resistance of Long Conjugated Molecular Wires. SCIENCE 2008; 320.

[4] Tao NJ. Electron transport in molecular junctions. Nature Nanotechnology volume 2006.

[5] Chuancheng Jia AM, Na Xin, Shaoyun Huang, Jinying Wang, Qi Yang, Shuopei Wang, Hongliang Chen, Duoming Wang, Boyong Feng, Zhirong Liu, Guangyu Zhang, Da-Hui Qu, He Tian, Mark A. Ratner, H. Q. Xu, Abraham Nitzan, Xuefeng Guo. Covalently bonded single-molecule junctions with stable and reversible photoswitched conductivity. SCIENCE 2016.

[6] Roldan D, Kaliginedi V, Cobo S, Kolivoska V, Bucher C, Hong W, Royal G, Wandlowski T. Charge transport in photoswitchable dimethyldihydropyrene-type single-molecule junctions. J Am Chem Soc 2013; 135:5974-5977.

[7] Moreno-Garcia P, Gulcur M, Manrique DZ, Pope T, Hong W, Kaliginedi V, Huang C, Batsanov AS, Bryce MR, Lambert C, Wandlowski T. Single-molecule conductance of functionalized oligoynes: length dependence and junction evolution. J Am Chem Soc 2013; 135:12228-12240.

[8] Capozzi B, Xia J, Adak O, Dell EJ, Liu ZF, Taylor JC, Neaton JB, Campos LM, Venkataraman L. Single-molecule diodes with high rectification ratios through environmental control. Nat Nanotechnol 2015; 10:522-527.

[9] Sadeghi H, Sangtarash S, Lambert CJ. Oligoyne Molecular Junctions for Efficient Room Temperature Thermoelectric Power Generation. Nano Lett 2015; 15:7467-7472.

[10] Sergey Kubatkin AD, Mattias Hjort, Je´roˆme Cornil, Jean-Luc Bre´das, Nicolai Stuhr-Hansen, Per Hedega˚rd& Thomas Bjørnholm. Single-electron transistor of

a single organic molecule with access to several redox states. NATURE 2003.

[11] Rudnev AV, Kaliginedi V, Droghetti A, Ozawa H, Kuzume A, Haga MA, Broekmann P, Rungger I. Stable anchoring chemistry for room temperature charge transport through graphite-molecule contacts. Sci Adv 2017; 3:e1602297.

[12] Kim T, Liu ZF, Lee C, Neaton JB, Venkataraman L. Charge transport and rectification in molecular junctions formed with carbon-based electrodes. Proc Natl Acad Sci U S A 2014; 111:10928-10932.

[13] Seo S, Min M, Lee SM, Lee H. Photo-switchable molecular monolayer anchored between highly transparent and flexible graphene electrodes. Nat Commun 2013; 4:1920.

[14] Lortscher E. Wiring molecules into circuits. Nat Nanotechnol 2013; 8:381-384.

[15] El Abbassi M, Sangtarash S, Liu X, Perrin ML, Braun O, Lambert C, van der Zant HSJ, Yitzchaik S, Decurtins S, Liu SX, Sadeghi H, Calame M. Robust graphene-based molecular devices. Nat Nanotechnol 2019; 14:957-961.

[16] Thomas JO, Limburg B, Sowa JK, Willick K, Baugh J, Briggs GAD, Gauger EM, Anderson HL, Mol JA. Understanding resonant charge transport through weakly coupled single-molecule junctions. Nat Commun 2019; 10:4628.

[17] S. Zhao QW, J. Pi, J. Liu, J. Zheng, S. Hou, J. Wei, R. Li, H. Sadeghi, Y. Yang, J. Shi, Z. Chen, Z. Xiao, C. Lambert, W. Hong,. Cross-plane transport in a single-molecule two-dimensional van der Waals heterojunction. SCIENCE ADVANCES 2020.

[18] Limburg B, Thomas JO, Holloway G, Sadeghi H, Sangtarash S, Hou IC-Y, Cremers J, Narita A, Müllen K, Lambert CJ, Briggs GAD, Mol JA, Anderson HL. Anchor Groups for Graphene-Porphyrin Single-Molecule Transistors. Advanced Functional Materials 2018; 28.

[19] Prins F, Barreiro A, Ruitenberg JW, Seldenthuis JS, Aliaga-Alcalde N, Vandersypen LM, van der Zant HS. Room-temperature gating of molecular junctions using few-layer graphene nanogap electrodes. Nano Lett 2011; 11:4607-4611.

[20] Ullmann K, Coto PB, Leitherer S, Molina-Ontoria A, Martin N, Thoss M, Weber HB. Single-molecule junctions with epitaxial graphene nanoelectrodes. Nano Lett 2015; 15:3512-3518.

[21] Cao Y, Dong S, Liu S, He L, Gan L, Yu X, Steigerwald ML, Wu X, Liu Z, Guo X. Building high-throughput molecular junctions using indented graphene point contacts. Angew Chem Int Ed Engl 2012; 51:12228-12232.

[22] Jia C, Wang J, Yao C, Cao Y, Zhong Y, Liu Z, Liu Z, Guo X. Conductance switching and mechanisms in single-molecule junctions. Angew Chem Int Ed Engl 2013; 52:8666-8670.

[23] Jose´ M Soler EA, Julian D Gale, Alberto Garc´ıa, Javier Junquera, Pablo Ordejo´n and Daniel Sa´nchez-Portal. The SIESTA method for ab initio order-N materials simulation. JOURNAL OF PHYSICS: CONDENSED MATTER 2002.

[24] Dion M, Rydberg H, Schroder E, Langreth DC, Lundqvist BI. van der Waals density functional for general geometries. Phys Rev Lett 2004; 92:246401.

[25] J Ferrer CJL, V M García-Suárez, D Zs Manrique, D Visontai, L Oroszlany, R Rodríguez-Ferradás, I Grace,, S W D Bailey KG, Hatef Sadeghi and L A Algharagholy. GOLLUM: a next-generation simulation tool for electron, thermal and spin transport. New Journal of Physics 2014.

[26] Latha Venkataraman YSP, Adam C. Whalley, Colin Nuckolls, Mark S. Hybertsen, and Michael L. Steigerwald. Electronics and Chemistry: Varying Single-Molecule Junction Conductance Using Chemical Substituents. American Chemical Society 2007.

[27] Tan Z, Zhang D, Tian HR, Wu Q, Hou S, Pi J, Sadeghi H, Tang Z, Yang Y, Liu J, Tan YZ, Chen ZB, Shi J, Xiao Z, Lambert C, Xie SY, Hong W. Atomically defined angstrom-scale all-carbon junctions. Nat Commun 2019; 10:1748.

Chapter 6.

6 Conclusions and future work

6.1 Conclusion

In this thesis, density functional theory DFT was utilized to explore charge transport in graphene-single molecule-graphene junctions. DFT results confirm that charge transport in graphene junctions is in a cross-plane direction and significantly different from that of conventional in-plane transport. There are six chapters in this thesis, and the following is a summary of each chapter.

Chapter 1. provides an overview of molecular electronics and how it has developed over the past several decades. The advantages and examples of single-molecule junctions with graphene electrodes are also discussed.

Chapter 2. discusses density functional theory (DFT) which is employed to study electronic structure and properties of molecules in this thesis. The key principles and components of density functional theory are discussed.

Chapter 3. describes the theory of charge transport through molecules. Several concepts were discussed, including the Landauer formula, scattering matrix, bond currents and Green's function. Several important formulas were also derived, including the transmission coefficient and the Berit-Wigner equation.

Chapter 4. examines the electrical properties of three molecular bilayer graphene molecules (MBLG-C114, MBLG-C108 and MBLG-C96) and molecular single-layer (MSLG-C96), sandwiched between two graphene sheets. This study studies the

influence of the size and layer number of molecular graphene on charge transport in cross-plane graphene molecular junctions. DFT results indicate that the electrical conductance of the molecular junction based on the largest molecular area, MBLG-C114, is higher than that of the smallest molecular area, MBLG-C108 and MBLG-C96. Additionally, single-layer molecular graphene MSLG-C96 has a greater electrical conductivity than molecular bilayer graphene MBLG-C96. According to these results, charge transport in molecular graphene junctions is affected by the size and number of layers present in the junction.

This chapter also examines the angle between the graphene flake and peripheral mesityl groups. In molecular bilayer graphene, charge transport is studied at an angle close to 90° between the graphene flake and peripheral mesityl groups (crystal configuration), and then the mesityl groups are rotated manually to 30° and 10°. For molecular single-layer graphene, I have also investigated the angle between the graphene flake and the peripheral mesityl groups by rotating them manually at 40°, 35°, 30°, and 20°. According to DFT results, charge transport through molecular graphene in these molecular junctions is influenced by the angle between the graphene flake and peripheral mesityl groups, and these rotated groups can be utilized to tune electrical conductance.

Chapter 5. examines how substituents and conjugation affect charge transport in cross-plane molecular junctions based on two groups of molecules. First, to study the effect of substituent groups on electron transport in cross-plane molecular junctions, the two hydrogen atoms in Pyrene are replaced by electron-withdrawn (-Br) and electron-donating ($-NH_2$) substituents to form DBPyr and DAPyr, respectively. The results indicate that DBPyr and DAPyr exhibit greater transmission functions at Fermi energy

E_F than Pyrene, which can be due to a decrease in the HOMO-LUMO gap for the corresponding molecules. In contrast, in metal electrode junctions where electron transport is in-plane mode, electron-donating substituents lead to an increase in molecular junction conductance, while electron-withdrawing substituents lead to a decrease [1].

Second, to study the impact of conjugation on electron transport in cross-plane molecular junctions, three molecules were selected with different degrees of conjugation and, as a result, planarity 6HPyr, 4HPyr, and 16HPyr. These molecules are conjugated in the following order: 6HPyr, 4HPyr, and 16HPyr. It is evident from the DFT results that the transmission functions of molecular junctions based on 6HPyr are higher than those of molecular junctions based on 4HPyr and 16HPyr. Therefore, it can be concluded that as the degree of conjugation of the three molecules gradually decreases, the conductance of their constructed molecular junctions decreases correspondingly. This is consistent with the previous study's conclusion that disruption of the conjugated structure affects the electrical transport of graphene/fullerene single molecule/graphene junctions [2].

6.2 Future work

For the immediate future, I shall undertake a collaborative project aimed at investigating charge transport through non-planar organic molecules that were successfully sandwiched between two graphene electrodes using a cross-plane break junction technique (XPBJ). Figure 6.1 (a, b and c) shows the molecular structures of Oligophenylene ethynylenes (OPEs), with different anchoring group positions. Moreover, Figure 6.2 shows the molecular structures of benzodifurans (BDFs) with different anchoring groups. The OPEs and BDFs can be coupled to graphene electrodes

via van der Waals interactions. In this study, I aim to examine the influence of molecular anchoring group position, molecular backbone, and anchoring groups on cross-plane graphene-based junctions and compare the results to conventional Au-molecule-Au junctions.

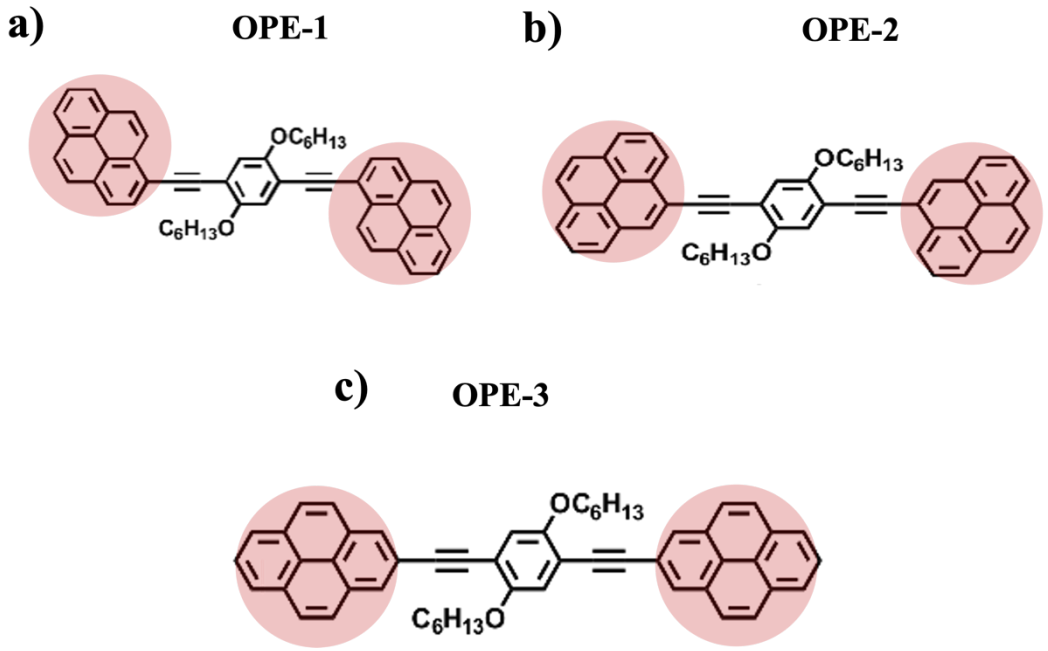

Figure 6.1. The molecular structures of Oligophenylene ethynylenes (OPEs). (a) OPE-1, (b) OPE-2, and (c) OPE-3.

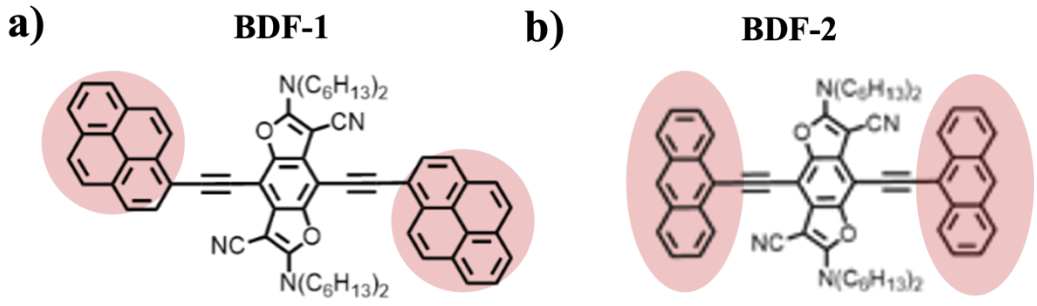

Figure 6.2. The molecular structures of benzodifurans (BDFs), (a) BDF-1 and (2) BDF-2.

In the future, I would also like to explore and design molecular switches, rectifiers or memristors based on cross-plane junctions which have been demonstrated in the in-plane junctions. There are, of course, many avenues of research which could be fruitfully explored. For example, it would be interesting to study phonon transport through molecular junctions by generalising early theories of phonon transport in molecular-scale wires [3]. It would also be of interest to examine the effect of using different metallic electrodes or substrates, such as platinum, palladium [4, 5] and graphene [8], which would allow the role of the electrode work function to be explored. Most recently [9], molecular junctions using superconducting electrodes have been reported experimentally, which means that theories of nanoscale superconducting proximity effects [10,11] can now be utilised to explore the interplay between superconductivity and molecular-scale quantum interference.

6.3 Bibliography

[1] Latha Venkataraman YSP, Adam C. Whalley, Colin Nuckolls, Mark S. Hybertsen, and Michael L. Steigerwald. Electronics and Chemistry: Varying Single-Molecule Junction Conductance Using Chemical Substituents. American Chemical Society 2007.

[2] Tan Z, Zhang D, Tian HR, Wu Q, Hou S, Pi J, Sadeghi H, Tang Z, Yang Y, Liu J, Tan YZ, Chen ZB, Shi J, Xiao Z, Lambert C, Xie SY, Hong W. Atomically defined angstrom-scale all-carbon junctions. Nat Commun 2019; 10:1748.

[3] A. Kambili GF, Vladimir I. Fal'ko, and C. J. Lambert. Phonon-mediated thermal conductance of mesoscopic wires with rough edges. The American Physical Society 1999.

[4] García-Suárez VM, Rocha AR, Bailey SW, Lambert CJ, Sanvito S, Ferrer J. Single-channel conductance ofH2molecules attached to platinum or palladium electrodes. Physical Review B 2005; 72.

[5] Garcia-Suarez VM, Rocha AR, Bailey SW, Lambert CJ, Sanvito S, Ferrer J. Conductance oscillations in zigzag platinum chains. Phys Rev Lett 2005; 95:256804.